2016-06-16

Development of an Imaging/Therapy Integrated System by Using Radionuclide 192Ir for Breast Cancer

Jian Fang
University of Miami, jfangf@gmail.com

UNIVERSITY OF MIAMI

DEVELOPMENT OF AN IMAGING/THERAPY INTEGRATED SYSTEM BY USING RADIONUCLIDE ^{192}IR FOR BREAST CANCER

By

Jian Fang

A DISSERTATION

Submitted to the Faculty
of the University of Miami
in partial fulfillment of the requirements for
the degree of Doctor of Philosophy

Coral Gables, Florida

August 2016

UNIVERSITY OF MIAMI

A dissertation submitted in partial fulfillment of
the requirements for the degree of
Doctor of Philosophy

DEVELOPMENT OF AN IMAGING/THERAPY INTEGRATED SYSTEM BY USING RADIONUCLIDE ^{192}IR FOR BREAST CANCER

Jian Fang

Approved:

_____
Weizhao Zhao, Ph.D.
Professor of
Biomedical Engineering

_____
Fabrice Manns, Ph.D.
Professor of
Biomedical Engineering and
Ophthalmology

_____
Jorge Bohorquez, Ph.D.
Associate Professor of
Professional Practice of
Biomedical Engineering

_____
Edward A. Dauer, M.D.
Research Associate Professor of
Biomedical Engineering

_____
Yidong Yang, Ph.D.
Assistant Professor of
Radiation Oncology

_____
Guillermo Prado, Ph.D.
Dean of the Graduate School

_____
Xiaodong Wu, Ph.D.
CEO and President of
Biophysics Research Institute
of America

FANG, JIAN (Ph.D., Biomedical Engineering)
Development of an Imaging/Therapy Integrated System by Using Radionuclide ^{192}Ir for Breast Cancer. (August 2016)

Abstract of a dissertation at the University of Miami.

Dissertation supervised by Professor Weizhao Zhao.
No. of pages in text. (130)

Breast cancer is the second most common cancer diagnosed among women in the United States following skin cancer. About one−third of women cancer patients have breast cancer. Following lung cancer, breast cancer has the second highest death rate compared to other types of cancer. Radiation therapy is a common way to treat breast cancer after surgery; it can significantly decrease the breast cancer recurrent rate. For early breast cancer treatment, breast-conserving surgery followed by radiation therapy is highly recommended compared to mastectomy. Since most of the local recurrences occur near the tumor bed, additional boost radiation to the tumor bed benefits patients of all age groups.

In this dissertation, we developed an innovative imaging/therapy integrated system by using radionuclide Ir-192 for breast cancer. Three major studies have been completed. First of all, we proofed the possibility of using Ir-192 as an external source for breast imaging by Monte Carlo simulation. Secondly, we built an imaging assembly in a physical laboratory setting to further validate the imaging ability of Ir-192 source. Thirdly, a preliminary 3-D conformal treatment plan was created by using a commercially available treatment planning system to evaluate the treatment capability of using Ir-192 source in the future.

Based on our studies, a new platform which combines imaging and treatment via a single radiation source (Ir-192) can potentially be implemented in the future for image-guided radiation therapy. In this context, patients are not required to undergo an external imaging modality to guide the brachytherapy treatment, so the dual-function radiation source can simplify the procedure and increase the efficiency. In addition, it will streamline the device and cut down the cost significantly.

ACKNOWLEDGMENTS

I would like to express my deepest gratitude to my advisor, Dr. Weizhao Zhao. Through his support, guidance and friendship, he has introduced me to the world of Medical Physics. His generosity with his time, care and concern, goes over and beyond that of a great mentor.

I am also highly indebted to Dr. Xiaodong Wu, for his tremendous help in this work, as well as for tapping on his wealth of knowledge, resources, and expertise.

I am grateful to my committee members, Drs. Jorge Bohorquez, Fabrice Manns, Edward Dauer and Yidong Yang for taking time out of their busy schedules to proofread and attend my proposal and defense, and for fielding thought-provoking questions.

I would like to thank my wife for her continuous support and belief in me, and for giving me such a beautiful and lovable baby girl whose delightful smiles and coos energizes me every day when I return home.

Finally, I would like to thank my family for their endless support all the time.

Jian Fang

August 2016, Coral Gables

TABLE OF CONTENTS

LIST OF FIGURES

LIST OF TABLES

LIST OF ABBREVIATIONS

3-D: Three Dimension
BCS: Breast-Conserving Surgery
CBCT: Cone Beam Computed Tomography
CCS: Collapsed Cone Superposition
CNB: Core Needle Biopsy
CRT: Conformal Radiotherapy
DAQ: Data Acquisition Device
DCIS: Ductal Carcinoma in situ
DNA: Deoxyribonucleic Acid
DICOM: Digital Imaging and Communications in Medicine
DVH: Dose-Volume Histogram
EGS: Electron Gamma Shower
EGSnrc: EGS National Research Council Canada
EIT: Efficiency Improving Technique
EPID: Electronic Portal-Imaging Device
FBCT: Fan Beam Computed Tomography
FDA: Food and Drug Administration
FDK: Feldkamp-Davis-Kress
FNAB: Fine Needle Aspiration Biopsy
GBBS: grid-based Boltzmann solvers
GEANT4: Geometry and Tracking 4
GTV: Gross Tumor Volume
GUI: Graphic User Interface
HDR: High-dose Rate
HU: Hounsfield Unit
IDC: Invasive Ductal Carcinoma
IGRT: Image-Guided Radiation Therapy
ILC: Invasive Lobular Carcinoma
IMAT: Intensity Modulated Arc Therapy
IMRT: Intensity Modulated Radiation Therapy
IORT: Intraoperative Radiotherapy

KV: Kilovoltage

LCIS: Lobular Carcinoma in situ

LDR: Low-dose Rate

LINAC: Linear Accelerator

MC: Monte Carlo

MCNP: Monte Carlo N-Particle Transport Code

MDR: Medium-dose Rate

MLC: Multileaf Collimator

MRI: Magnetic Resonance Imaging

MV: Megavoltage

OAR: Organs at Risk

OBI: On-Board Imager®

OID: Object to Imager Distance

OS: Operation System

PDR: Pulse Dose Rate

PET: Positron Emission Tomography

PENELOPE: Penetration and Energy Loss of Positrons and Electrons

PTV: Planning Target Volume

QA: Quality Assurance

RBE: Biological Effectiveness

SAVI: Strut Adjusted Volume Implant

SOD: Source To Object Distance

SPECT: Single Photon Emission Computed Tomography

TPS: Treatment Planning System

US: Ultrasound

VMAT: Volumetric Modulated Arc Therapy

VOI: Volume of Interest

VRT: Variance Reduction Technique

CHAPTER 1

INTRODUCTION

1.1 Breast Cancer Overview

Tumor is a swelling part of the body and is caused by abnormal growth of tissue. It can be separated into two categories: benign tumor and malignant tumor. Breast cancer is a malignant tumor that starts from the breast. It can grow uncontrollably and spread to the surrounding tissues and organs, even to the whole body (American Cancer Society [ACS], 2015). Most of the breast cancer cases are found in women, but men could develop this disease too. In the United States, breast cancer is the second most common cancer in women after skin cancer (National Cancer Institute [NCS], 2014), and it also has the second highest death rate among women following lung cancer (DeSantis, Ma, Bryan, & Jemal, 2014).

1.1.1 Types of Breast Cancer

Breasts are composed mainly of connective and fatty tissues. Breast milk is produced in small lobules, and the lobules forms lobes. The milk is transported to the nipple through small thin tubes, which are called ducts. The breasts do not contain muscles, but they have blood vessels and lymph vessels (Dahnert, 2011). There are many types of breast cancers and each type is based on how the cancer cells appear under the microscope. The most common breast cancers are carcinomas. It starts from epithelial cells which forms the

lining of breast. Sarcoma is another type of cancer that can occur in the fat and connective tissue of breast, but it is not as common (ACS, 2015).

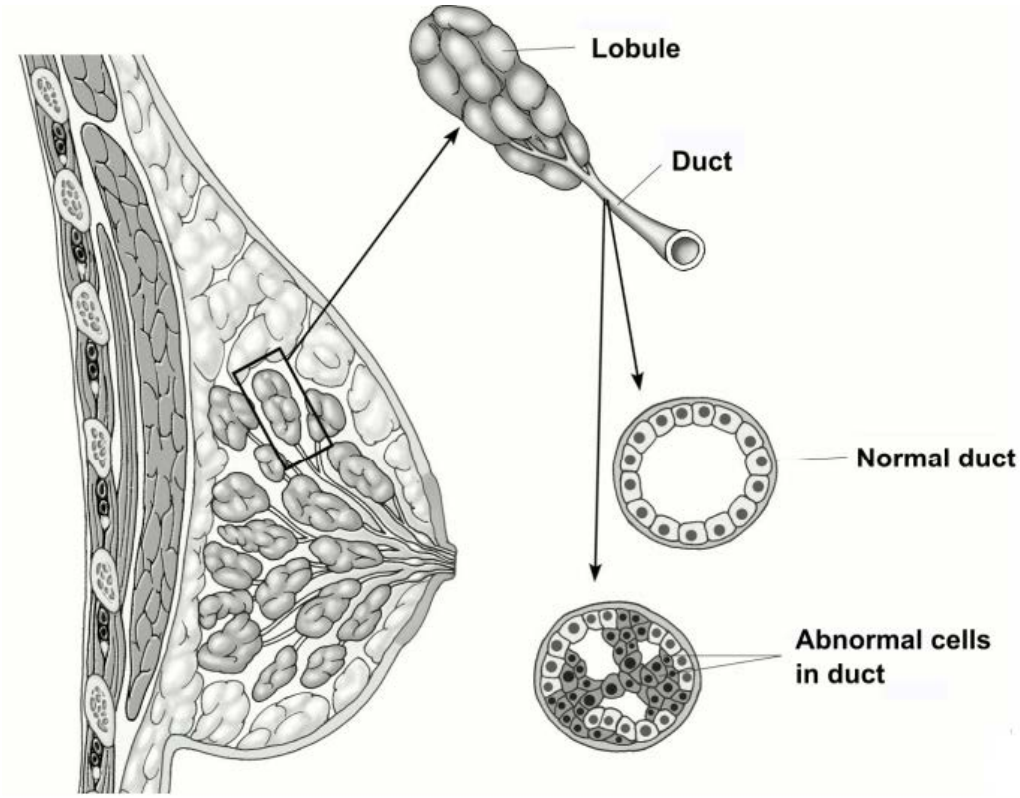

Figure 1.1 Ductal carcinoma in situ (ACS, 2015).

Breast cancer types can be further categorized based on where the cancerous cells are, and whether the cells have the ability to metastasize. Majority of the cancerous cells start from ducts and lobules. If those cells stay in their original locations and do not invade the surrounding tissues, the cancer is called noninvasive, or in situ. However, if those cells

spread into fat or connective tissues, it is invasive, or infiltrating (Hartmann & Loprinzi, 2012). In some rare cases, breast cancer can be a combination of different types of tumors or even a mixture of invasive and noninvasive cancer. Ductal carcinoma in situ (DCIS) (Figure 1.1) is the most common noninvasive breast cancer (ACS, 2015). Though it is a noninvasive cancer, there is a high risk that the cancer will develop into an invasive cancer in the future if the cancerous cells are not removed. Lobular carcinoma in situ (LCIS) (Figure 1.2) is another type of noninvasive breast cancer. The cancerous cells stay in the region of lobules and they do not spread outside of the lobules wall. Invasive ductal carcinoma (IDC) begins in a breast duct, breaks through the duct wall, and then invades the connective and fatty tissue around. It can also move to other locations in the human body through the cardiovascular and lymphatic circulation system. About 75 percent of invasive breast cancer belongs to IDC. Invasive lobular carcinoma (ILC), a very similar type of breast cancer to IDC except for the location where the cancer starts, represents another 15 percent of invasive breast cancer (Hartmann & Loprinzi, 2012). Other atypical breast cancer types include Paget disease, inflammatory breast cancer, phyllodes tumor, angiosarcoma, etc.

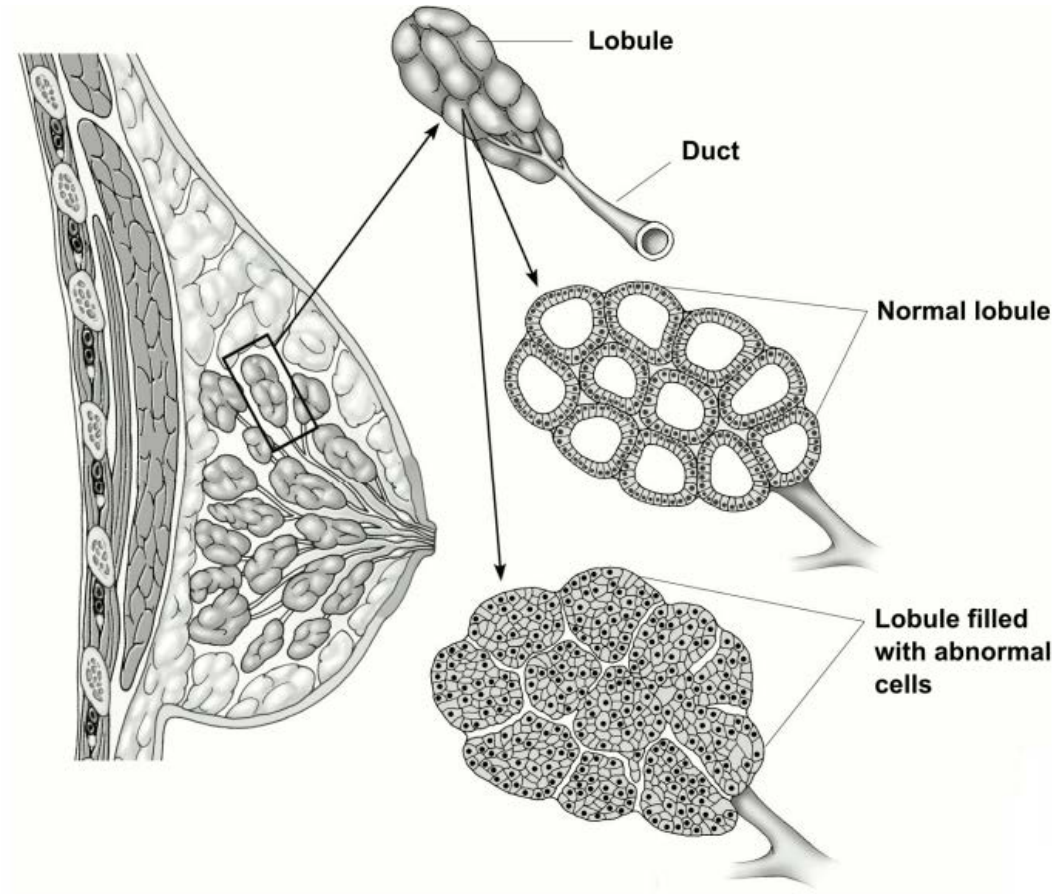

Figure 1.2 Lobular Carcinoma in situ (ACS, 2015).

1.1.2 Risk Factors

It is very difficult to determine the possibility that an individual will develop cancer. However, certain risk factors can affect the likelihood of getting cancer. Different cancers have different risk factors. For example, smoking is a significant factor for lung, mouth, and larynx cancer, while long exposure to strong sunlight is a factor for skin cancer. However, that does not imply that people with one or more risk factors will definitely get cancer. Most women, who have several risk factors for breast cancer, never develop breast cancer during their lives. On the other hand, some women with breast cancer may not have

any apparent risk factors or may carry only a limited number of risk factors. It is not so easy to determine if those factors contribute to the disease.

Risk factors can be broadly classified to three groups: not related to personal choice, lifestyle related factors and unclear factors (ACS, 2015). Gender, age and race are the strongest risk factors that are predetermined (Hulka & Moorman, 2001). The risk of breast cancer in women is a few hundred times higher than in man, because certain female hormones such as estrogen and progesterone can stimulate the growth of cancer cells. Older females usually have a higher risk of breast cancer. The incident rate almost doubles every ten years until menopause (McPherson, Steel, & Dixon, 2000). Overall, white women are a little more likely to develop breast cancer than black women, but black women are more likely to die of this cancer. Other races including Asian, Hispanic and Native-American woman have a lower risk to develop breast cancer.

Genetic defects are hereditary, thus family history play an important role in breast cancer risk too. BRCA1, the first breast cancer susceptibility gene, was identified in 1990 and cloned in 1994 (Miki et al., 1994). It not only affects breast cancer, but also ovarian cancer. Researches show that people who carry BRCA1 mutation genes have as high as an 80% chance of developing breast cancer during their lifetime (Hulka & Moorman, 2001). BRCA2 is another breast cancer susceptibility gene. The mutation of BRCA2 gene has a high risk of developing into breast cancer, but unlike BRCA1, BRCA2 does not confer a substantially elevated risk of ovarian cancer (Wooster et al., 1994). Additionally, BRCA2 mutations for breast cancer risk are lower, around 45% (ACS, 2015). In healthy cells, both BRCA1 and BRCA2 help prevent cancer by making proteins that keep the cells from growing abnormally. Other gene mutations also increase the risk of breast cancer, although

not as significant as BRCA1 and BRCA2. These genes include ATM, TP53, CHEK2, PTEN, CDH1, STK11 and PALB2 (ACS, 2015). We also need to consider family history of breast cancer. Women, whose mother, sister or daughter (first-degree relatives) are diagnosed with breast cancer, have doubled risk of breast cancer. If they have two first-degree relatives with breast cancer, the risk triples (McPherson et al., 2000). BRCA1 and BRCA2 mutations can be inherited not only from mothers, but also fathers. Furthermore, a woman who was treated with cancer in one breast has an increased risk of developing a new cancer in the other breast or in another part of the same breast. This risk is even higher if breast cancer was diagnosed at a younger age. Women who start menstruating early in life or who have a late menopause have an increased risk of developing breast cancer, because of longer lifetime exposure to estrogen and progesterone. Ionizing radiations to the chest wall, especially for young women, increases the risk of breast cancer.

Some lifestyles have proved to affect the risk of developing breast cancer. Having children is one of the considerations. Women who have never given birth at all or who first gave birth after the age of 30 have a slightly higher breast cancer risk. More pregnancies or becoming pregnant at a young age can reduce breast cancer risk, due to the reduction of menstruation times during lifetime (Hulka & Moorman, 2001). Breastfeeding over a long term can also help to decrease the risk of breast cancer. Researches show that there is a clear relationship between drinking alcohol and breast cancer. Alcohol abuse and excessive drinking (more than 3 drinks per day) will significantly increase the risk of breast cancer, about 1.5 times more than women who do not drink alcohol (Singletary & Gapstur, 2001). An alcoholic drink per day slightly increases the risk.

Diet is an arguable factor. Many studies have attempted to find out the link between diet and breast cancer risk, but there is no conclusion yet. Some studies found no evidence that diet affects breast cancer risk (Pierce et al., 2007), while some other studies claim that diet plays a role. For example, the research by Cho et al. (2006) indicated that greater red meat intake was strongly related to elevated risk of breast cancers (Cho et al., 2006). Bingham et al. (2003) found that the risk of breast cancer rises with increasing fat intake, particularly saturated fat (Bingham et al., 2003). Research by Shin et al. (2002) indicated no correlation between intake of dairy products and breast cancer in postmenopausal women. However, for premenopausal women, high intake of low-fat dairy foods was associated with a reduced risk of breast cancer (Shin et al., 2002). Another ambiguous risk factor of breast cancer is smoking. The 2014 US Surgeon General's report concluded that there is "suggestive but not sufficient" evidence that smoking increases the risk of breast cancer (ACS, 2015).

1.1.3 Diagnosis

Breast cancer can be found when symptoms appear. The most common symptoms are breast lump and mass. The lump is usually soft, tender and can be either painless or painful. It is imperative that women check with their breast health professionals as soon as possible upon the discovery of a new breast lump or mass. Other symptoms include swelling of all or part of a breast, skin irritation or dimpling, breast or nipple pain, nipple retraction, redness, scaliness, or thickening of the nipple or breast skin, and nipple discharge other than breast milk. Women in the early stages of breast cancer generally have no symptoms, so it is crucial to get screening tests.

The most popular and recommended test for early screening is mammogram (Figure 1.3). A mammogram is an X-ray of the breast. The X-ray beams pass through the tissues and strike the film. The film will then display the density difference of the tissues, due to the attenuation of X-rays. Screening mammograms are used to look for breast disease in women who have no breast cancer symptoms. The ACS recommendations for early breast cancer detection in women with an average risk of breast cancer are as follows: For ages 40 to 44 years old, women are encouraged to begin annual screenings. Women between the ages of 45 to 54 should get annual mammogram screenings. Women aged 55 years and older should transition to biennial screenings. The ACS does not recommend physical breast examinations for breast cancer screening among average-risk women at any age (Oeffinger et al., 2015). During a mammogram, the breast is pressed between two plates in order to spread and flatten the tissue for a readable film. If the screening mammogram shows a lump or any abnormal results, the physician will usually prescribe a diagnostic mammogram. Unlike the screening mammogram, which only takes two projections, the diagnostic mammogram will include more images of the area of concern. A biopsy is needed if the diagnostic mammogram shows that the abnormal area is suspected of cancer.

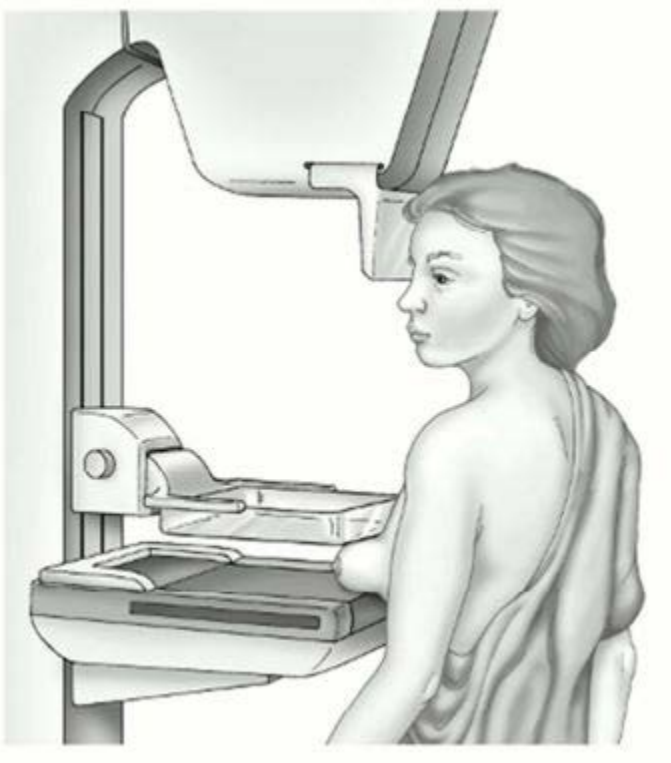

Figure 1.3 Mammogram (ACS, 2015).

Not all lumps are cancerous. Some of them are cysts. They can be distinguished by a breast ultrasound. Ultrasound, also known as sonogram, uses soundwave to detect objects in the body. A transducer is placed on the skin of the patient's breast and it generates high frequency (over 1 MHz) sound waves. The waves will penetrate the tissues and feedback an echo signal, which is in turn processed by a computer to form a black and white image. Ultrasound, when coupled with mammogram, becomes a valuable tool for diagnosing breast cancer. Not only is it able to differentiate between cyst and tumor, it is also painless and safe. Patients are not exposed to radiation during the entire diagnostic process. It is an ideal imaging modality for pregnant women and also for those who are not able to receive a mammogram or Magnetic resonance imaging (MRI).

MRI scan uses radio waves and strong magnetic fields to generate images of the body. During a breast MRI scan, the patient is placed on a couch within an MRI scanner in the prone position. There are openings on the couch for each breast that allow them to be imaged without compression. The machine forms a strong magnetic field around the breast to be imaged. Hydrogen atoms in tissues containing water molecules are used to create a signal that is processed to form an image of the body. The strong magnetic field will excite these hydrogen atoms, which then emit a radio frequency signal. This signal is measured by a receiving coil. Furthermore, by using a gradient coil, a different coil that varies the main magnetic field, the position information of radio signals can be read. The contrast between different tissues is determined by the rate at which excited atoms return to the equilibrium state (McRobbie, Moore, Graves, & Prince, 2007). Compared to both the mammogram and the ultrasound, the MRI scan provides more detailed information and usually takes a longer time. In order to receive a clear and useful image, it is very important to stay still during the whole scanning process. If a screening mammogram is not enough to determine the suspicious area, the MRI may be used as a backup. Some studies showed that MRI for breast cancer screening has a higher sensitivity compared to mammogram and breast ultrasound (Kuhl et al., 2005; Lee et al., 2010). MRI is sometimes used for diagnosis purposes, such as to determine the actual size of the cancer and to look for any other cancers in the breast.

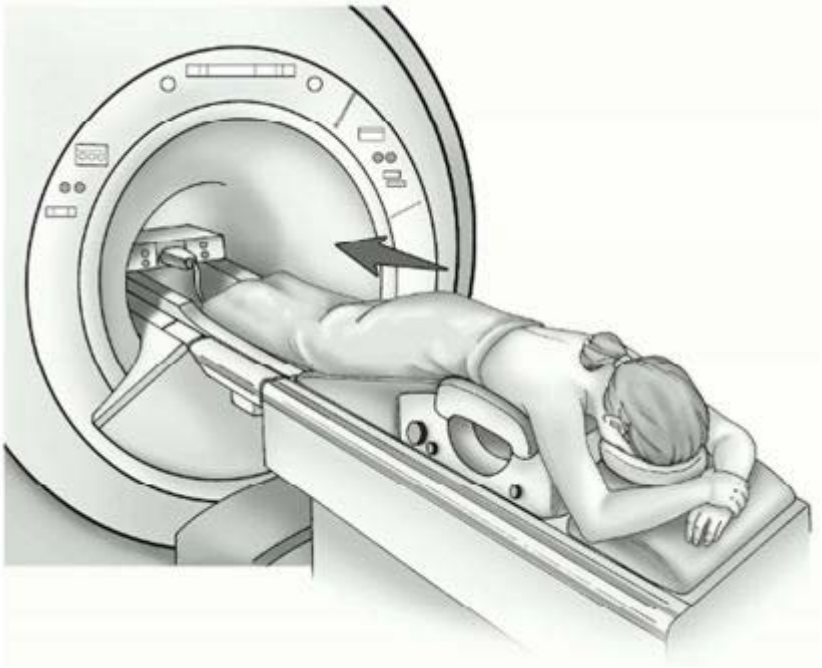

Figure 1.4 Breast MRI (ACS, 2015).

Biopsy is a further diagnostic procedure for the abnormal areas that are found by a mammogram, breast ultrasound or breast MRI (Figure 1.4). It is the only way to confirm if cancer is really present. In the United States, among the women screened annually for 10 years, approximately 50 percent will need additional imaging, and 5 to 7 percent will have biopsies (Hubbard et al., 2011), which indicates over a million women receive breast biopsies each year. Pathologist will examine the tissue sample from biopsy under a microscope, and send a report containing the diagnosis results to the physician. There are three major types of biopsies: fine needle aspiration biopsy (FNAB), core needle biopsy (CNB) and open surgical biopsy. Depending on each patient's specific situation, a different technology will be applied. Some factors to be concerned include the appearance, size, location and quantity of the suspicious lesion, or the patients' personal preferences.

FNAB is the least invasive diagnostic method among the three biopsies. During the procedure, the physician extracts a small portion of tissue from the suspicious area by using a very thin, hollow needle that is attached to a syringe. The needle size can be as small as 23 gauge (23 gauge = 0.5733mm diameter = 0.2582 mm^2 cross sectional area), which is smaller than the commonly used blood test needle (Daltrey & Kissin, 2000). The sample tissue will be examined under a microscope. If the physicians can feel the lesion with their hands, the needle will be guided into the area just by feeling it. This is called palpation guide. Otherwise, the physicians will need to use an ultrasound to guide the needle to the suspicious area. The cost of FNAB is low and the result can be made available within a shorter time frame. Since it uses a tiny needle, it has a lower probability of causing hematoma and other rare complications, such as pneumothorax. However, the accuracy of the diagnosis is poor, compared to CNB. Many studies (Willems, Van Deurzen, & Van Diest, 2012) have shown that for large lesion area or metastasis cancer, the positive prediction rate for FNAB decreases to 78%. This is because sometimes the needle is not guided accurately to the area and so will miss collecting suspicious tissues at the cancer cells location. Moreover, even if cancer cells are found, it is usually not possible to determine if the cancer is invasive. The low prediction rate greatly affects its popularity. Nowadays, FNAB is not widely used or even abandoned in many institutions in United States and United Kingdoms, but it is still commonly used in many developing countries (Yu, Wei, & Liu, 2012). If a final diagnosis cannot be provided by FNAB, the physicians will prescribe a second or a different type of biopsy.

A CNB uses a larger needle to sample suspicious tissue. The needle size range from 18 gauge (18 gauge = 1.0237mm diameter = 0.8230 mm^2 cross sectional area) to 7 gauge

(7 gauge = 3.6649mm diameter = 10.5488 mm^2 cross sectional area) (Preibsch et al., 2015; Nath, Robinson, Tobon, Chough, & Sumkin, 1995). The procedure is similar to FNAB, but because the needle is larger than the one used in FNAB, much more abnormal tissue samples can be extracted at once. CNB also requires several cores for one sampling. Also, some imaging guided methods are usually used in tandem, such as stereotactic mammogram, ultrasound or MRI, to locate the lesion.

In some cases, a vacuum device is used to assist in removing the tissue sample from the needle, which is called vacuum-assisted core biopsies (Dahabreh et al., 2014). During this process, a small incision is made on skin and a hollow probe is inserted through this incision. The probe is guided by imaging methods and arrives at the lesion area. There is a hole at the side of the probe, so the tissue can be suctioned into the probe. A rotating knife equipped within the probe will then cut the tissue off. This method usually removes more tissue than a regular CNB (ACS, 2015).

CNB is an outpatient setting. Thus, it requires local anesthesia to reduce pain, because it removes larger pieces of tissue. A CNB is more likely to provide a clear diagnosis than an FNAB, although it might still miss some cancers. Overall, FNAB has average success rates of 75% to 90% for palpable lesions, and 34% to 58% for non-palpable lesions, while the success rates of CNB are 97% and 94%, respectively (Willems et al., 2012).

FNAB and CNB are usually accurate enough to make a diagnosis. However, a more aggressive method called surgical biopsy needs to be applied sometimes, for example, when the results of the CNB are inconclusive. The whole lump area will be removed during surgical biopsy and sent to a pathologist. Since the surgery removes a great mass of breast,

there is a high possibility of a breast shape change after this biopsy and a scar is usually left behind. Surgical biopsy is considered to be the most accurate, but it also carries a higher risk of complications, such as bleeding or infection. Compared to all three major biopsies, CNB has a highly accurate diagnosis, and is certainly more reliable than FNAB and less invasive than surgical biopsy (Pagni, Spunticchia, Barberi, Caprio, & Paglicci, 2014). The patients and physicians may prefer CNB to other biopsies.

A whole diagnosis procedure usually includes the three parts mentioned above and involves three medical personnel. Firstly, self-examination or a physical examination is done by a clinician. Secondly, a mammogram, ultrasound or MRI is handled by a radiologist. Thirdly, a biopsy completed by a pathologist. These three diagnostic steps can narrow down the missed diagnosis of breast cancer to less than 1% (Yu et al., 2012).

1.1.4 Treatment Methods

The treatments of breast cancer can be broadly grouped based on how the treatments are performed and at which tumor stage they are used. Systemic therapy includes chemotherapy, hormone therapy and targeted therapy, while local therapy includes surgery and radiation therapy (ACS, 2015).

Systemic therapy is a treatment method where prescribed drugs administered orally or directly into the bloodstream can reach cancer cells anywhere in the body. Depending on when the therapy is given, systemic therapy can be separated to two categories: adjuvant therapy and neoadjuvant therapy. Adjuvant therapy is usually applied after surgery. Surgery is used to remove all of the cancer cells that are visible, but there are possibilities

that some cancer cells may have been left behind or may have spread to other parts of the human body, which cannot be seen. Adjuvant therapy is then used to kill those cancer cells, which reduces the risk of breast cancer recurring. Unlike adjuvant therapy, neoadjuvant therapy needs to be applied before surgery. It can help to shrink the tumor so that the tumor can be removed with less extensive surgery. That is the reason that neoadjuvant therapy is usually used to treat cancers that are too big to be surgically removed at the time of diagnosis (Mauri, Pavlidis, & Ioannidis, 2005). It is also able to provide more information on how the cancer cells respond to the treatment. Should neoadjuvant therapy fail to shrink the tumor, other methods will be needed.

Chemotherapy treatment usually lasts for several months. It is given in cycles, with each period of treatment followed by a recovery period. Each cycle will vary according to the chemo drugs used. These drugs will target cells that are dividing quickly, since it is characteristic of cancer cells. However, some other cells, such as cells in the bone marrow, in the lining of the mouth and intestines, and in the hair follicles, also divide quickly. These cells can be affected by chemo drugs, which can lead to side effects. Some of the most common possible side effects include hair loss and nail changes, mouth sores, loss of appetite or increased appetite and low blood cell counts, etc. Different types of drugs will result in different side effects. It also depends on the amount of drugs taken and the length of treatment. Some women may have many side effects; others may only have few. These side effects usually last a short period of time and subside after treatment is completed.

Gene alteration is one of the important risk factors of breast cancer. Three broad categories of gene changes that appear to contribute to tumor progression include tumor suppressor genes, repair-mutator genes, and oncogenes (Pegram, Pietras, Bajamonde,

Klein, & Fyfe, 2005). Targeted therapy uses drugs that specifically target these gene mutations. Most commonly used drugs include tamoxifen for estrogen receptor, and trastuzumab for HER-2 (Sledge, 2005). The side effects of these drugs are often mild, compared to chemo drugs. Hormone therapy is another form of systemic therapy. It is often used as an adjuvant therapy to help reduce the risk of cancer recurrence after surgery. Estrogen is one of the hormones that promote the growth of cancer cells and it is hormone receptor-positive. About 33% of breast cancer patients are hormone receptor-positive, including estrogen receptor-positive cancers and progesterone receptor-positive cancers (ACS, 2015). Most types of hormone therapy for breast cancer either lower estrogen levels or stop estrogen from acting on breast cancer cells. However, this kind of treatment is beneficial only for hormone receptor-positive breast cancers. It does not help patients whose tumors are hormone receptor-negative.

Local therapy is intended to treat a tumor at the site without affecting the rest of the body. Surgery and radiation therapy are examples of local therapies. Most women with breast cancer have some type of surgery requirement. During the procedure, a breast tumor can be removed.

Breast-conserving surgery (BCS) (Figure 1.5) only removes the part of the breast containing the cancer cells. Some surrounding normal tissue will also be removed in order to clear the connective area between cancer and normal cells, as well as to reduce the risk of cancer recurrence. How much of the breast is removed depends on the size and location of the tumor and other factors. Sometimes, if cancer cells are found at the edges of the surgical site, the surgeon may need to go back and remove more tissue. This operation is called a re-excision. In some cases, when the surgeon is not able to remove enough breast

tissue to get clear surgical margins, a mastectomy may be needed. Side effects of BCS include pain, temporary swelling, tenderness, and hard scar tissue that will form at the surgical site.

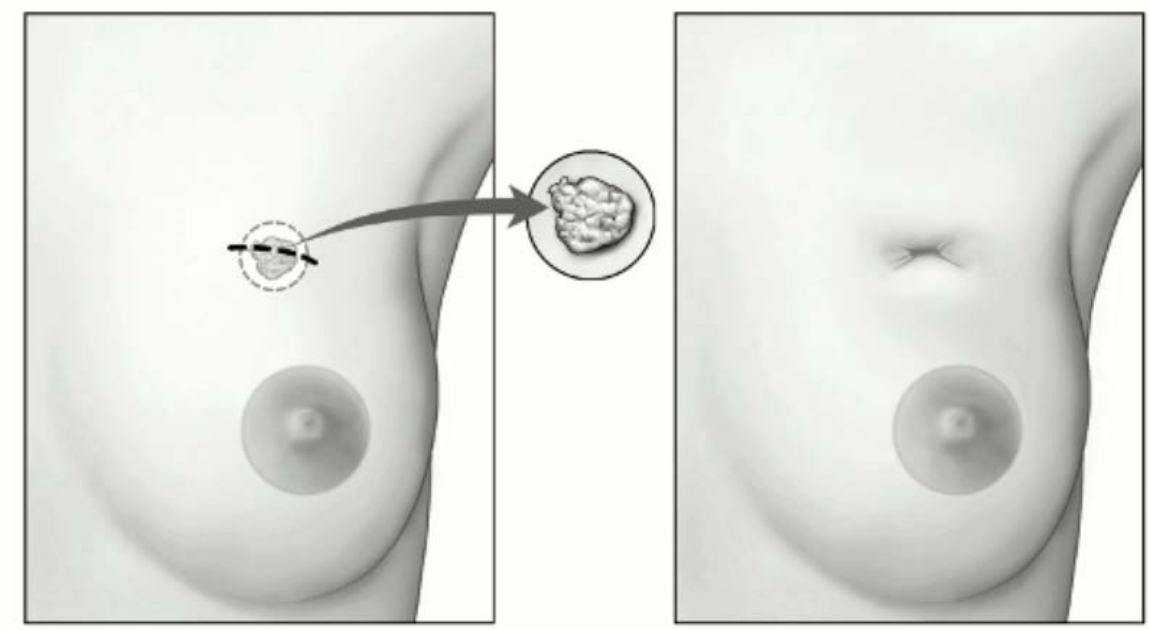

Figure 1.5 Breast-conserving surgery (ACS, 2015).

Mastectomy (Figure 1.6) is the surgery which removes the whole breast. Occasionally, the nearby tissues such as axillary lymph nodes and the pectoral muscles under the breast, or even the other breast are removed within this procedure for those high risk patients who are diagnosed with invasive breast cancer. Side effects of mastectomy include wound infection, hematoma and seroma.

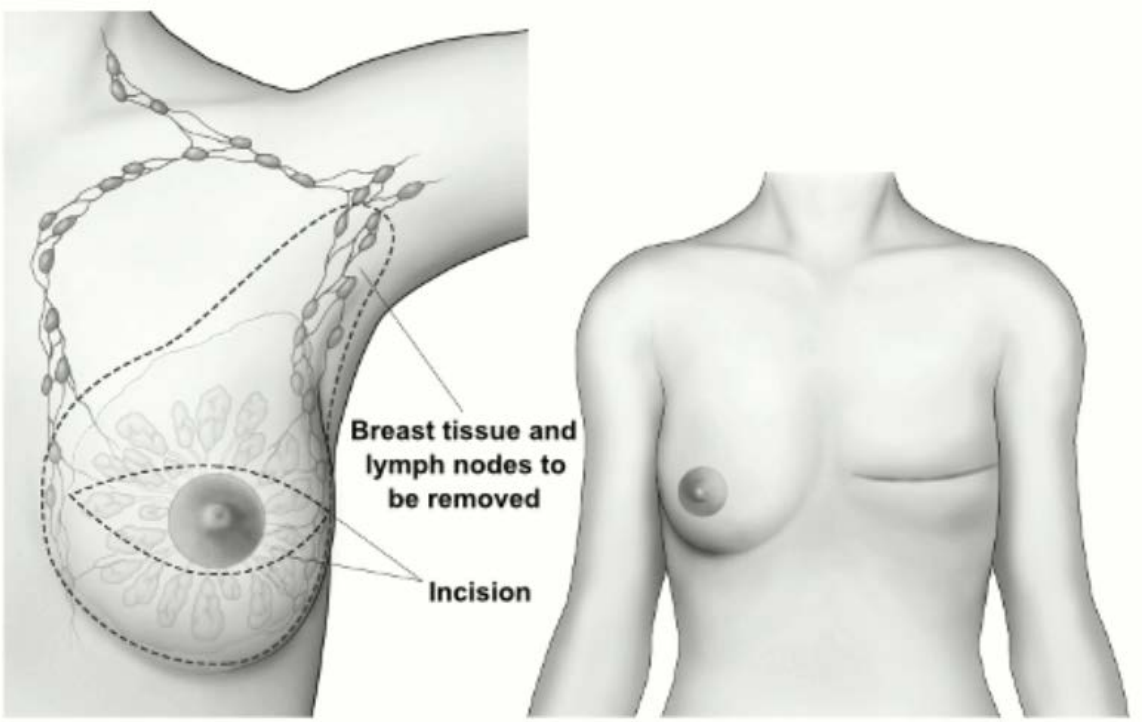

Figure 1.6 Mastectomy (ACS, 2015).

Early-stage breast cancer patients can choose between BCS and mastectomy. Though the main advantage of BCS is that a woman keeps most of her breast, she will also need radiation therapy in most cases. On the other hand, only a small percentage of women who have mastectomy for early stage cancers require additional radiation. Researches show that women who are treated by BCS with radiation have a slightly higher local recurrence rate than those who are treated by mastectomy, but they have similar overall survival rate and disease-free survival rate (McGuire et al., 2009). For some women who have invasive breast cancer, have a large-sized tumor, or have previous treatment history, mastectomy might be a better option. After having a mastectomy or some BCS, patients can choose breast reconstruction to restore the breast appearance.

1.2 Radiotherapy Treatment

Radiation therapy is usually applied to a specific area or the whole breast after surgery or chemotherapy. It is also used to treat cancer that has spread to other areas. The high-energy radiation can either directly damage the cells' Deoxyribonucleic acid (DNA) or generate charged particles, which interact with the DNA and damage it consequently. Cancer cells with damaged DNA will lose the ability to divide and die (Lawrence, Ten Haken, & Giaccia, 2008). Radiation therapy can significantly lower the likelihood of the recurrence of breast cancer. It can be further classified into two different types of treatment, external beam radiation and brachytherapy. Figure 1.7 shows a bar chart of breast cancer treatment pattern in 2012 (ACS, 2015). Base on this chart, we can see almost 46% of breast cancer treatments involve radiation therapy.

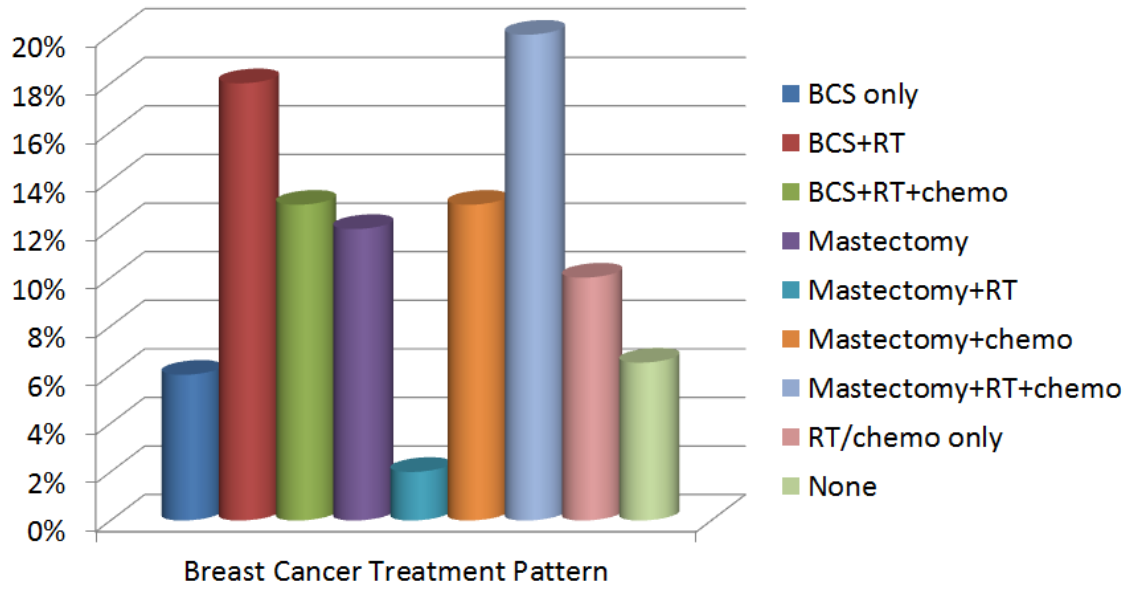

Figure 1.7 Breast cancer treatment pattern in 2012. Surgery, radiation therapy and chemotherapy are three major treatment methods for breast cancer. In 2012, about 46% of breast cancer patients were treated by radiation therapy.

1.2.1 External Beam Radiation

External beam radiation is the most common type of radiation therapy for breast cancer. The radiation is generated from a machine called linear accelerator (LINAC). LINAC uses microwave technology to accelerate electrons in a waveguide. Those electrons will collide with a heavy metal target and generate high-energy X-rays. The high-energy X-rays are delivered from outside of the body to the region of the patient's tumor. It can be used to treat all parts of the body.

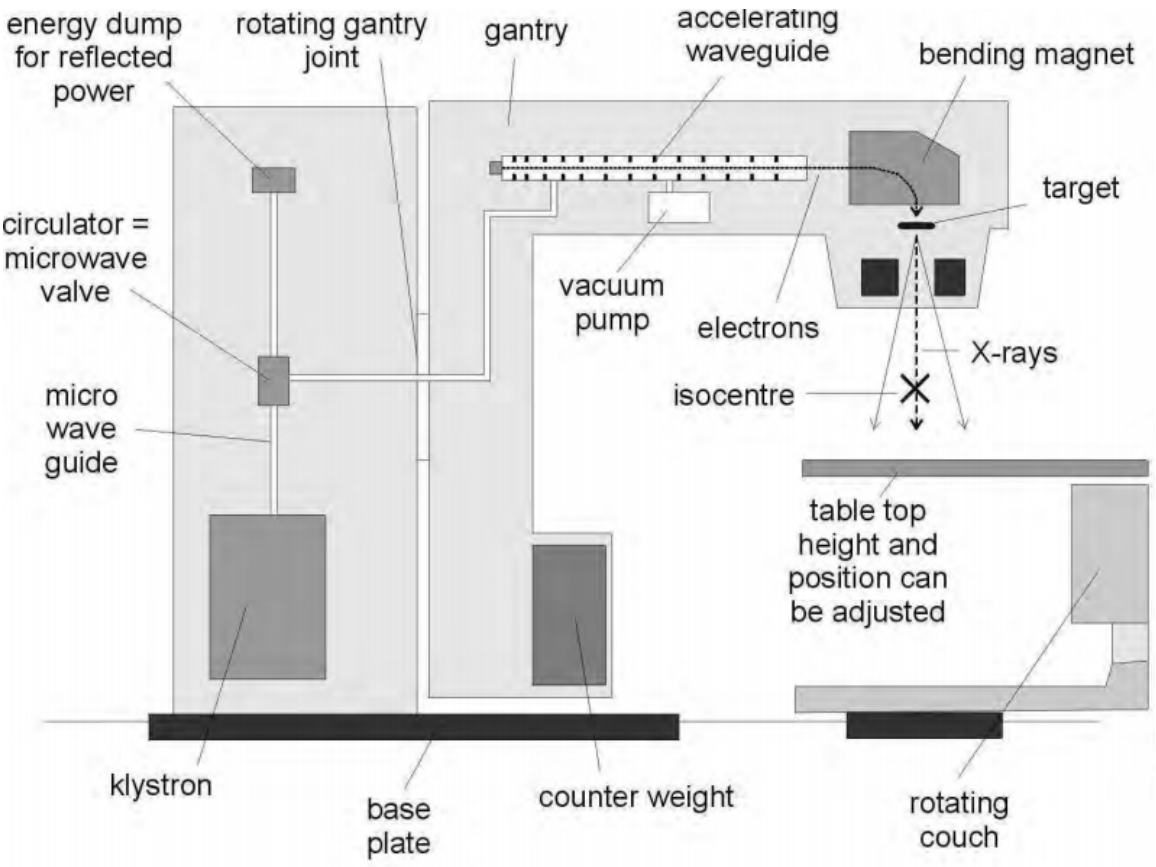

Figure 1.8 A schematic of LINAC (Tello, 2015).

Figure 1.8 shows a schematic of LINAC with inside components drew. The klystron in the drive stand plays an important role in LINAC. It amplifies the introduced

radio frequency electromagnetic waves, which travel through the micro waveguide and reach the accelerating waveguide. In some LINACs, magnetron carries the same function as klystron. The electron gun generates electrons by thermionic emission, and the amplified radio frequency is used to accelerate those electrons in the horizontal waveguide at the top of the gantry. The bending magnet changes the direction of the electron beam, from horizontal to vertical, which travels downward to the patient. There is a high density target located at the exit of the bending magnet. The collision between the electron and the target will generate X-rays. Since 94% of the collision energy converts to heat, thermal stability in the LINAC is achieved through a water cooling system in the drive stand and gantry. The X-ray beam from the target is not uniformly distributed. The photons are usually found more at the center than at the side. Beam flattening filter is designed to absorb those forward peaking photons. The filter is conical shaped and usually made of tungsten, steel, lead or uranium. The flatten beam will pass through an ion chamber, which monitors integrated dose, dose rate and filed symmetry. At the end, the radiation beams are collimated by collimators to match the shape of the treatment target. The upper and lower collimator jaws can define a rectangular filed size up to 40cm by 40cm. The multileaf collimator (MLC) was first implemented by Takahashi in 1965 (Huq, Das, Steinberg, & Galvin, 2002). It is a key part of LINAC, especially for intensity modulated radiation therapy (IMRT). Though all MLCs from different LINAC manufacturers (Figure 1.9) have different types of design, such as number of leaves and leaf thickness, they all serve the same purpose – to create a custom-specified block to spare normal tissue and direct the radiation dose to the tumor. Other compensators include trays, wedges and blocks are also available to modify the beam.

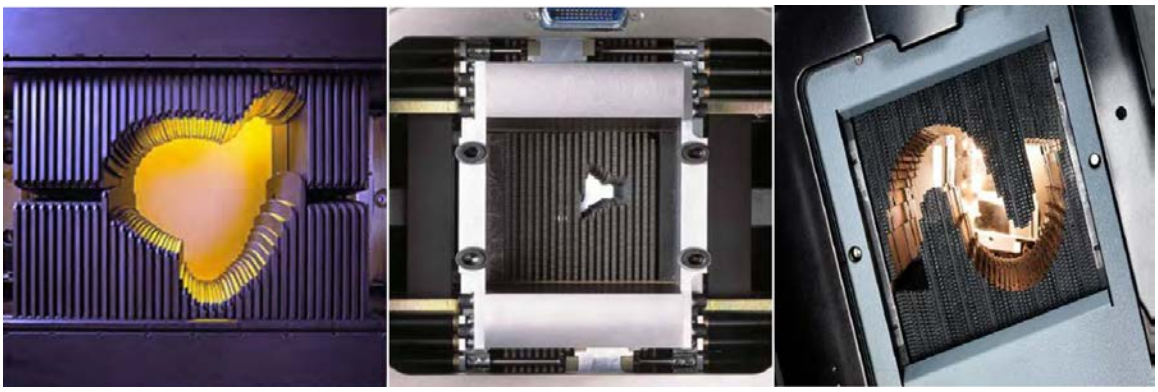

Figure 1.9 MLCs from different manufactures. Left: Varian. Middle: Elekta. Right: Siemens (Tello, 2015).

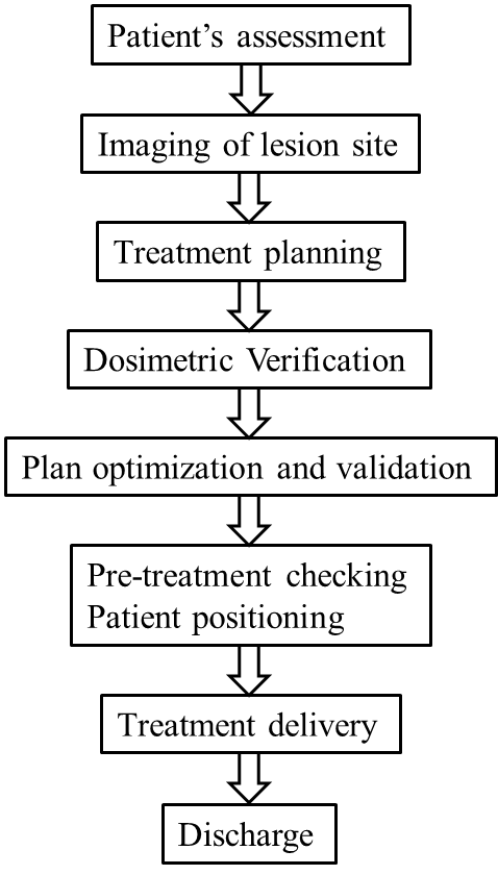

Figure 1.10 A flowchart of a typical external beam radiation therapy treatment procedure.

The main procedures of external beam radiation therapy include simulation, treatment planning and radiation delivery (Figure 1.10). Simulation is usually referred to CT simulation. In this procedure, conventional CT images are acquired and the isocenter is placed within the tumor volume (Woody & Videtic, 2014). Depending on which part of the body needs to be treated, different techniques will be applied. For breast cancer, two positioning methods are used based on facility limitation and physicians' preference. The traditional method is the supine position. The patient is required to lie down on the treatment couch with holder attached. Her arms need to be lifted up in order to expose the breast without any blockage. The other method is prone position by using a specially-designed table with a breast board. The patient's breasts naturally hang away by gravity through the hole of the board. Compared to the supine position, prone position can reduce the dosage on the surrounding organs and tissues like the heart and lungs. This lowers the risk of future complications such as heart disease, lung damage and poor cosmesis (Huppert, Jozsef, DeWyngaert, & Formenti, 2011). During the simulation, the patient needs to keep stable to acquire good quality images. The simulation results will be sent to physicians for review and prescription information will be provided. The prescription contains the total dose needed, the number of fractions, constraints, and any notes that should be delivered to dosimetrists.

Varies techniques are used for external radiation beam treatment. Three-dimensional conformal radiotherapy (3D-CRT) was developed from conventional radiotherapy, which irradiates the target area with a fixed filed size. 3D-CRT limits target area by using MLC. In the planning system, dosimetrists will arrange the MLC to form a hollow shape which matches the target's beam-view shape. One treatment often requires

several fields from different angles. Compared to conventional radiotherapy, 3D-CRT involves a reduction in the volume of healthy tissues receiving a high dose, with an increase in dose to the target volume that includes the tumor and a limited amount of normal tissue (Hall & Wuu, 2003). Along with the development of MLC, another treatment technique called IMRT appeared. It is a further development of 3D-CRT. IMRT usually requires more fields than 3D-CRT, and the MLC leaves move constantly at each field. Unlike 3D-CRT, a larger volume of normal tissue is exposed to lower radiation doses during IMRT treatment. Also, leakage radiation from increasing total monitor units rises the total body dose in IMRT. Those factors increase the risk of developing secondary cancers in the future (Hall & Wuu, 2003; Abo-Madyan et al., 2014). In 1995, Yu proposed a new method (Yu, 1995), intensity modulated arc therapy (IMAT), which is the early version of volumetric modulated arc therapy (VMAT). The greatest difference between IMAT and IMRT is the filed shape during treatment. In IMAT, the filed shape changes during continuous gantry rotation by using conventional MLC. More recently, the fast development of LINAC delivery control systems makes the feasibility of VMAT possible. These systems are able to vary the MLC leaf positions, dose rate, and gantry rotation speed during the delivery of IMAT (Rao et al., 2010). According to many researches, VMAT has the advantage of efficiency, accuracy, high dose conformality and homogeneity, and low monitor units (Otto, 2008; Rao et al., 2010; Popescu et al., 2010; Pasler, Georg, Bartelt, & Lutterbach, 2013).

Table 1.1 Comparison of different external beam radiation therapy techniques.

	Conventional	3D-CRT	IMRT	VMAT
Treatment Time	Long	Long	Middle	Short
Monitor Units	Middle	Middle	High	Middle
Target Conformality	Low	Low	High	High
Normal Tissue Dose	High	Middle	Low but widely	Low
Cost	Low	Low	Middle	High

After the treatment plan is verified and approved by physicians and physicists, patients are ready to undergo treatment. Before radiation delivery, technicians need to acquire new images and compare them with previous planning images to ensure the patient position is the same as the simulation position. This is to ensure a precise delivery of the radiation beam. This step is completed by an on-board imaging system. The imaging system, typically combined with the treatment machine, includes a kilovoltage (kV) tube and a flat panel detector. The tube and the detector are folded and hidden beside the gantry when treatment machine is on standby or during the treatment. At the time of imaging, the imaging system turns on and rotates around the same axis as the treatment head. The represented on-board imaging systems include the Synergy® Platform from Elekta Oncology and the On-Board Imager® (OBI) from Varian Medical Systems (Dawson & Jaffray, 2007) (Figure 1.11).

Figure. 1.11 A photo of Varian Edge® LINAC with OBI marked at Innovative Cancer Institute (South Miami, FL). The kV X-ray tube and imager are marked in red. They are folding back to standby position.

Both systems run cone beam computed tomography (CBCT) for this procedure. The image reconstruction calculation process starts immediately after some projections are collected. If the reconstructed results do not match to the initial simulation CT images, therapists must use a remote control to move the treatment couch. In some cases, they need to walk into the room and reset the patient if huge difference occurs between the CTs of simulation and treatment. After everything is set up correctly, the treatment can begin.

External beam treatment is the oldest method of radiation therapy for breast cancer, but it is still widely used, especially for those patients who need total breast irradiation. The whole treatment usually involves a 3- to 7-week course of daily fractions case by case

(Olivotto et al., 2013), and this relatively long period causes a great inconvenient for patients with their normal life. In addition, external beam radiation therapy may induce some side effects, owing to the extra dose to normal tissue, such as heart disease (Darby et al., 2013). However, the great advantage is patient feels no pain during the entire procedure.

1.2.2 Brachytherapy

Brachytherapy (from the Greek word brachy, meaning short distance), also called internal radiation therapy, is another form of radiation therapy where a sealed radiation source is placed inside or next to the area requiring treatment. Brachytherapy is commonly used for cervical, prostate, breast and skin cancer as primary treatment tool. It can also be used to treat tumors in other parts of the body and combined with external beam radiation treatment.

Radioactive sources for brachytherapy are now available with many radionuclides and in various shapes and sizes. The characteristics of different sources depend on their emission type, energy level and how they are constructed. An appropriate radiation source for treatment needs to meet the following requirements (Lee & Lowe, 2011):

1. A suitable half-life. For permanent implants, the half-life of radionuclide should be at least a few days long. For temporary implants, the requirement is at least a few weeks and large corrections for radioactive decay should be minimized. In addition, in order to have a useful working life, stock sources should have a long half-life.

2. A suitable energy level. The energy level of radionuclides should be high enough to deliver sufficient dose to the treatment site, but should also be suitable for radiation protection.
3. A suitable physical form. The physical form of radionuclides should be insoluble, non-dispersible and can be easily encapsulated into a structure to prevent from dispersion.
4. Suitable decay products. No gaseous or liquid decay products during radioactive decay process.
5. A suitable activity. The radionuclides should have a high specific activity.
6. A suitable cost. The cost of radionuclides should be reasonable so that the treatments are affordable to patients.

Common radionuclides for brachytherapy include Radium-226 (Ra-226), Cesium-137 (Cs-137), Cobalt-60 (Co-60), Iridium-192 (Ir-192), Iodine-125 (I-125), etc. The physical characteristics of those radionuclides can be referred to Table 1.2.

The placement of radiation sources in the target area can be temporary or permanent. Depending on the patient cases, temporary brachytherapy can be done in a single visit or multiple visits. For a single visit treatment, the low-dose seeds, which emit radiation at a rate between 0.4 to 2 Gy/hr (Miller & Thomadsen, 2009), are implanted and the patient must stay in the hospital for a few days until the target area receive enough dose. The radioactive seed will be removed on the last day. This method is potentially hazardous to the medical staffs.

Table 1.2 Physical characteristics of some common radionuclides used in brachytherapy (Lee & Lowe, 2011).

Source	Usual form	Production	Half-life	Emissions
Radium-226	Tubes, Needles	Naturally occurring	1620 years	2.45 MeV gamma ray
Cesium-137	Tubes, Needles, Afterloading	Fission Product	30.17 years	0.662 MeV gamma ray
Cobalt-60	Tubes, Afterloading	Neutron activation	5.26 years	1.17 and 1.33 MeV gamma ray
Iridium-192	Wires, Afterloading	Neutron activation	74 days	0.38 MeV gamma ray
Iodine-125	Seeds	Daughter of Xenon-125	59.6 days	27.4, 31.4 and 35.5 keV X-rays
Palladium-103	Seeds	Neutron activation	17 days	21 keV X-ray
Gold-198	Grains	Neutron activation	2.7 days	0.412 MeV gamma ray
Strontium-90	Plaques	Fission Product	28.7 years	2.27 MeV beta particles
Ruthenuim-106	Plaques	Fission Product	1.02 years	3.54 MeV beta particles

For multiple visits treatment, high-dose seeds, which emit radiation at a rate of more than 12 Gy/hr (Miller & Thomadsen, 2009), are implanted and removed in the same surgical sitting. Permanent brachytherapy involves a single hospital visit with low-dose seeds. Dose is delivered over the lifetime of the sources. The dose rate of brachytherapy indicates how much radiation is delivered to the surrounding medium and is expressed in Grays per hour (Gy/h). Low-dose rate (LDR) brachytherapy involves low-dose seeds and it is commonly used for cancers of the oral cavity (Yoshimura et al., 2009), cervix (Nag et

al., 2002), soft tissue sarcomas (Nag, Shasha, Janjan, Petersen, & Zaider, 2001) and prostate cancer (Ho, Burri, Cesaretti, Stone, & Stock, 2009). On the other hand, high-dose rate (HDR) brachytherapy uses high-dose seeds. The most common treatment sites for HDR brachytherapy include cervix (Nag et al., 2000b), endometrium (Nag et al., 2000a), head and neck (Nag, Cano, Demanes, Puthawala, & Vikram, 2001), prostate (Yamada et al., 2012) and breasts (Guinot et al., 2015). Most HDR treatments are performed on an outpatient basis. Another uncommon category based on dose rate brachytherapy called medium-dose rate (MDR) brachytherapy is characterized by a medium rate of dose delivery, ranging between 2 Gy/hr to 12 Gy/hr (Miller & Thomadsen, 2009).

During the early days of brachytherapy treatment, all radionuclides and applicators were applied to or inserted into the patient manually. With the growing concerns about radiation safety, the techniques of afterloading were developed for reducing radiation exposure to medical staffs. If the operators apply the radionuclides to the applicators by using appropriate handling tools, it is called manual afterloading (Lee & Lowe, 2011). This kind of afterloading can only be used for LDR treatments since the operators and other medical staffs in the room will be irradiated. Another system called remote afterloading, which is the most popular afterloading currently. It is also called machine afterloading. The radionuclide is stored in a well-shielded device and remote controlled by a computer. A room with appropriate shielding is required. Because the operators control the source outside the treatment room, the radiation dose on the operators can be minimized. Remote afterloading technique is available for HDR, as well as LDR. The most common brachytherapy afterloaders include the microSelectron® Digital and Flexitron® platform from Nucletron® - Elekta (Stockholm, Sweden), and VariSource™ iX HDR and

GammaMedplus™ iX HDR/pulse dose rate (PDR) from Varian Medical Systems (Palo Alto, CA) (Yue, Chen, & Zou, 2014).

Figure 1.12 Afterloader systems from different manufacturers. Top left: microSelectron® Digital afterloader. Top right: Flexitron® afterloader. Bottom left: VariSource™ iX HDR afterloader. Bottom right: GammaMedplus™ iX HDR/PDR afterloader.

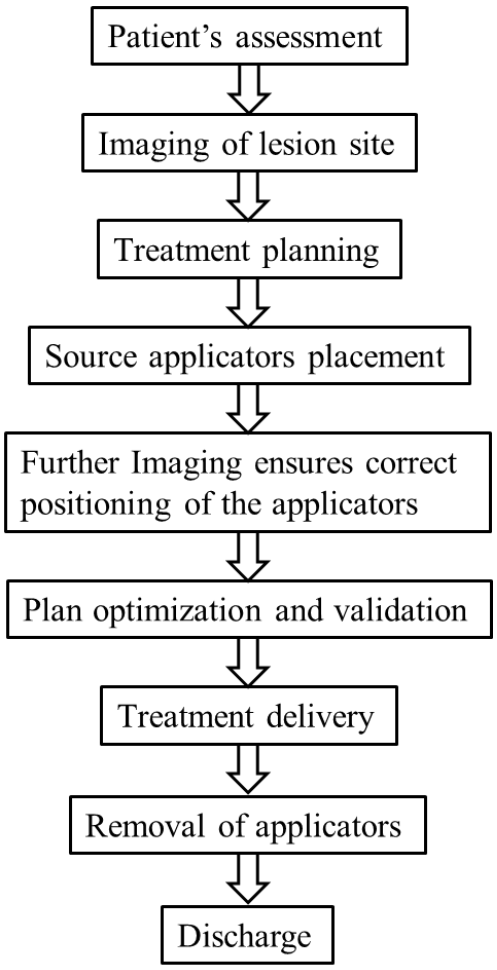

Figure 1.13 A flowchart of a typical brachytherapy treatment procedure.

The procedure of brachytherapy is relatively similar to external beam radiation therapy (Figure 1.13). Imaging simulation that includes CT, MRI, positron emission tomography (PET), etc., can provide patients' data for treatment planning. Interstitial and intracavitary brachytherapy are the two most commonly used HDR techniques for patients who had BCS (Figure 1.14). For interstitial breast brachytherapy, multiple catheters are temporary placed through the breast tissue surrounding the lumpectomy cavity, usually at 1 to 1.5 cm intervals. The number of catheters used is determined by the size and shape of the target (Vicini & Arthur, 2005). These catheters are carefully positioned to allow optimal

targeting of radiation to the treatment area while sparing the surrounding breast tissue. However, due to the complicated and challenging implantation of those catheters, interstitial brachytherapy is not offered at many radiation oncology centers (Richards et al., 2004).

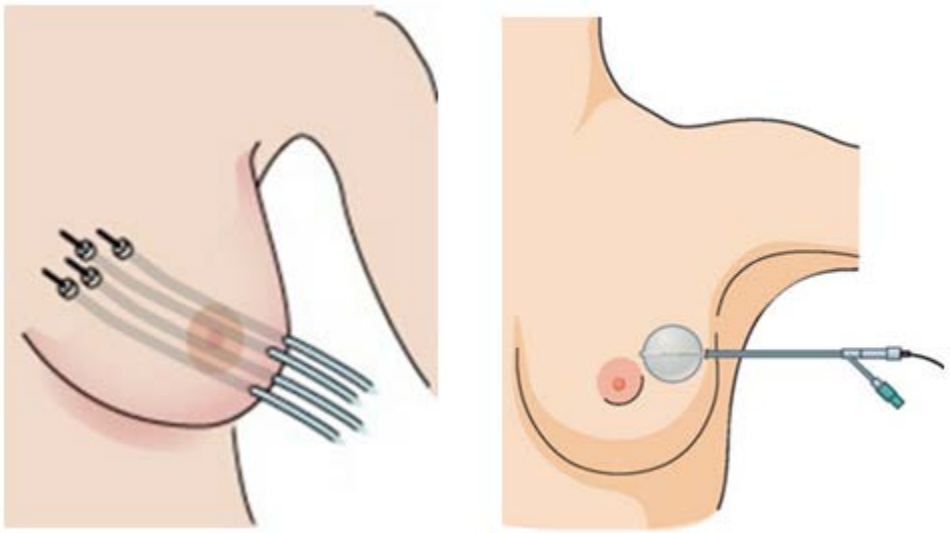

Figure 1.14 Two most common breast brachytherapy techniques. Left: Interstitial breast brachytherapy. Right: Intracavitary breast brachytherapy (Richardson, 2010).

Intracavitary breast brachytherapy involves the placement of a single catheter into the lumpectomy cavity. This technique is benefited with the fast development of catheter technologies. In May 2002, the Food and Drug Administration (FDA) approved a new treatment device (Richards et al., 2004), the MammoSite applicator (Hologic Inc., Marlborough, MA). This applicator opened a new era for intracavitary radiation. It significantly simplified the delivery of breast brachytherapy by changing the implantation process, and improved the reproducibility of dosimetry target coverage (Kelley, Cuttino, Vicini, & Arthur, 2007). The traditional MammoSite is a 15 cm long double-lumen balloon catheter specially designed for HDR afterloader (Figure 1.15). One port is for balloon

volume control, which allows the saline or other contrast fluid expanding the balloon to fit the cavity. The other port is for radiation source access, which connects to an afterloader. The afterloader delivers the radiation dose through the catheter and into the balloon. In order to fit different lumpectomy cavity sizes, varying shapes and sizes of balloon catheters have been developed (Figure 1.15).

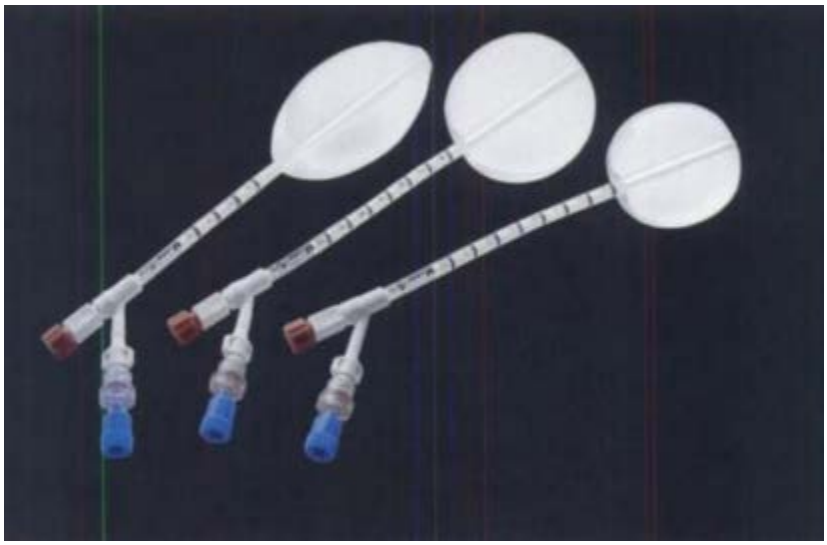

Figure 1.15 Different sizes of MammoSite applicators. Left: a 4 × 6 elliptical balloon applicator. Middle: a 5 × 6 spherical balloon applicator. Right: a 4 × 5 spherical balloon applicator (Kelley, Cuttino, Vicini, & Arthur, 2007).

The catheter can be placed at the time of the lumpectomy or postoperatively following the determination of pathologic size, margin and nodal status. Imaging methods are necessary to guide catheter insertion and verify balloon location and symmetry. The planning dose is usually delivered between 5 to 7 days with 2 treatments per day (Richards et al., 2004). After each treatment, the radiation source is removed and no radiation remains in the breast in between treatments. Some new applicators (Figure 1.16), including MammoSite multi-lumen (Hologic Inc., Marlborough, MA), Contura (Hologic Inc.,

Marlborough, MA) and Strut Adjusted Volume Implant (SAVI) (Cianna Medical Inc., Aliso Viejo, CA), combine the features of interstitial and intracavitary breast brachytherapy, which uses multiple catheters but are inserted through a single-entry point in the breast. Many studies show that these multiple catheters applicators can provide a more precise target dose (Yashar, Blair, Wallace, & Scanderbeg, 2009; Scanderbeg, Yashar, White, Rice, & Pawlicki, 2010; Kim & Trombetta, 2014).

Brachytherapy provides a localized irradiated area around the radiation source by precisely placing the source directly at the site of the tumor bed. It reduces the radiation to the healthy tissues tremendously comparing to the external beam radiation therapy. In addition, even if the patient moves or if there is any movement of the tumor within the body during treatment, the radiation sources retain their correct position in relation to the tumor. All those characteristics allow a physician to use a higher total dose of radiation to treat a smaller area in a shorter time than external beam radiation treatment.

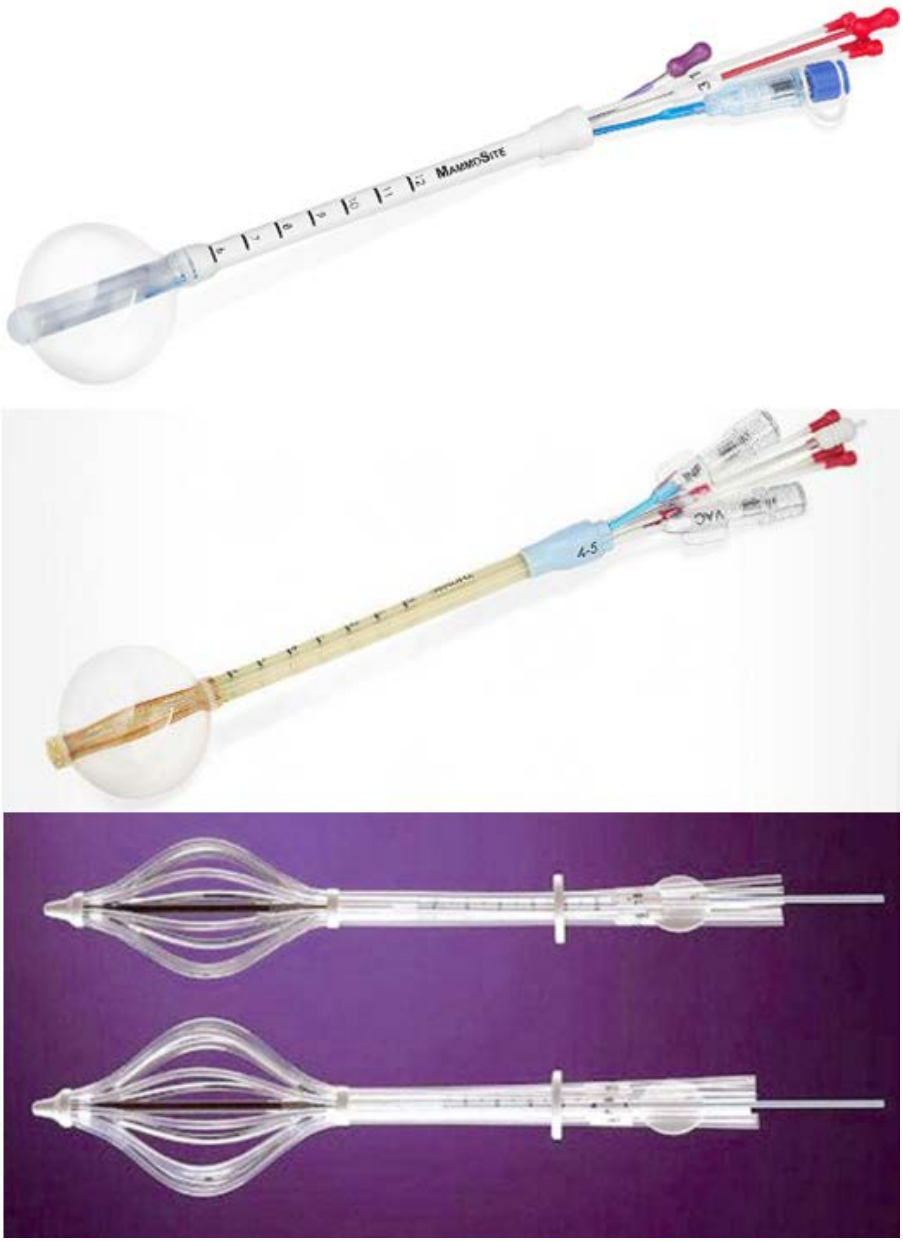

Figure 1.16 Multi-lumen applicators from different manufacturers. Top: MammoSite multi-lumen (Hologic Inc., Marlborough, MA). Middle: Contura (Hologic Inc., Marlborough, MA). Bottom: Strut Adjusted Volume Implant (SAVI) (Cianna Medical Inc., Aliso Viejo, CA), (Skowronek, Wawrzyniak-Hojczyk, & Ambrochowicz, 2012).

1.2.3 Intraoperative Radiotherapy

If the radiation is delivered to the tumor bed by a single fraction and during the lumpectomy, it is called intraoperative radiotherapy (IORT) (Kim & Trombetta, 2014). There are several methods that are used to deliver IORT. Electron IORT can provide a uniform dose distribution to the tumor bed, because of the characteristic of electron beams, where the depth of radiation penetration can be easily controlled. X-ray IORT can be separated to two categories, orthovoltage IORT and low-energy IORT. Orthovoltage X-ray IORT delivers 250-300 kV X-rays to the tumor bed, however, the poor uniformity as a result of the depth of penetration causes the healthy tissues to receive high radiation dose. It also requires additional shielding for the operating room. Compared to orthovoltage X-ray IORT, low-energy X-ray IORT uses a maximum of 50 kV X-rays, and its relative biological effectiveness (RBE) on tumor cells is higher due to the higher ionization density. Furthermore, low-energy X-rays usually has a limited range, so the conventional walls of the operating room is sufficient to stop the radiation. HDR IORT was developed in the late 1980s to lower the cost of IORT, since many cancer centers already had HDR devices. However, due to the limited radiation penetration of the HDR source, the treatment time is longer than other IORT techniques. That means the patient needs to stay in the operating room longer, and more anesthesia and greater blood loss are expected. It also requires extra measures for radiation protection.

The development of new small and mobile IORT devices (Figure 1.17) makes IORT accessible for more hospitals. IORT provides the maximum effect to the tumor bed. It delivers a concentrated dose of radiation to a tumor site immediately after a tumor is removed, helping to destroy the microscopic tumor cells that may be left behind. IORT is

precise. It spares and protects healthy tissues and organs very well. The most advantage of IORT is shortening the treatment times (Reitsamer et al., 2008). The integration of the complete radiation treatment into the surgical procedure helps most patients finish treatment and get back to their normal lives quicker, compared to traditional radiation therapy which is typically given over 5 to 6 weeks after surgery.

Figure 1.17 Mobile IORT devices. Left: Novac 7 (New Radiant Technology – NRT, Rome, Italy), a Electron IORT device, can generate 4, 6, 8 and 10 MeV electron beams. Right: INTRABEAM (ZEISS, Oberkochen, Germany), a low-energy X-rays device, provides 50 kV photon beams.

1.2.4 New Technologies

AccuBoost®

AccuBoost (Advanced Radiation Therapy, Tyngsboro, MA) (Figure 1.18) is a breast brachytherapy system that delivers radiation to the lumpectomy cavity either as a boost after external beam treatment or as a monotherapy of partial breast irradiation (Iftimia, Talmadge, Ladd, & Halvorsen, 2015). This system combines a mammography unit with a

HDR Ir-192 remote afterloader. Specially-designed tungsten alloy surface applicators are used to collimate the radiation beam.

Figure 1.18 A photo of AccuBoost® system at Lynn Cancer Institute (Boca Raton, FL).

The treatment procedure of AccuBoost starts with imaging. The patient's breast is immobilized within the mammography system just like a normal mammography setup. Mammogram images will be taken first and radiation oncologists will need to determine

how much dosage is required. They will also need to choose the appropriate applicator size and shape for this patient based on the shape and position of the tumor bed to be treated. Two applicator shapes are available: round and D-shaped. The round shape applicator is usually used, since majority lumpectomy cavities are spherical or slightly ovoid in shape. However, for those cavities which are close to the chest wall, the D-shaped applicators are more commonly used because the compression of breast will affect those cavities' shape (Rivard, Melhus, Wazer, & Bricault Jr, 2009).

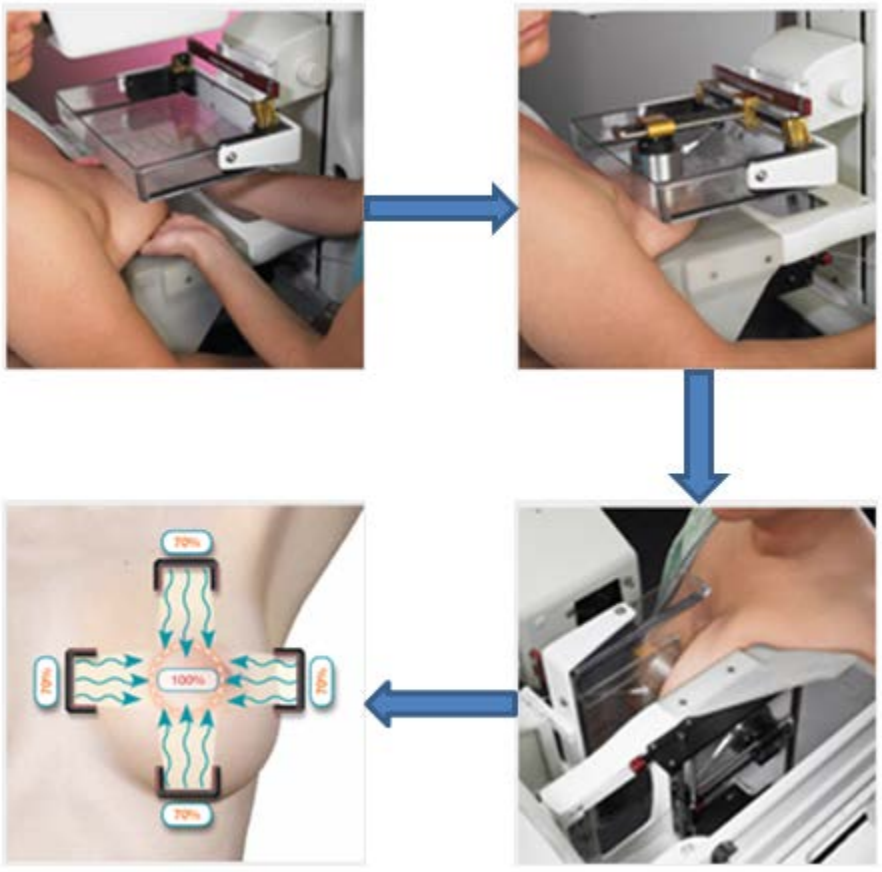

Figure 1.19 The treatment process of AccuBoost. From top left: Step 1. Target and applicator size selection. Step 2. Vertical treatment. Step 3. Horizontal treatment. Step 4. Overlapping treatment (AccuBoost, 2016).

Without decompressing the breast, the applicators will be attached to the boards on either side of the breast with their surfaces facing each other (Figure 1.19). The applicators are connected to an HDR afterloader through catheters. Brachytherapy dose is delivered from these parallel-opposed beams from a stepped HDR Ir-192 source. After the two vertical beams have delivered, this process is repeated for the two horizontal beams. A four-field delivery plan is then formed (Figure 1.19).

AccuBoost is currently equipped in some treatment centers in the United States. Rivard et al. (2009) evaluated the dosimetric characterization of round applicators by using films and Monte Carlo simulation. It showed that the dosimetric agreement within a few percent was obtained along the central axis between measurements and simulations, which is within 1% of the published results over the radial/angular region of interest. Hamid et al. (2012) evaluated the feasibility, implementation, and early results of 147 women patients who were treated with AccuBoost. The result indicated that this treatment method was associated with acceptably mild normal tissue toxicity and favorable early cosmesis. However, not all patients can be candidates for this technique. AccuBoost is suitable for most patients, especially for those who have larger breast size. It is very difficult to locate posterior cavity, but surgical clips can improve the accuracy (Hepel, Leonard, Hiatt, DiPetrillo, & Wazer, 2014).

GammaPod™

GammaPod™ (Xcision Medical Systems, Columbia, MD) is a novel stereotactic breast irradiation device (Figure 1.20). The concept and technique of GammaPod is similar to Gamma Knife (Elekta, Stockholm, Sweden), except for the treatment area. GammaPod

is for breast cancer treatment, whereas Gamms Knife is for head and neck cancer patients. It consists of a hemispherical source carrier containing 36 Cobalt-60 sources, a tungsten collimator with two built-in collimation sizes, a dynamically controlled patient support table and a breast immobilization cup which also serves as the stereotactic frame for the patient (Ödén et al., 2013).

Figure 1.20 The GammaPod radiation unit. Top: A photo of GammaPod unit. Bottom Left: A schematic of GammaPod without cover. The treatment couch stands for patient loading, and the breast immobilization cup is locked in the opening. Bottom Right: A schematic of GammaPod shielding body, source carrier and collimator (Yu et al., 2013).

The clinical procedure is similar to the external beam radiation therapy. GammaPod does not carry on-board imaging system, so CT or MRI is used for planning. During the simulation, the patient lies in prone position. The breast is immobilized in a patented breast cup (Figure 1.20) with a two-layer design. A negative air pressure between the inner and outer layers will provide a gentle suction to the breast, which helps to pull the breast away from patient's chest. The large separation between the breast and the chest lowers down the radiation dosage on those critical organs, such as heart, lungs and chest wall. A fiducial wire is contained in the outer layer of the breast cup to identify the stereotactic location. The patient starts the treatment with the exact same simulation immobilization and position to ensure accurate beam delivery. If multiple fractions are required, each fraction will require the same imaging, planning and treatment procedure (Yu et al., 2013).

The GammaPod has its own treatment planning system (TPS), running inverse planning algorithm. Mutaf et al. (2013) evaluated the dosimetric and spatial accuracy between its TPS calculations and real patients' dosimetric measurements. They found that GammaPod TPS is able to generate a plan which meets clinical radiotherapy standards, and these highly complex treatment plans have outstanding geometric and dosimetric accuracy. Ödén et al. (2013) compared GammaPod dosimetric characteristics to brachytherapy results. It showed that GammaPod provides adequate and more uniform dose coverage to centrally and peripherally located targets with an acceptable dose fall-off and lower relative skin dose than the brachytherapy techniques including single and multi-lumen devices.

GammaPod is not available in the market currently. The device is still under reviews by five medical centers for clinical trials, including University of Maryland

Medical Center, The University of Kansas Cancer Center, University of Texas Southwestern Medical Center, Allegheny General Hospital/Western Pennsylvania Hospital and Thomas Jefferson University Hospital (Bavley, 2012). They will collect evidence through the clinical trials for the approval by FDA before the GammaPod can be used clinically.

1.3 Significance and Motivation

The procedure for all types of treatment involves similar processes, i.e., from patient staging, simulation, treatment planning, and radiation delivery, to patient follow-up (Xing et al., 2006). The indispensable part of each process is imaging. CT, MRI and Ultrasound (US) are commonly used imaging modalities for breast cancer. For external beam radiation, this step is usually completed by an on-board imaging system, which simplifies the treatment procedure and increases the accuracy. However, for brachytherapy and the new techniques of breast cancer treatment, the imaging system uses a separated and independent imaging method, ranging from US (Zannis, Walker, Barclay-White, & Quiet, 2003), CT (Cuttino, Todor, & Arthur, 2005), to mammography (Sioshansi et al., 2008), etc., to confirm the irradiation position in the current treatment procedure. Although brachytherapy has the advantages of a focused, localized, and flexible irradiating capability, the lack of a coherent imaging system limits its treatment accuracy.

Low energy level and short half-life radionuclides (F-18, Tc-99m, etc.) are generally used as biosignal or biomarker sources in PET and single photon emission computed tomography (SPECT) to generate nuclear medicine images for diagnoses. In

clinical applications, these radionuclides are injected into the patient's body and distributed through the circulation system. Based on the feature of the biomarker, radionuclides are accumulated at the region of tumor cells, because those cells have higher metabolism rate than normal cells. Detectors in PET/SPECT will collect photon activities emitted by the radionuclides, which are then used for image reconstruction. In these applications, radionuclides are used as internal emission-based imaging sources. Other high-energy level radionuclides (Co-60, Ir-192, etc.) are widely used as brachytherapy treatment sources. However, they have never been used as transmission-based external imaging source, because the energy level of most radionuclides is higher than the level of imaging X-ray tubes.

The possibility of an external radionuclide source used as a "local" imaging system is a very practical topic. A new treatment unit which combines imaging and treatment via a single radiation source could potentially be implemented in the future for image-guided radiation therapy (IGRT). In this context, patients are not required to use an external imaging modality to guide the brachytherapy treatment, so the dual-function radiation source can simplify the procedure and increase the efficiency. In addition, it will streamline the device and reduce cost significantly by not using an additional imaging system.

In order to make this new device possible, the following works need to be done. First of all, the Monte Carlo (MC) simulation should be used to verify the viability of this imaging method. We will specify Ir-192 as the radionuclide for the transmission-based imaging source, and a patient CT image set (breast with tumor) as the simulation source data. All simulation projections will be collected through a virtual detector. They will be reconstructed and compared to the original CT slices.

Next, an imaging assembly need to be designed and built in a physical laboratory setting. We will use microSelectron® (Nucletron - Elekta, Stockholm, Sweden) as the external imaging source and the detector of Simulix Evolution™ (Nucletron BV, Veenendaal, The Netherlands) as the imaging panel. A breast phantom (CIRS Inc., Norfolk, VA) will be placed on a rotary stage in between the source and panel. We will collect CBCT projections and perform the image reconstruction. The reconstructed images will be compared to the real CT images, which will further verify the feasibility of this imaging method. Finally, a preliminary 3-D conformal treatment plan will be drafted by using a commercial available TPS for future evaluating the treatment ability of Ir-192 source of this device.

CHAPTER 2

MONTE CARLO FBCT AND CBCT SIMULATION FOR BREAST IMAGING

2.1 Background of Monte Carlo Simulation for Medical Physics

Monte Carlo (MC) simulation is a computational algorithm that generates random objects or processes. The repeated random sampling will produce numerical results from certain probability distribution. It is often used to solve physical and mathematical problems. The strength of randomness and efficiency of calculations make MC applications available in broad areas, including industrial engineering and operations research, physical processes and structures, random graphs and combinatorial structures, economics and finance, and computational statistics (Kroese, Brereton, Taimre, & Botev, 2014).

The MC technique has become omnipresent in medical physics in the last 60 years. Rogers (2006) found out that the earliest paper published in this field is written by Kahn. The developing of MC techniques accompanies the developing of computers, since MC technique relies on heavy computations. To date, the MC simulation is the most commonly used method to model the transport of radiation particles. The simulation process reflects the physical reality. Source with spectrum distribution releases particles, and those particles travel certain distances, which are determined by a probability distribution depending on the total interaction cross section. When the particles collide with other particles or materials, they will be absorbed or scattered into another direction based on the

corresponding differential cross section (Kawrakow, 2000). This procedure is continued until all the particles are absorbed or leave the pre-defined geometry.

In the past two decades, various software packages based on the MC method for particle tracking have been continuously developed. Popularly used simulation packages include, namingly Geometry and Tracking 4 (GEANT4), Monte Carlo N-Particle Transport Code (MCNP), Penetration and Energy Loss of Positrons and Electrons (PENELOPE), and Electron Gamma Shower (EGS) (Grupen & Buvat, 2012).

2.1.1 GEANT4

The GEANT4 code system (Agostinelli et al., 2003) is a general purpose code developed for particle physics applications. It was designed and developed by an international collaboration, formed by people from different cooperating institutes, organizations, and universities. It can simulate transportation for different particles, such as protons, neutrons, and electrons. It can also build complex geometries and visualize those geometries and particle trajectories, through a variety of interfaces.

It is the foundation of Tomographic Emission (GATE) simulation toolkit for nuclear medicine application in PET and SPECT. However, compared to EGSnrc, the weakness of GEANT4 lies in its long computation time when electron transport is involved in some applications (Rogers, 2006).

2.1.2 MCNP

The MCNP system is maintained by a large team at Los Alamos National Laboratory (Los Alamos, NM). It was originally designed as a neutron-photon transport for reactor calculation, which induced many applications used outside of the medical physics field (Rogers, 2006). The MCNP system can be used for simulating the transport of neutron, photon, electron, or combination of any of them. It treats an arbitrary three-dimensional configuration of materials in geometric cells bounded by first- and second-degree surfaces and fourth-degree elliptical tori (X-5 Monte Carlo Team, 2008). It has a very powerful geometry package, which embedded the Electron Transport (ETRAN) code, for electron transport calculation. Since the MCNP system has a great flexibility, it runs considerably slower than EGSnrc (Rogers, 2006).

2.1.3 PENELOPE

The PENELOPE code is developed and distributed by the Nuclear Energy Agency (NEA), which is an intergovernmental agency that has 31 country members. Just like its name, the PENELOPE code was initially designed for positrons and electrons calculation only, and photons were introduced to the system later. Nowadays, this code has become more general for the simulation of coupled electron-photon transport. The simulation algorithm is based on a scattering model that combines numerical databases with analytical cross-section models for the different interaction mechanisms and is applicable to kinetic energies of particles from a few hundred eV to 1 GeV (Salvat, Fernández-Varea, & Sempau, 2008). The PENELOPE code package features detailed cross-section information for low-energy particles and a flexible geometry package for accelerator beams simulation.

2.1.4 EGSnrc

The EGS system has a long history compared to other MC codes. The ancestor of EGS appeared in the early-to-mid-1960's by two independent groups, one was written by Zerby and Moran at Oak Ridge National Laboratory (Oak Ridge, TN) and the other one was written by Nagel at University of Bonn (Bonn, Germany) (Bielajew, Hirayama, Nelson, & Rogers, 1994). Both of the initial codes can only simulate electron beams for some simplex geometry and phenomena. After almost 60 years development, from EGS1 to EGS4, The EGS system is the most widely used general purpose MC radiation transport package now.

EGS National Research Council Canada (EGSnrc) is a new generation package of the EGS system, which can simulate the radiation transport of particles in any element, compound, or mixture. The dynamic energy range of particles in the EGSnrc is from 1 keV to 10 GeV. It almost takes into account all physics processes which will happen in radiation transport, such as bremsstrahlung production, positron annihilation, Moller and Bhabha scattering, pair production, Compton scattering, photoelectric effect, etc (Kawrakow, Mainegra-Hing, Rogers, Tessier, & Walter, 2011). It is stable, accurate, and the simulation speed is faster than other MC packages (Rogers, 2006; Faddegon et al., 2009; Wang & Li, 2001; Chibani & Li, 2002).

EGSnrc contains numerous toolkits. The function egs_cbct is a new user code officially implemented into the EGSnrc since 2008. It is written by C++, and provides a fast estimation of the scatter contribution to an ideal detector in a CBCT setup by combining different variance reduction techniques (VRTs) and a smoothing algorithm (Mainegra-Hing & Kawrakow, 2008). It can also be used for estimating the total signal to

the detector or the signal's separated transmitted and scattered components. At the beginning, this user code was designed for the purpose of simulating a CBCT setup, but now it can also be used for modelling conventional CT scanner setups. egs_cbct can help reduce the simulation time significantly based on our lab hardware settings. Furthermore, considering that our proposed dual-function system uses Ir-192, which requires the high-energy photon transport simulation, the EGSnrc system is the most appropriate package to be used.

2.2 Photon Interaction

Photons are electromagnetic radiation, such as X-rays and gamma rays (Hubbell, 1999), with zero mass, zero charge and a velocity of the speed of light. Since photons are electrically neutral, atomic electrons or other charged particles will not affect their travel by coulombic force. They travel a certain distance and collide with other particles, leading to partial or total transfer of the photon energy to electron energy. These electrons will deposit their energy in the medium. Photons are much more penetrating than charged particles with similar energy level.

The general probability of photon interaction depends on photon energy and on the material photons are traveling in. The equation is:

$$N = N_0 e^{-\mu x} \qquad (2.1)$$

where N and N_0 are output and input photons, x is the distance traveled in a certain material, and μ is linear attenuation coefficient of the material (Figure 2.1).

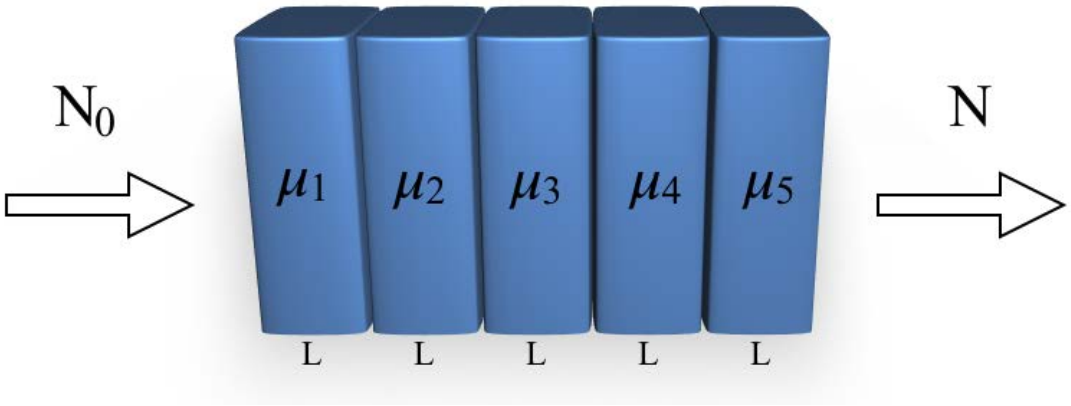

Figure 2.1 A schematic demonstrates photon attenuation. The general probability of photon interaction depends on photon energy and on the material photons are traveling in. N and N_0 are output and input photons, L is the distance traveled in a certain material, and μ_1 to μ_6 are linear attenuation coefficients of different materials

Since a linear attenuation coefficient is dependent on the density of a material, a normalization of the linear attenuation coefficient per unit density of a material that is called mass attenuation coefficient is often used. It produces a value that is constant for a given element or compound.

$$N = N_0 e^{-(\frac{\mu}{\rho})(\rho x)} \qquad (2.2)$$

where $\frac{\mu}{\rho}$ is mass attenuation coefficient.

2.2.1 Photoelectric Effect

Photoelectric effect usually occurs at the most tightly bound (inner-shell) of the atom. In this process, the incident photon completely disappears by transferring its energy

to an inner-shell electron, and the electron is ejected. This electron is named photoelectron. The energy of the emitted photoelectron is given by:

$$E(e) = hv - E(b) \qquad (2.3)$$

where h is planck's constant, v is the frequency of the photon, hv is incident photon energy and $E(b)$ is the electron binding energy.

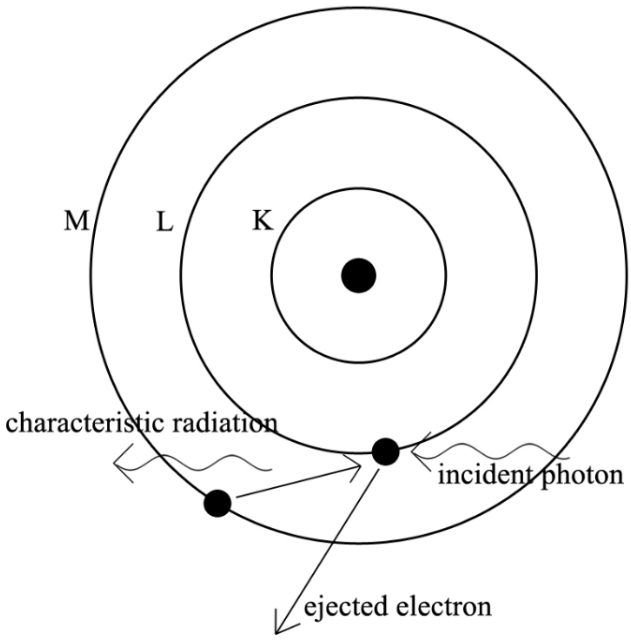

Figure 2.2 A schematic of photoelectric effect. An incident photon interacts with an inner-shell electron. The photon completely disappears by transferring its energy to the electron, and the electron is ejected. The electrons which originally stay at outer-shell will fill in the inner-shell electron vacancies and release characteristic radiation.

The ejected photoelectron ionizes other atoms in the tissue and loses its energy. The electrons which originally stay at outer-shell will fill in the inner-shell electron vacancies to stabilized the atom. Characteristic radiation or Auger electrons will be generated during this process (Figure 2.2).

In order to let the photoelectric effect occur, the energy of the incident photon is at least equal to or greater than the binding energy of the electron with which it interacts. The probability of photoelectric effect predominates at incident photon energy just above the k-edge binding energy (Huda & Slone, 2003). It decreases quickly when the photon energy (hv) further grows above the k-edge energy and increases significantly with atomic number of the materials (Z). This relationship can be shown in the following equation:

$$P(PE) \propto \frac{Z^3}{(hv)^3} \qquad (2.4)$$

2.2.2 Compton Scattering

In Compton scattering, incident photons interact with loosely bound outer-shell electrons. The incident photon is deflected to an angle θ with respect to its original direction, and the new scattered photon carries less energy than the original photon. The lost energy is transferred to the outer-shell electron (recoil electron), which travels with an angle ϕ. This energy varies from zero to a large fraction of the incident photon energy. All angles of scattering are possible. The recoil electrons deposit their energy in nearby tissues and contribute to the patient dose. The energies of recoil electron and scatter photon are given by (Metcalfe, Kron & Hoban, 2007):

$$E(e) = hv\left[\frac{\alpha(1-\cos\theta)}{1+\alpha(1-\cos\theta)}\right] \qquad (2.5)$$

$$E(p) = hv\left[\frac{1}{1+\alpha(1-\cos\theta)}\right] \qquad (2.6)$$

where $\alpha = \frac{hv}{m_0c^2}$, the ratio of incident photon energy (hv) to electron rest mass energy (m_0c^2=0.511 MeV). The scattered photon may move in any direction, even backscattered. The backscattered situation will result in the maximum recoil electron energy (Figure 2.3).

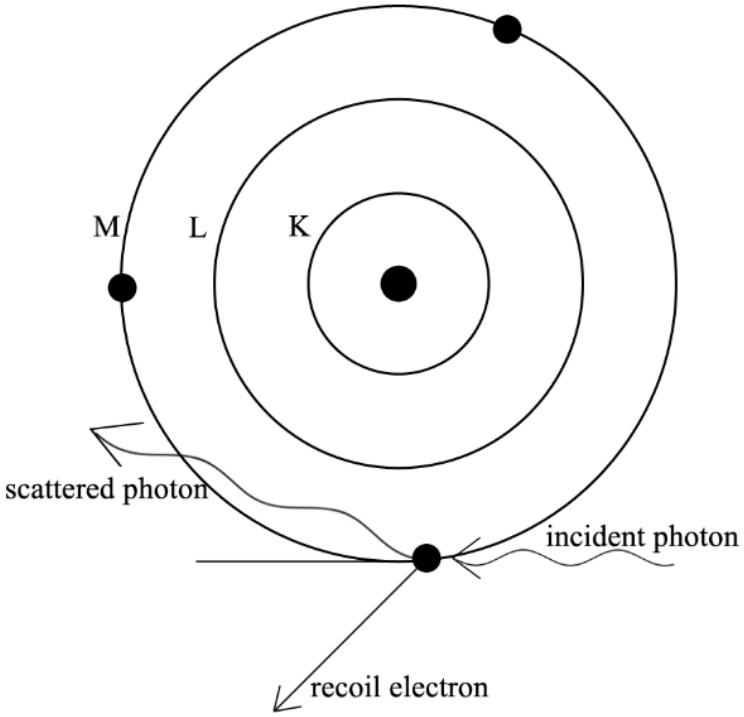

Figure 2.3 A schematic of Compton scattering. An incident photon interacts with an outer-shell electron. The photon is deflected to an angle θ with respect to its original direction, and transfer energy to the outer-shell electron (recoil electron), which travels with an angle ϕ. This energy varies from zero to a large fraction of the incident photon energy. All angles of scattering are possible.

Low binding energy electrons have higher possibilities of Compton scattering occurrence. The probability of this occurrence is proportional to the number of outer-shell electrons available in the materials and inversely proportional to the square root of the photon energy (hv) (Huda & Slone, 2003). The Compton scattering process is the most

important for energy absorption for soft tissues in the range from 100 keV to 10MeV. This relationship can be shown as the following equation:

$$P(Compton) \propto \frac{Z}{(hv)^{-\frac{1}{2}}} \qquad (2.7)$$

2.2.3 Pair Production

If a photon enters some materials with energy over 1.022 MeV, pair production may occur. When the photon passes near an atomic nucleus, the strong field effects from the nucleus convert the energy of the photon into a positron and electron pair. The kinetic energy that is shared between those two electrons is given by this equation:

$$E(e^+, e^-) = hv - 1.022 \qquad (2.8)$$

The positron interacts with a free electron after losing its kinetic energy (Figure 2.4). In this process, both particles are annihilated and two new photons each of 0.511 MeV are generated. Annihilation radiation is emitted in this conversion of mass to energy (Metcalfe et al., 2007).

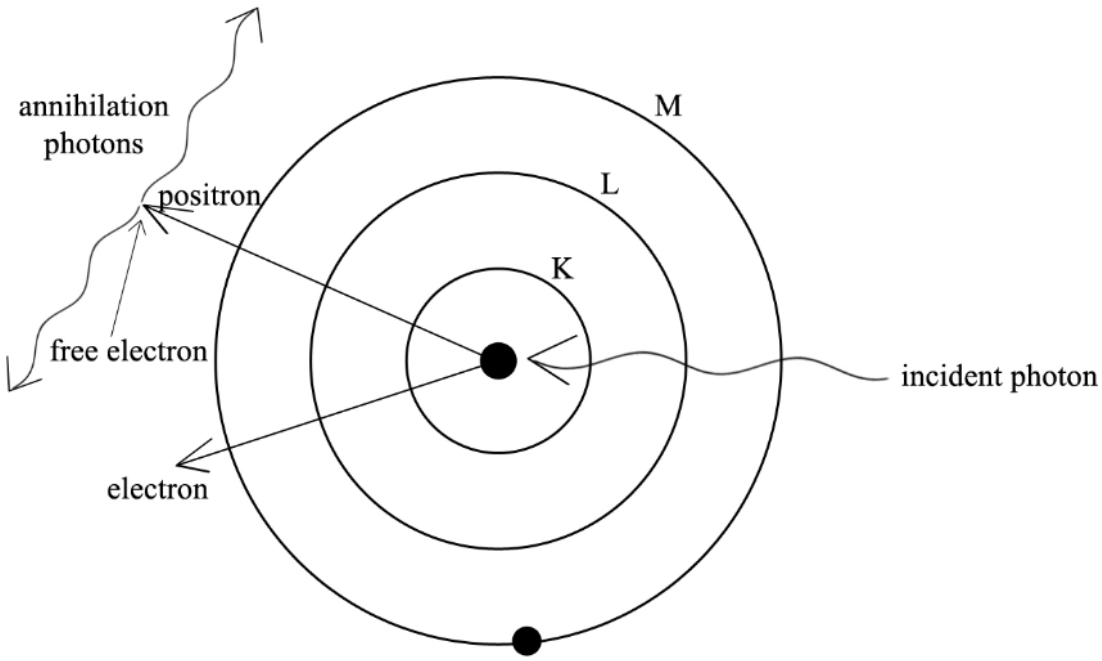

Figure 2.4 A schematic of pair production. An incident photon passes near an atomic nucleus. The strong field effects from the nucleus convert the energy of the photon into a positron and electron pair. The positron interacts with a free electron after losing its kinetic energy. In this process, both particles are annihilated and two new photons each of 0.511 MeV are generated. Annihilation radiation is emitted in this conversion of mass to energy.

Pair production probability depends on incident photon energy and materials atomic number. However, unlike like photoelectric effect and Compton scatter, the probability of pair production occurrence increases with higher energy. It is proportional to Z^2 and to the log of the incident photon energy (hv). This relationship can be shown as the following equation:

$$P(Pair) \propto Z^2 \log(hv) \qquad (2.9)$$

2.2.4 Coherent Scattering

Coherent scattering occurs when atomic electrons momentarily oscillate because of electromagnetic wave. The electrons vibrate at the same frequency as electromagnetic photons, which induce electromagnetic radiation to be emitted from all electrons in the atom. In this process, no energy is transferred to charged particles. Therefore we usually ignore the coherent scattering in radiotherapy, since its contribution is insignificant at energies above approximately 100 keV in soft tissues (Metcalfe et al., 2007). The probability of coherent scattering can be described as the following equation:

$$P(Coherent) \propto Z^{2.5}\log(hv)^{-2} \qquad (2.10)$$

2.3 Materials and Methods

In order to theoretically verify the possibility of using an external radionuclide source for imaging, MC simulation is the first step. We specified Ir-192 as the radionuclide for the transmission-based imaging source, and a patient CT image set (breast with tumor) as the simulation source data. All simulation projections were collected through a virtual detector. They were reconstructed and compared to the original CT slices.

2.3.1 Hardware and Software

Based on the previous discussion of the advantages and suitability of EGSnrc Monte Carlo system, we chose it for this work. The EGSnrc is installed in a desktop computer under Ubuntu 14.04 (Canonical Group Limited, London, UK) Linux operation

system (OS) with GNU Fortran and C++ compiler, Intel® Core™ i7 CPU (3.6 GHz × 8) processors (Intel Corporation, Santa Clara, CA) and 8 GB memory.

2.3.2 Simulation Experiment Setup

Using the proposed imaging system of Ir-192 as a proof of concept, we designed a virtual imaging model for simulation that consists of an Ir-192 radiation source, a collimator, a phantom of source data, and a data acquisition panel.

Ir-192 is a common and important treatment source used in breast brachytherapy. It is produced through neutron activation process (Eq. 2.11) from Ir-191 in a nuclear reactor. Ir-192 decays to platinum-192 (Pt-192) via beta decay (Eq. 2.12).

$$ {}^{1}_{0}n + {}^{191}_{77}Ir \rightarrow {}^{192}_{77}Ir + \gamma \qquad (2.11) $$

$$ {}^{192}_{77}Ir \rightarrow {}^{192}_{78}Pt + \beta^{-} + \gamma \qquad (2.12) $$

The average energy of Ir-192 is 380 keV and its half-life is 73.87 days (Marcu, Bezak, & Allen, 2012). In order to make the source easily accessible and manageable, the manufacturers usually produce the source in a special pellet. Most of the Ir-192 pellets from different manufacturers are cylindrical in shape. However, these source pellets have slightly different spectrum characteristics due to different lengths, diameters and encapsulation materials (Figure 2.5).

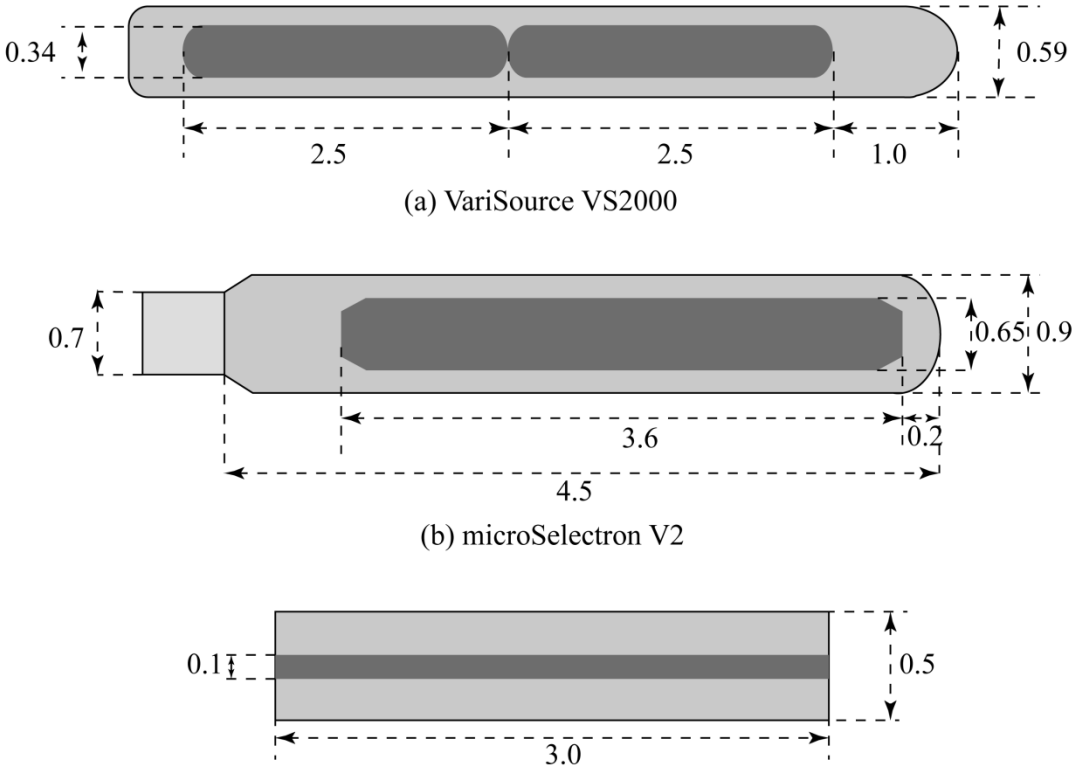

Figure 2.5 Diagrams of three Ir-192 source pellets from different manufacturers (unit in mm). The dark-gray area in the middle is Ir-192. (a) Source pellet from VariSource VS2000 from Varian Medical System (Palo Alto, CA, USA), (b) source pellet from microSelectron V2 from Nucletron B.V. (Veenendaal, Netherlands), and (c) source pellet from Best Industries Inc. (Springfield, VA, USA).

For example, VariSource VS2000 from Varian Medical System (Palo Alto, CA, USA) usually emits a spectrum with a little lower average energy than microSelectron V2 from Nucletron B.V. (Veenendaal, Netherlands), because the pellet is thinner (Rasmussen, Davis, Schmidt, Micka, & DeWerd, 2011). The pellets from Best Industries Inc. (Springfield, VA, USA) usually carry a higher average energy (Pérez-Calatayud et al., 2012) (Figure 2.6).

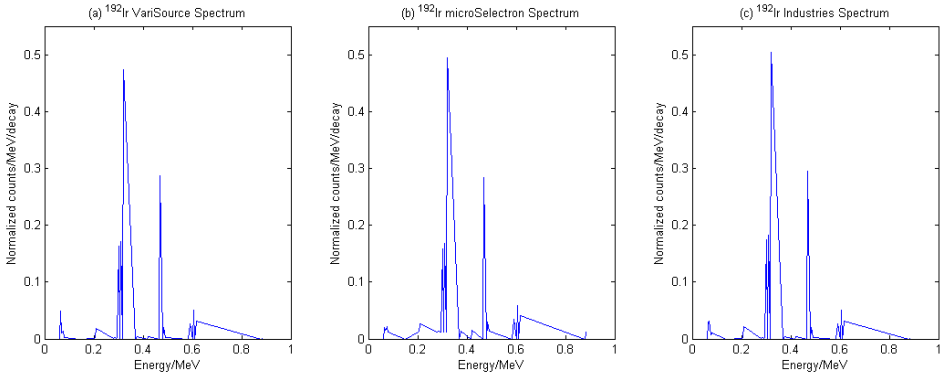

Figure 2.6 Spectra plots from different Ir-192 source pellets. The shield materials and configuration of pellets are different. VariSource VS2000 (Left) emits a spectrum with a little lower average energy than microSelectron V2 (Middle). The pellet from Best Industries Inc. (Right) usually has a higher average energy. We defined a point source with VariSource VS2000 spectrum for the simulation.

For our MC simulation, we generated a photon point source with the VariSource VS2000 spectrum. The point source is located at the negative x-axis with a distance of 19 cm from the origin, which is the center of the breast (Figure 2.7). We limited the emitting direction of the photon to the positive x-axis.

A virtual collimator was set 5cm in front of the point source to limit the irradiated area. It is a square-shaped collimator centered at x-axis with 25.8 cm edge length (Figure 2.7). The particles transported outside of this area will be blocked completely. This collimator setup also saves computation time by irradiating only a certain area which reduces particle interaction times. In addition, by changing the shape of the virtual collimator, we can simulate different CT models. For example, a strip collimator can be used to simulate fan beam computed tomography (FBCT) and a square collimator for CBCT.

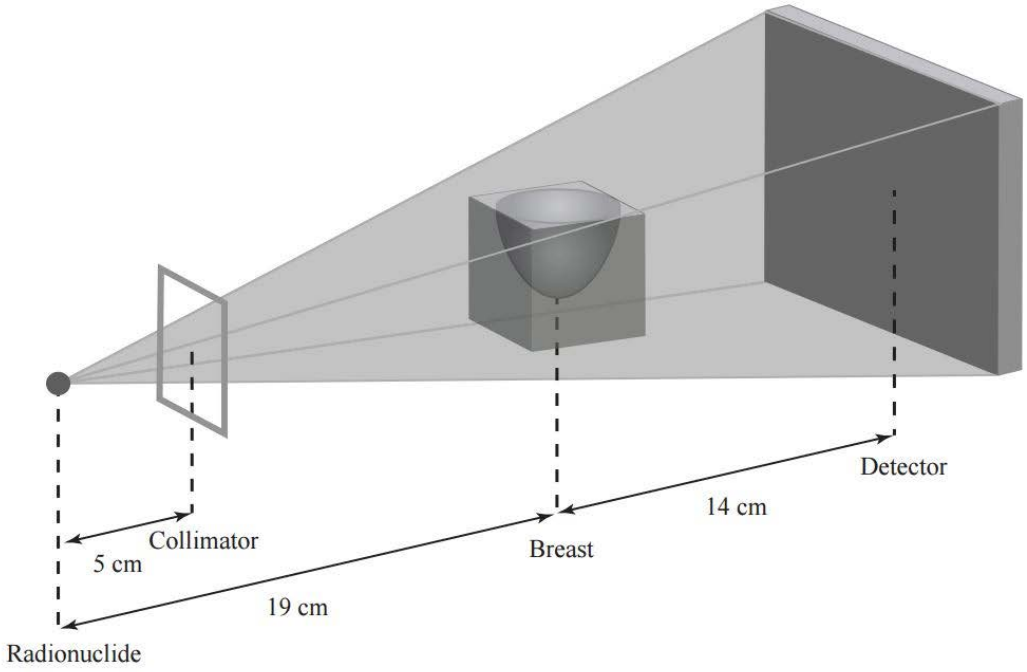

Figure 2.7 A schematic simulation geometry. A virtual point source with VariSource VS2000 spectrum was placed at the negative x-axis with a distance of 19 cm from the origin. A virtual squared collimator was set in front of the point source to limit the area being radiated. A virtual air detector with resolution 0.1 cm × 0.1 cm in dimension of 256 × 256 was centered at the positive x-axis with a distance of 14 cm to the origin. In this setup, we assume the detector is 100 % efficient, i.e., all photon energy that passes through the detector will be recorded as air kerma. The center of the breast phantom was defined as the origin of the geometry system.

A virtual air detector panel (Kawrakow, Mainegra-Hing, Tessier, & Walters, 2009) is centered at the positive x-axis with a distance of 14 cm to the origin (Figure 2.7). The dimension of each detector is 0.1 cm × 0.1 cm, 256 × 256 detectors for CBCT simulation and 1 × 256 detectors for FBCT on the data acquisition panel. In this setup, we assume the detector is 100% efficient, i.e., all photon energy that passes through the detector will be recorded as air kerma (Fang, Wu, Yang, & Zhao, 2015).

Real patient transverse plane chest CT data is used in the simulation. The original CT data has a resolution of 0.13 cm × 0.13 cm × 0.3 cm in dimension of 512 × 512 × 135

pixels. It contains the whole chest and breasts information of a female patient who was lying on the treatment couch in prone position (Fang et al., 2015). From the CT data set, we cropped a volume-of-interest (VOI) rectangular box that contains only the whole breast volume (Figure 2.8).

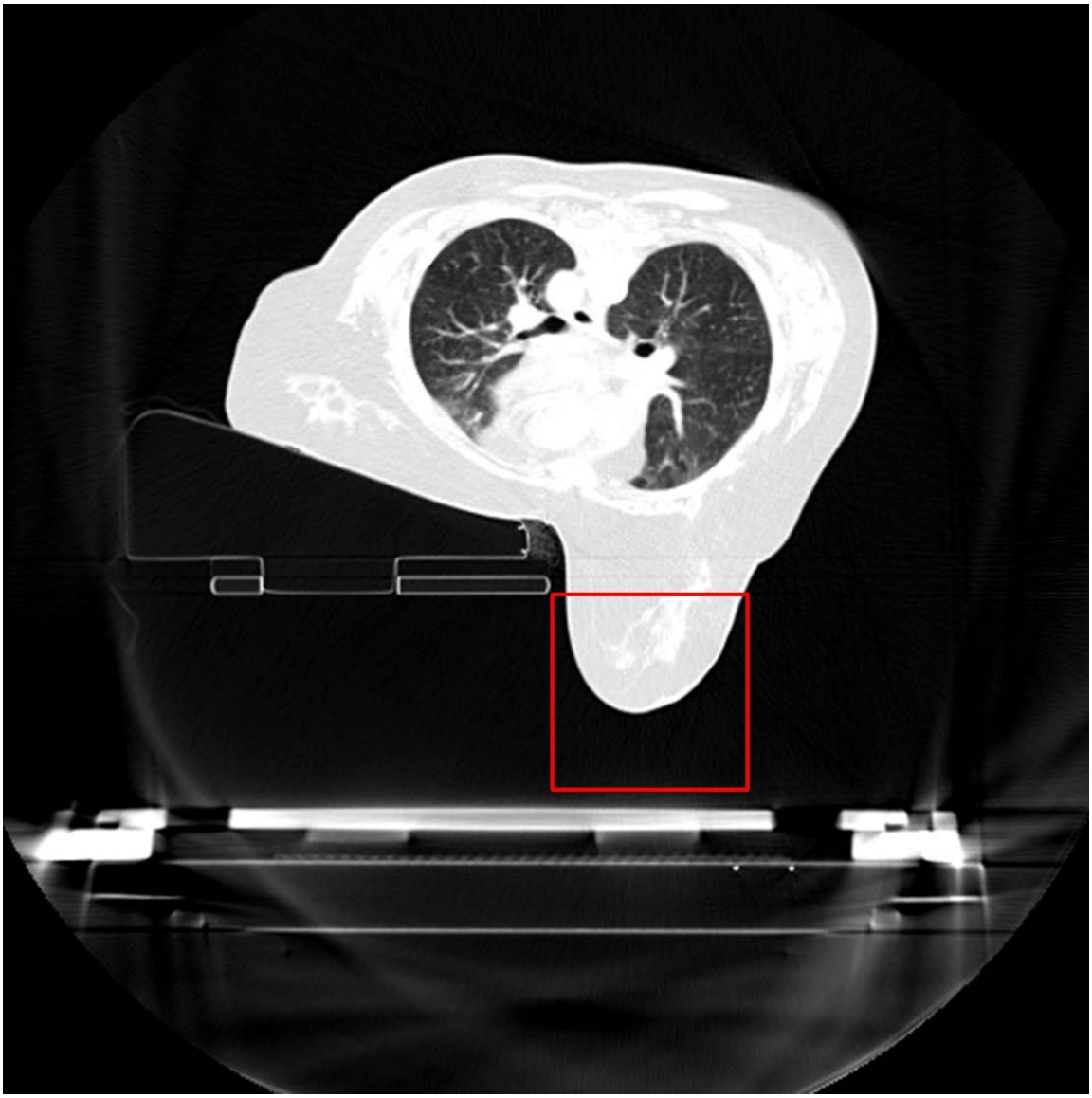

Figure 2.8 A slice of real patient transverse plane chest CT data used in the simulation. The original CT data has a resolution of 0.13 cm × 0.13 cm × 0.3 cm in dimension of 512 × 512 × 135 pixels. It contains the whole chest and breasts information of a female patient who was lying on the treatment couch in prone position. We cropped a red VOI rectangular box that contains only the whole breast volume.

A total of 47 slices were used for simulation. The cropped CT data forms a breast phantom with pixel size of 110 × 110 × 47 in correspondence to a cube of 14.3 cm × 14.3 cm × 14.1 cm. We then converted the CT number of each voxel to density value based on the CT ramp function (Saw, Loper, Komanduri, Combine, Huq, & Scicutella, 2005). This breast phantom is used for MC FBCT and CBCT simulation. The phantom's center is defined as the imaging model's geometry center. A schematic of the imaging model's geometry is shown in Figure 2.7.

2.3.3 Simulation Parameters

Considering the real-space setting and computation efficiency, we specified simulation parameters as follows.

(1) The lowest photon energy permitted in this simulation is 1 keV by setting PCUT = 0.001 (photon transport cutoff energy, unit is MeV), where all photons with kinetic energy lower than 1 keV will be abandoned in this geometry during particles simulation.

(2) Since electrons do not contribute to the signal collected by the virtual detector, they were not allowed to transport in the system by setting ECUT = 1 (electron transport cutoff energy, MeV), which is higher than the maximum photon energy in the calculation (Thing & Mainegra-Hing, 2014).

(3) XCOM photon cross-sectional compilation was used in the simulation (Berger & Hubbell, 1987); it provides total cross sections and attenuation coefficients as well as partial cross sections calculation. At this energy level of radiation,

coherent (Rayleigh) and incoherent (Compton) scattering were the main interactions in the phantom.

(4) The typical manufacture-provided initial activity of Ir-192 is approximately 3.7 × 10^{11} Bq (Goetsch, Attix, Pearson, & Thomadsen, 1991), which indicates about 370 million atoms disintegrating per second. Considering the hardware settings of our lab, in order to emulate the real transportations and to result in relatively good-quality projections, we set one billion particle histories for simulation (1 particle transportation = 1 particle history).

(5) Source and detector rotate around the imaging center (the center of the breast) 360 degrees with 1 degree interval.

The simulation process originally took about 5 days (120 hours) for the CBCT simulation based on the set up mentioned above. On the premise of keeping the quality of projections, we applied several methods of efficiency improving techniques (EITs) in combination with de-noising algorithms (Kawrakow, 2002), including force detection (Mainegra-Hing & Kawrakow, 2010) and delta transportation (Lux & Koblinger, 1991).

Force detection technique can increase the scoring efficiency. Compared to the traditional photons scoring method that saves all photons across the detector, force detection only records the photons that have the potential to move in the direction of the detector. It predicts the photon trajectory and abandons the ones that will not hit the detector. Furthermore, an exact ray-tracing algorithm is implemented to account for the attenuation through the phantom.

Delta transportation is also called Woodcock tracing. It transports those photons which are not aiming at the detector. In order to implement this technique, we need to specify the most attenuating medium in the geometry, which provides the maximum interaction cross section σ_{max}. This medium is breast tissue in this study. For the photons whose transported direction locates outside of the detector, the particle interaction in the pre-defined medium will be skipped. A probability of $1 - \frac{\sigma}{\sigma_{max}}$ is used for this interaction. This technique can reduce the estimation time for the photon scatter phenomenon, which contributes to the CBCT scan.

The de-noising algorithm decreases the statistical noise when the simulation histories are not sufficient. This algorithm is based on Savitzky-Golay filter with adaptive window size. Three parameters are required to be defined here for our simulation,

(1) *nmax* = 10, is the maximum allowed window size in one dimension

(2) *nmax2d* = 6, is the maximum allowed window size in two dimensions

(3) *chi2max* = 20, is the threshold for the chi-square test

By implementing this algorithm, it uses *nmax*'s value first, and then uses *nmax2d*. The *chi2max* is used to determine whether this algorithm is applicable to a pixel value without losing the original image's information. Research by Kawrakow (2002) evaluates the effects of these three parameters, and emphases that *nmax* must be smaller than *nmax2d*.

In addition, the fixed splitting technique, one of VRTs, was used to increase the number of scoring particles (Mainegra-Hing & Kawrakow, 2010). This technique requires two user inputs: the primary splitting numbers (N_p = 200) and secondary splitting numbers (N_s = 6000). A primary photon will be split N_p times when a scatter event occurs. This

splitting will reduce the statistical weights by a factor of N_p. Russian Roulette is used for the scattered photons that are not targeting the detector by a survival rate of $1/N_s$. In order to keep the statistical weights of scattered photons constant at the detector, the subsequent scatter events of the survival photons from Russian Roulette will be split by a factor of N_s.

2.3.4 Imaging Collection and Reconstruction

After implementing these techniques, the total simulation computation time for CBCT was significantly reduced to 40 hours. Figure 2.9 shows one slice of FBCT radon image and one CBCT projection with one billion particle history.

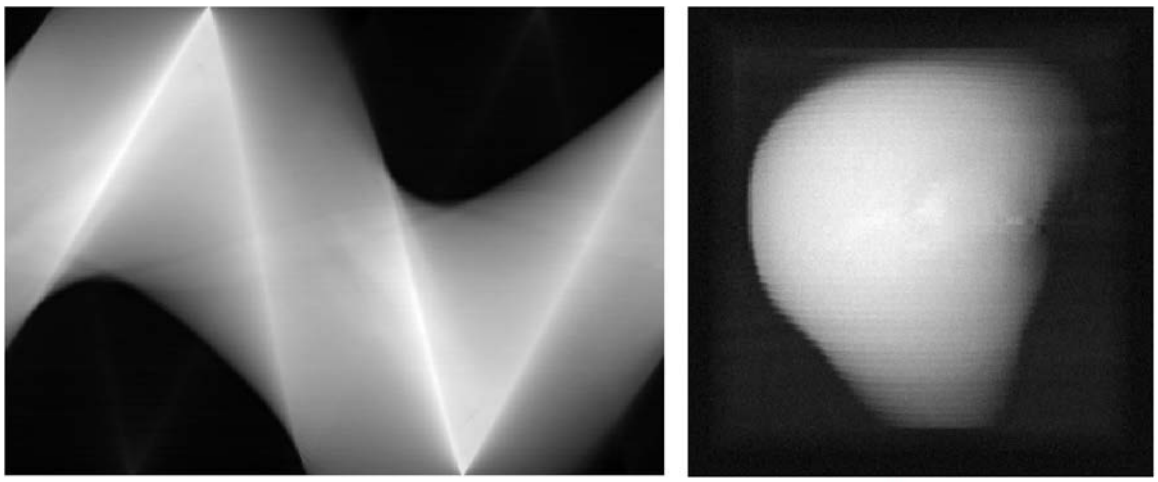

Figure 2.9 Sample simulated FBCT and CBCT projections. (a) is a FBCT radon image from one slice of phantom data. The x-axis indicates rotation angles from 0º to 360º, and the y-axis is the open fan angle. (b) is one projection of CBCT at a certain angle. The total data set for reconstruction includes 360 similar projections from different angles.

When all the projection data were collected, the Feldkamp-Davis-Kress (FDK) algorithm (Feldkamp, Davis, & Kress, 1984) was used for CBCT image reconstruction and the MATLAB's *ifanbeam* command was used for FBCT image reconstruction. We applied two filters to the projections to reduce the noise. One of the filters is a low-pass filter, which is an adaptive Wiener filter with a size of 5 × 5 pixels to estimate the local image mean and standard deviation, by using the following equation (Lim, 1990):

$$b(n_1, n_2) = \mu + \frac{\sigma^2 - v^2}{\sigma^2}(a(n_1, n_2) - \mu) \qquad (2.13)$$

where $a(n_1, n_2)$ and $b(n_1, n_2)$ are input and output images within a neighborhood of 5 × 5 pixels, μ is the local mean, σ is the local variance and v is the noise variance. The filter was used to remove the constant power additive noise. The other filter is an edge enhancement filter based on the unsharp masking technique, which improves the contrast of projections by subtracting a blurred image from its original (Figure 2.10).

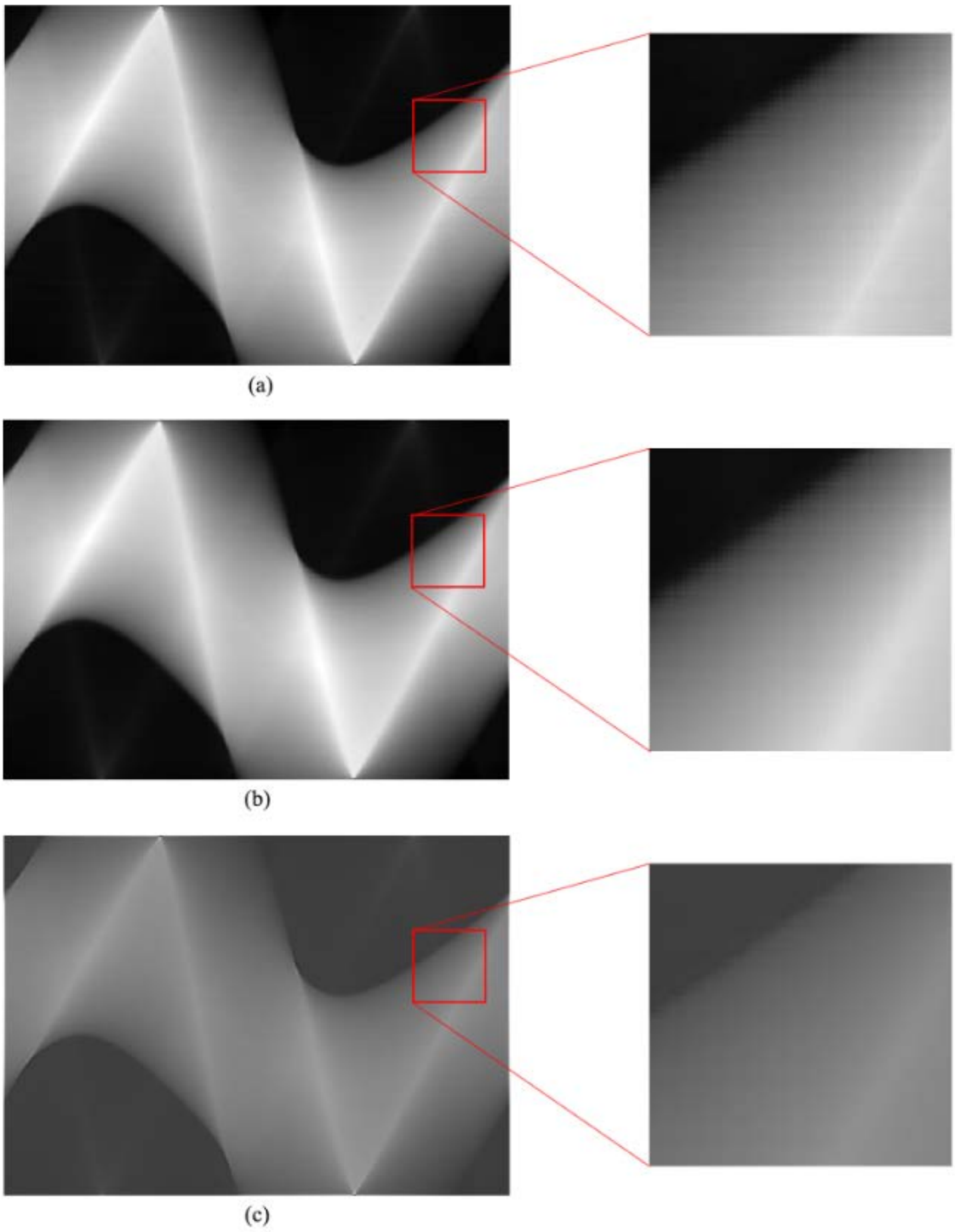

Figure 2.10 The results of FBCT projection after filtering. The x-axis indicates rotation angles from 0 to 360°, and the y-axis is the open fan angle. (a) Original FBCT radon image from one slice of phantom data. (b) Result of a filtered by a 2-D 5 × 5 Wiener low-pass filter. (c) Result of (b) filtered by an edge enhanced filter to sharpen the image.

2.4 Results

A total of 47 corresponding images were reconstructed by using 16920 FBCT projections (360 × 47) and 360 CBCT projections for the whole breast phantom. Among these 47 images, 16 of them have high-density areas, which are similar to the original CT slices. Some original CT slices and their corresponding FBCT- and CBCT-reconstructed images are displayed in Figure 2.12.

Figure 2.11a shows one of the cropped CT slices (the number 27 slice from cranial to caudal direction) where the high density area (lesion) is shown in bright pixels. The reconstructed FBCT (Figure. 2.11b) image corresponding to the original CT slice shows a similar result. The corresponding CBCT-reconstructed image marked is shown in Figure. 2.11c. Compared to the original CT slices, resulting images from both FBCT and CBCT reconstructions are able to differentiate the lesion areas clearly. However, due to the scattering effect, CBCT-reconstructed images contain more blur and noise than FBCT images. The lesion areas in FBCT-reconstructed images have a sharper edge.

Figure 2.11 Original CT image, FBCT-reconstructed image, and CBCT-reconstructed image are all at the corresponding sagittal level. (a) The original CT slice shows a high-density area (lesion) by bright pixels. (b) The corresponding FBCT-reconstructed image. (c) The corresponding CBCT-reconstructed image. We used pseudocolor to display the reconstructed images. Red represents high density and green represents low density in the image. Compared with the original CT slices, lesions in both FBCT- and CBCT-reconstructed images can be visually distinguished. However, due to the scattering effect, CBCT-reconstructed images contain more blur and noise than FBCT images.

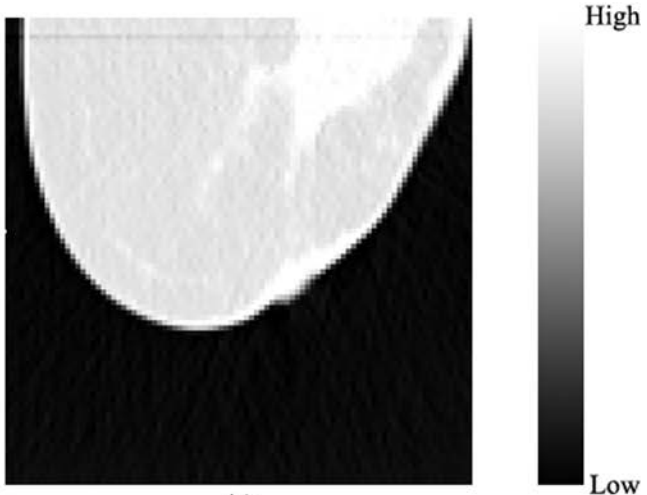

(a)

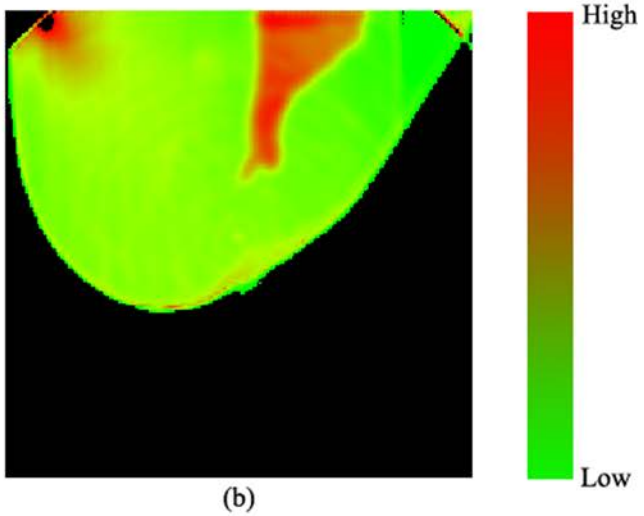

(b)

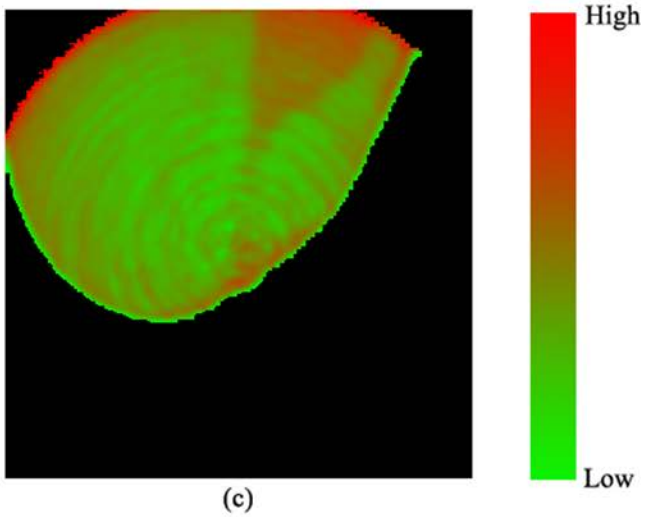

(c)

2.5 Discussion

Through the MC simulations, both FBCT- and CBCT- reconstructed images contained ring artifacts and CBCT results were affected more than FBCT's. Several reasons of ring artifacts may explain this phenomenon. First of all, energy received by adjacent pixels on the detector panel should be similar in theory. However, low simulation history is not able to provide sufficient "emissions" for the whole detector panel. In reality, the initial activity of Ir-192 source is 10 Ci, which equals to 3.7×10^{10} (37 billion) disintegrations or nuclear transformations per second. For our simulation, one billion particle histories are only equivalent to 0.26 second of Ir-192 activity, so increasing simulation history will absolutely increase the projection quality. Thus, we also simulated ten billion particle histories and the results are shown in j, k, and l in Figure 2.12. The ring artifacts were dramatically removed. However, due to the hardware limitation in our lab and high particle history inducing extremely long calculation times, it is not feasible for us to simulate with an even higher particle history. Figure 2.13 shows the comparison of simulated projections with different particle histories. One can see the noise level reduces intensely with particle history increasing.

Figure 2.12 Part of the reconstruction results and their corresponding original CT data. (a), (b), and (c) are three slices with varied high density features from different scan depth of original CT. (d), (e), and (f) are FBCT-reconstructed images and (g), (h), and (i) are CBCT-reconstructed images from one billion particle histories MC simulation projections, which corresponds to (a), (b), and (c). (j), (k), and (l) are CBCT-reconstructed images from ten billion particle histories. High density areas are shown in bright pixels in those images. Compared to the original CT slices, both FBCT- and CBCT-reconstructed results can distinguish high density areas clearly. However, due to the scatter effect, CBCT-reconstructed images contain more blur and noise than FBCT's. The high density areas in FBCT-reconstructed images have smoother edge and more detail information, resulting in better quality.

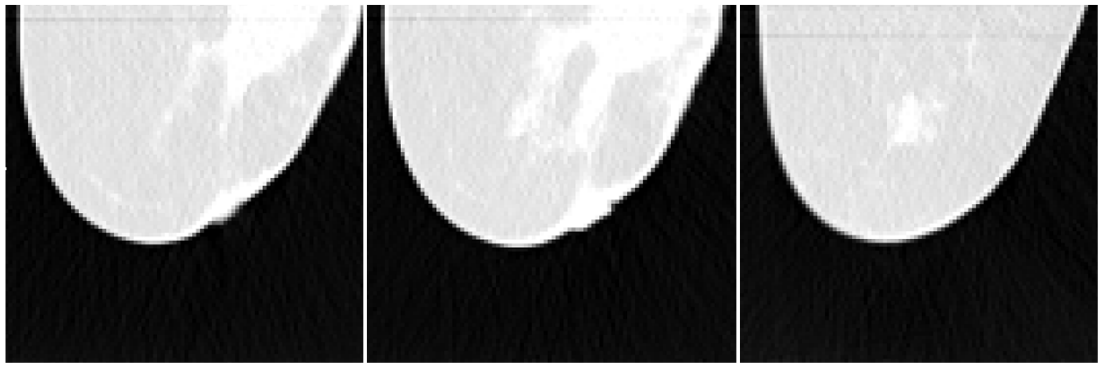

(a) (b) (c)

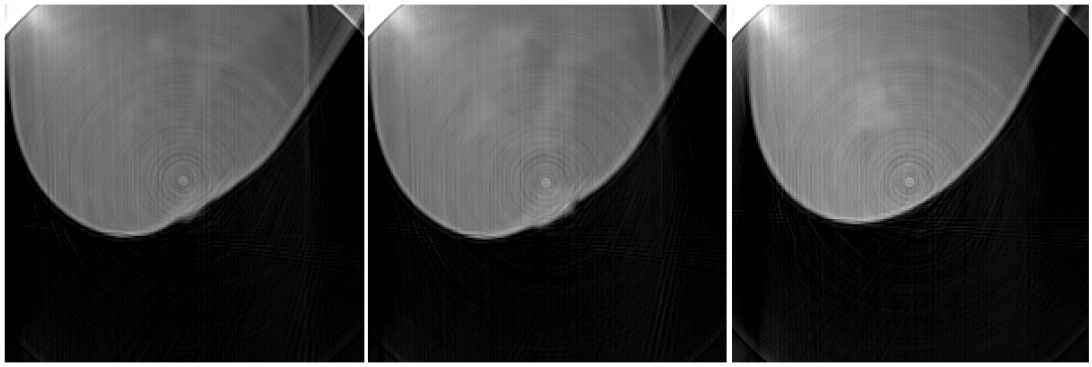

(d) (e) (f)

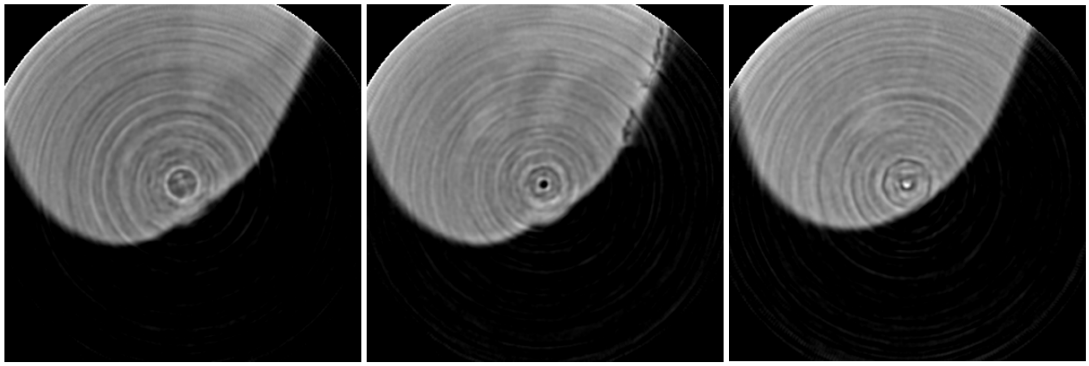

(g) (h) (i)

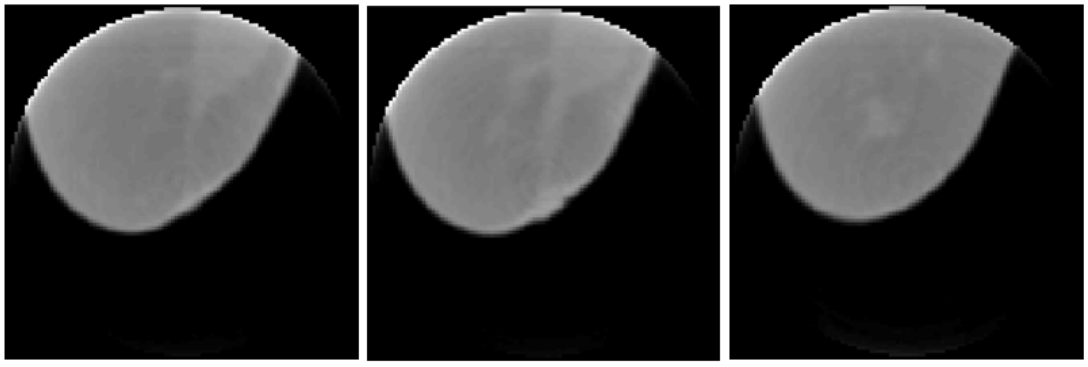

(j) (k) (l)

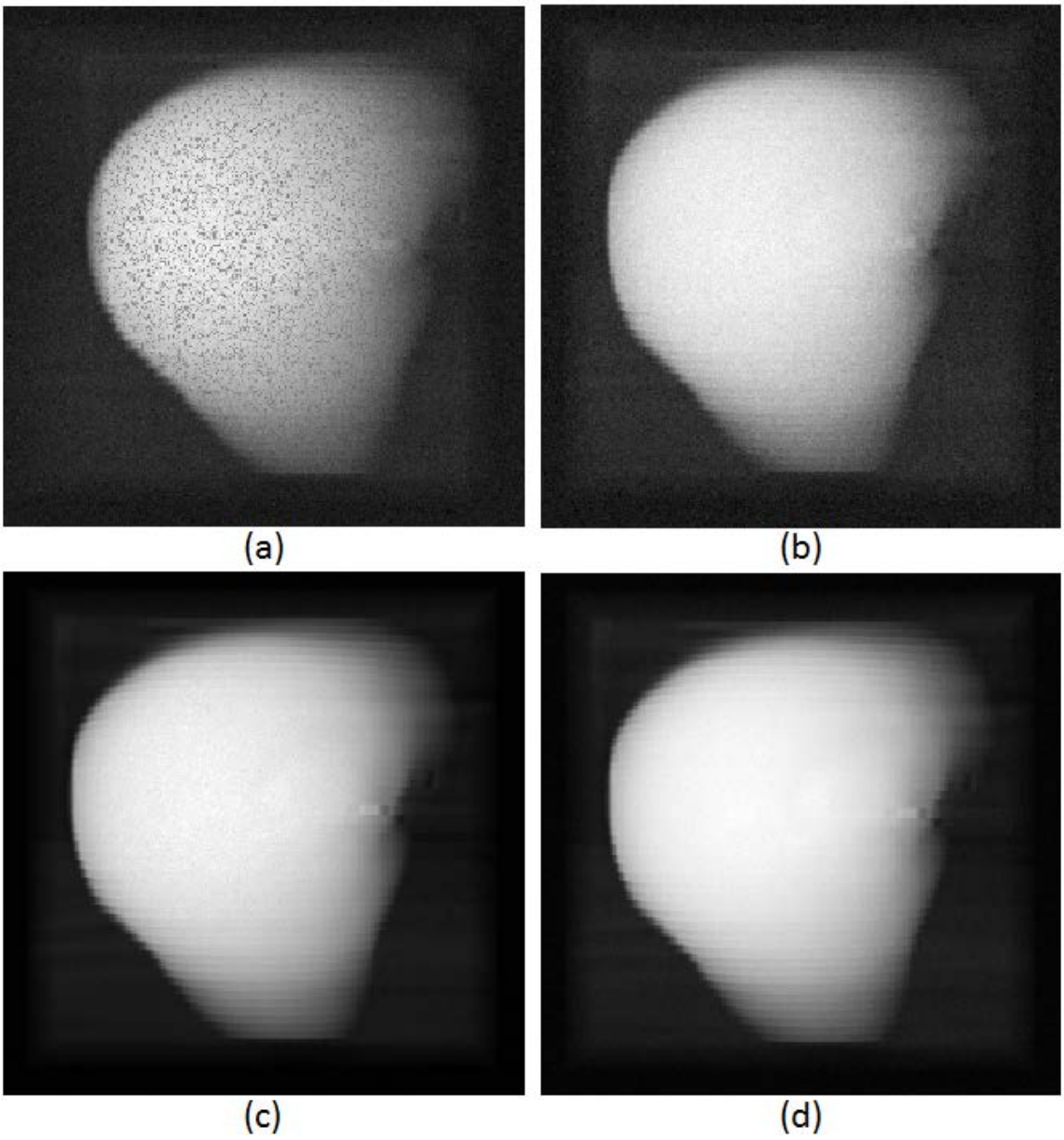

Figure 2.13 Comparison of projections from different simulation particle histories. (a) 6 million particle histories. (b) 60 million particle histories. (c) 600 million particle histories. (d) 6 billion particle histories. It is obvious that the noise level reduces intensely with particle history increasing.

Secondly, the intensive Compton scattering effect from the interaction between high-energy particles and breast tissue produced intensive noise on projections. Since particles in CBCT went through the entire breast phantom and most scatter photons hit the

detector panel, compared with only one slice in FBCT, the noise level was much higher than in FBCT. Figure 2.14 shows the simulated projection without scatter photons, projection with scatter photons only, and projection with scatter photons. Evidently, the scatter photons contribute to the majority of noise to the projections.

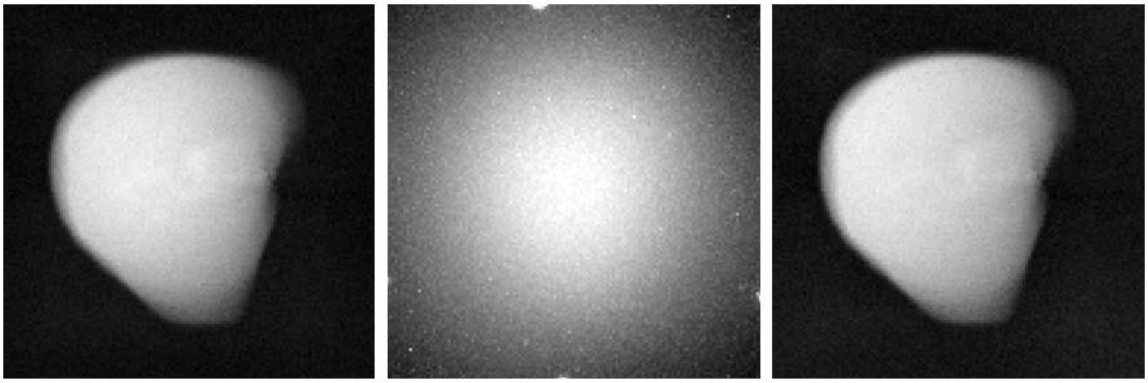

Figure 2.14 Scatter effects of simulated projections. (a) A simulated projection without scatter photons. (b) The projection of (a) with scatter photons only. (c) The final projection combine (a) and (b). The scatter photons contribute to the majority of noise to the projection.

Thirdly, the reconstruction algorithm may also affect the ring artifacts. In Figure 2.11 and 2.12, however, one can still relatively identify the lesion even with the artifacts. Additionally, we are able to reduce the scattering effect for CBCT simulation and increase the signal to noise ratio by increasing the number of histories. In simulation, the more histories are used, the more computation time is needed. VRTs and EITs are necessary tools since they can increase the efficiency by at least 5 folds of computation time for our simulation without losing the projection accuracy and quality.

On the other hand, brachytherapy requires an external imaging system to confirm the irradiation position in the current treatment procedure. Based on the simulation results,

we verified the feasibility that radionuclides can be used as a brachytherapy treatment source, as well as an external imaging source. If this imaging system was used to guide the treatment, the quality of image would not be so imperative, where the lesion's gravity center and volume would be the first priority and the detailed boundary information might be neglected. The dual-function radiation source can simplify the brachytherapy procedure and cut down the cost of an additional imaging system.

2.6 Conclusion

The MC method simulates breast FBCT and CBCT successfully by using radionuclides Ir-192 as an external source. Though there are ring artifacts, breast with high-density areas can be clearly distinguished in both reconstructed images. Radionuclides are potential radiation sources for imaging. We foresee the possible application in IGRT, through a dual-function radiation source that can conduct both imaging and therapy sequentially. The next step is collecting experimental data from a physical laboratory environment, and validating proposed method through laboratory application.

CHAPTER 3

DATA COLLECTION AND ANALYSIS UNDER LABORATORY SETTING

3.1 Background of Breast CT

Mammography has the advantages of a relatively good detection performance, short imaging time and low cost. It is the most widely used imaging modality for breast cancer screening. However, mammography has the limitation of low sensitivity in women with dense breasts (Kolb, Lichy, & Newhouse, 2002). Some other imaging methods are used in the clinical setting after a screening mammogram in order to gather more information of breast, including scintimammography, positron emission tomography, magnetic resonance imaging, optical imaging, microwave imaging, and ultrasonography (Boone, Nelson, Lindfors, & Seibert, 2001).

The development of digital mammography systems increases the possibilities of seeing dense breast, compared to old film mammography, because of its wider dynamic range. CT is not used very often for breast cancer diagnosis due to concerns about radiation dose and cost-effectiveness (Boone et al., 2001). Patients are required to lie on the bed during a conventional CT scan. Even if this scan is for breast, other parts of the body will also receive radiation, such as lung, head and neck. In addition, the respiratory motion may induce the blurring effect to the images. However, the reconstructed image quality of CT is much better than mammography, since we are able to analyze the 3-D information. Digital breast tomosynthesis and dedicated breast CT are two methods that being well accepted.

3.1.1 Digital Breast Tomosynthesis

Digital tomosynthesis is a 3-D imaging technology that uses a limited number of X-ray projections for reconstruction. It improves the diagnosis and detection of lesions. The chest and breast are two major sites that tomosynthesis focuses on (Chen et al., 2010), since both are usually diagnosed by traditional imaging methods of chest X-ray and mammography, which only provide 2-D information.

During the process of digital breast tomosynthesis, the X-ray tube moves in an arc and makes a series of exposures at slightly different angles. The technique detail from different manufacturers varies. The angle that the X-ray tube rotates between 11 degrees to 50 degrees, corresponds to a total of 9 to 25 projections (Lim & Maxwell, 2015). Two methods for projections/acquisitions are usually applied. One is continuous acquisition, where all projections are collected during the continuous tube movement. The other is “step and shoot”, where the tube stops at a certain angle and projection is collected. The continuous acquisition method has the advantage of short acquisition time, but it also has the disadvantage of lower imaging resolution than the “step and shoot” method. The dose of each projection is relatively small, so that the total dose of digital breast tomosynthesis is comparable to that of a traditional mammography (Lim & Maxwell, 2015).

The digital breast tomosynthesis imaging technology has been demonstrated as promising to provide greater sensitivity and specificity of diagnosis. Many studies have showed that by combining with mammography, the breast cancer detection rate increases with a significant reduction in false positive rates (Lim & Maxwell, 2015).

3.1.2 Dedicated Breast CT

Dedicated breast CT is currently being researched by many investigators (Boone et al., 2001; Chen & Ning, 2002; Tornai et al., 2003). They use cone beam detector system to build a potential breast CT. Boone's group in University of California, Davis, has the longest research history and is still constantly studying dedicated breast CT. Their prototype includes a water-cooled tungsten anode X-ray tube with a 0.4 mm × 0.4 mm focal spot and 0.3 mm of added copper filtration, a flat X-ray panel with a resolution of 1024 × 768 in dimension of 40 cm × 30 cm, and a bearing-motor-encoder system to rotate the tube and panel (Lindfors et al., 2008).

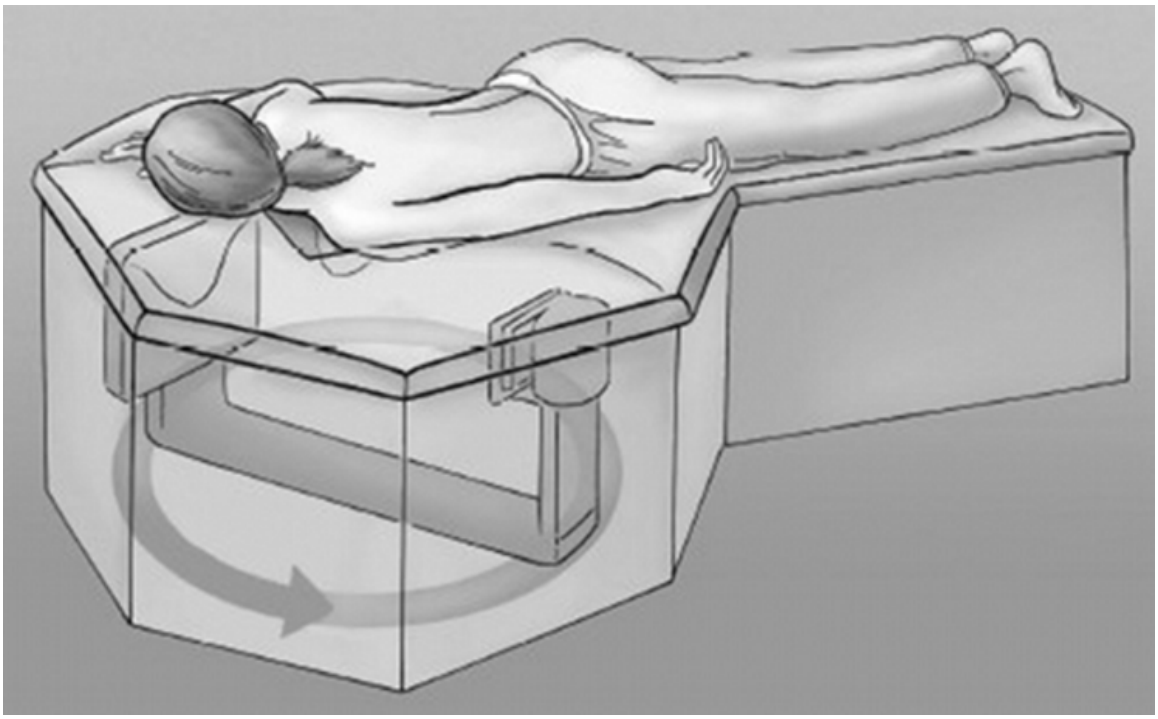

Figure 3.1 Illustration of how a breast CT works. Patient is in prone position on a couch with breast naturally dropping through a window. X-ray tube and imager are hidden underneath and rotate around the breast (Lindfors et al., 2008).

Patients are scanned in prone position (Figure 3.1). For a full 360-degree projection collection, it takes 16.6 seconds. Lindfors et al. (2008) published their initial clinical report of this system on 69 selected women patients. The outcome indicated that for the visualization of breast lesions, this dedicated breast CT had similar result as mammography. However, for the visualization of masses, dedicated breast CT had better result than mammography, and for microcalcification lesions, mammography is better. Prionas et al. (2010) did another clinical report by using this dedicated breast CT system with contrast materials injected on 46 women patients. They concluded that the conspicuity of malignant lesions and calcifications were significantly improved in contrast-enhanced breast CT compared to unenhanced breast CT and mammography.

3.1.3 High-Energy Level CBCT Solutions

The visualization of 3-D information of CBCT is used in IGRT for patient positioning and target localization in radiation therapy. Low energy levels kV CBCT, including 100 kVp, 110 kVp and 125 kVp (Ding, Munro, Pawlowski, Malcolm, & Coffey, 2010), are widely implemented in current clinical procedures. However, this kV system requires additional hardware components for a LINAC system. Due to the fast development of detector technology, portal imaging by using megavoltage (MV) treatment source became possible.

Using the treatment beam for imaging is attractive because this method does not require an additional hardware, which significantly reduces the expense and maintenance of the machine. Furthermore, the image is obtained in exact geometric coordination with the treatment, which helps to position the patients (Pouliot et al., 2005). Although the MV

source could reduce the imaging quality, researchers still developed MV CBCT because of the advantages of its 3-D information, lower cost and better geometric coordination. The MV source of the LINAC and the electronic portal-imaging device (EPID) are currently employed for MV CBCT imaging, such as the commercially available Siemens ONCOR MV CBCT (Siemens Medical Solutions USA, Inc., Malvern, PA).

3.2 Mechanical Phantom Design and Test

In order to build this proposed imaging/therapy assembly, we designed and built a mechanical CT simulation phantom from raw materials to mimic first-generation CT geometry and data collection. Part of this platform was used in our Ir-192 CBCT real data acquisition. We used a low power laser source and a light detector to simulate the X-ray tube and imaging signal receiver (Fang, Lupp, & Zhao, 2014).

3.2.1 Mechanical Phantom Design

The system includes the following components: a linear stage (T-LSR150A, Zaber Technologies Inc., Vancouver, Canada), a rotary stage (T-RS60A), a 10W laser module (VLM-532-43-SCB, Quarton Inc., Taiwan, China), a light detector (PDA36A, Thorlabs Inc., Newton, NJ), a data acquisition device (DAQ) (NI-USB 6221, National Instruments, Austin, TX) and a computer with LabView (National Instruments, Austin, TX) and Matlab (MathWorks Inc., Natick, MA) installed. The laser module and the light detector are mounted on a supporting beam that moves with the linear motion stage. The object to be scanned is placed on top of a disk that is moved by the rotation stage (Figure 3.2a). This

combination simulates the first generation CT machine (pen beam principle) (Figure 3.2b). The whole system is controlled by LabView software. The linear stage has a step resolution of 0.09921875 μm and the rotary stage has a step resolution of 0.000234375 degrees. The light detector has the ability to detect light signals over 350 nm to 1100 nm wavelength range.

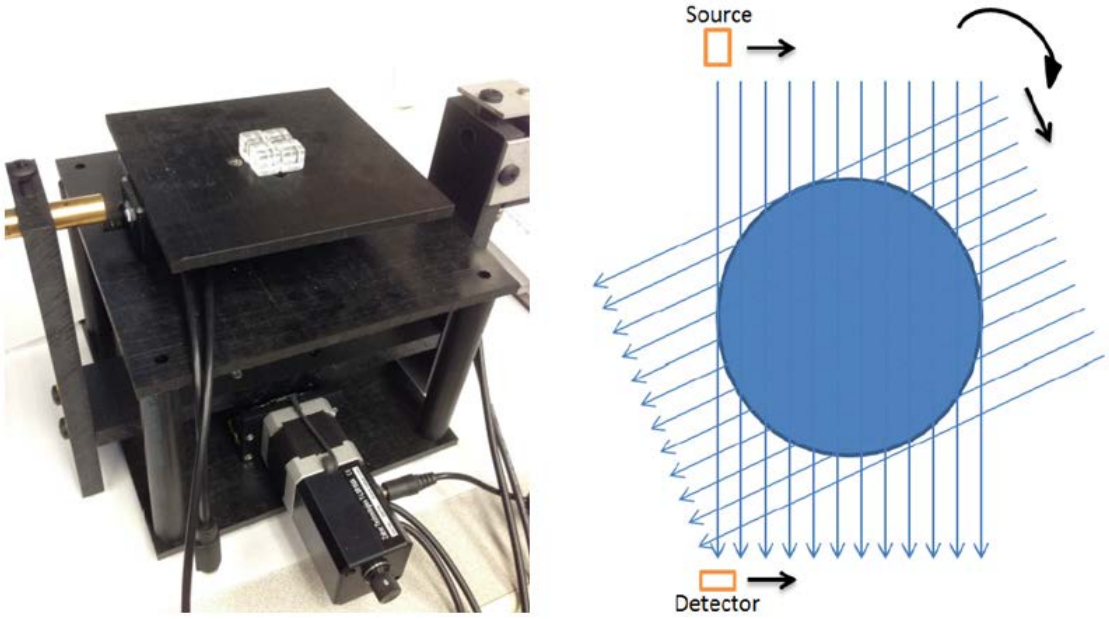

Figure 3.2 Mechanical CT simulation phantom. Left: A photo of our in-house platform which used a laser module and a light detector to simulate X-ray tube and imaging panel. Right: A schematic shows the first generation CT machine (pen beam principle).

Data collected by the DAQ from the light detector indicated the laser signal that passed through the object at every sampling location. LabView saved the data and then called Matlab to perform image reconstruction. Acrylic materials of different shapes with good optical properties were used for the system to verify the image reconstruction results. Speed of the motion stages, which simulated the movement of an X-ray head, and sampling rate, which simulated the number of radiation detectors, as well as other parameters were

adjusted by the operator through the system's graphic user interface (GUI) to obtain and observe results from various simulation inputs (Figure 3.3).

3.2.2 Mechanical Phantom Test and Results

Reconstructed images properly showed the original cross section shapes of scanned objects. Reconstructed images for individual cubic or cylindrical objects demonstrated better outcomes than other objects. The quality of the reconstructed image was affected by the laser energy, sampling rate, and movement interval. Higher energy level, higher sampling rate, and shorter movement interval improved the resolution and sharpness. When multiple objects were scanned, the reconstructed image showed some blurring effect due to the laser's reflection and refraction at the surface of the objects. In this phantom test experiment, a minimum of 10° rotation intervals and 2 mm linear movement intervals were necessary for a good reconstructed image (Fang et al., 2014).

This mechanical CT phantom system successfully simulated the first generation CT by using a laser module as an X-ray tube, and a light detector as an imaging panel. This phantom can be used in classrooms to demonstrate the CT's working principle. More importantly, it is a good prototype of our Ir-192 CBCT platform and can be implemented into this platform in the future.

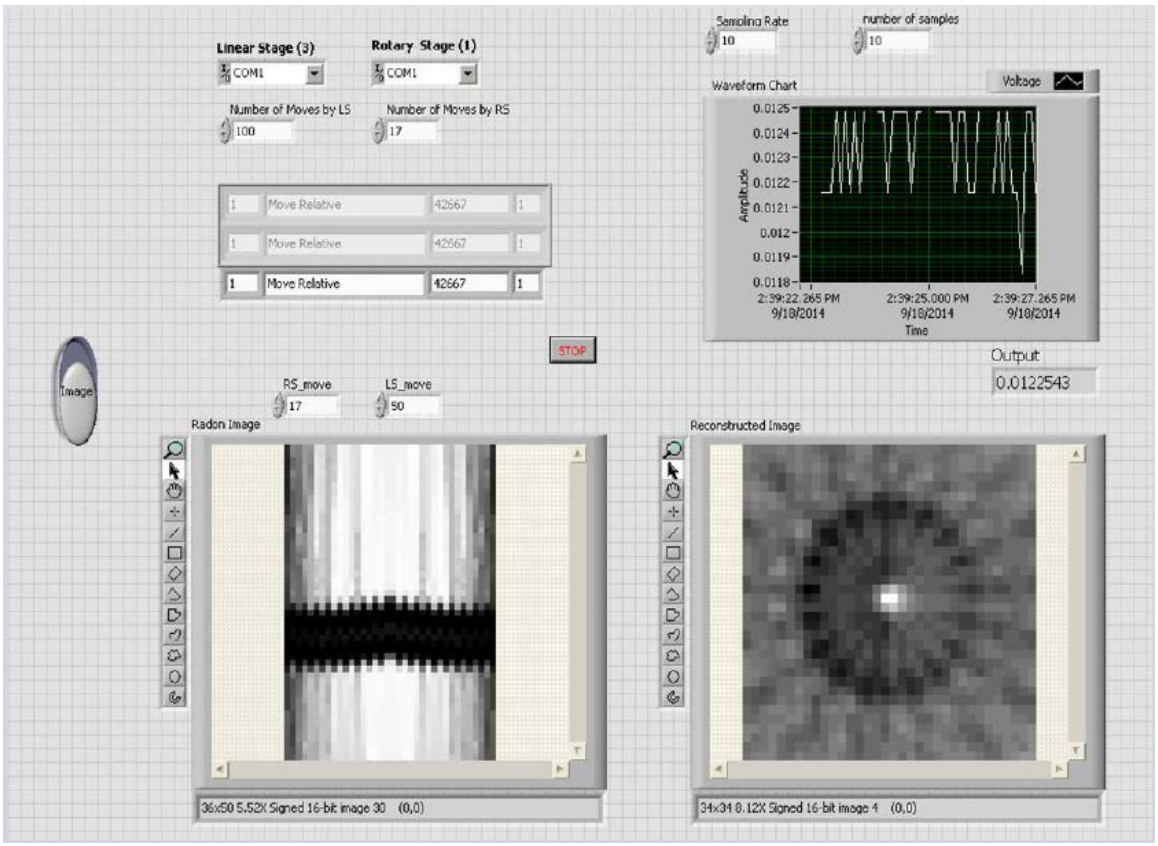

Figure 3.3 GUI of CT simulation platform. Top left: Data collection parameters. Top right: Real-time signal waveform chart. Bottom left: Radon image of one sample collection. Bottom right: Reconstructed image from previous radon image.

3.3 Materials and Methods

Short half-life radionuclides (F-18, Tc-99m, etc.) are usually served as internal emission-based imaging sources for diagnostic applications, such as PET and SPECT. Other high-energy level and long half-life radionuclides (Co-60, Ir-192, etc.) are widely used as brachytherapy treatment sources; however, they have never been served as transmission-based external imaging sources. In an attempt to utilize brachytherapy treatment sources for imaging purpose toward constructing an integrated platform for image-guided brachytherapy, we have successfully simulated breast FBCT and CBCT with

photons emitted from Ir-192 as an external source, via a MC technique. In this chapter, we accordingly designed and built an imaging assembly in a physical laboratory setting. We used the Ir-192 source from microSelectron® HDR remote after-loading unit (Nucletron - Elekta, Stockholm, Sweden) as the external imaging source and the amorphous-silicon panel on Simulix Evolution™ radiotherapy simulator (Nucletron BV, Veenendaal, The Netherlands) as the imaging detector. A breast phantom (CIRS Inc., Norfolk, VA) was situated on a house-made rotary stage in between the source and the imaging panel. We collected plane radiographic projections and performed CBCT reconstruction afterwards. The reconstructed images were compared to images from conventional thin-slice CT scanner to evaluate the image quality of this method. The whole model was designed and built in a treatment room which was specifically constructed for HDR to provide enough shielding.

3.3.1 Ir-192 Source

The microSelectron® Digital (Figure 3.4a) is one of the most popular HDR brachytherapy after-loading platforms. It contains an Ir-192 source with initial activity of about 10 Ci reloaded at a frequency of every three months (Davis, Parker, & Evans, 2013). Due to the design of the source pellet's geometry (length, diameter) and encapsulation materials (Figure 3.4b), the source emits its own unique spectrum which is shown in Figure 2.6.

(a)

(b)

Figure 3.4 A microSelectron® Digital (Nucletron - Elekta, Stockholm, Sweden) HDR brachytherapy after-loading system. (a) A photo of microSelectron used in this study at Lynn Cancer Institute (Boca Raton, FL). (b) A schematic of microSelectron V2 source pellet (unit in mm). The dark gray area in the middle is the Ir-192 alloy. The Ir-192 source emits photons with an average energy level of 380 keV.

In this real data acquisition experiment, a 132 cm catheter was used and connected to the channel three of microSelectron® Digital afterloader, allowing the source to be pulled out and pushed into a horizontal Leipzig applicator with an aperture diameter of 30 mm (Pérez-Calatayud et al., 2005). The Leipzig applicator was provided with a 1-mm thick protective plastic cap for using on the skin cancer treatment, but this cap was not used in our experiment. The applicator consisted of a cone-shaped tungsten/steel alloy with the source pellet located at the focal spot of the cone. The source had a distance of 15 mm to the surface of the applicator and moved into the applicator parallel to the surface (Figure 3.5). It served as the imaging source holder and collimator to confine the irradiated area. The applicator was held by a multi-angle fixation, and the fixation was attached to a stabilizing baseboard, which prevented the whole system from shifting. We adjusted the angle of the fixation to ensure that the surface of the applicator was parallel to the imaging panel, and also made sure the alignment of the center of the source was projected to the center of the panel.

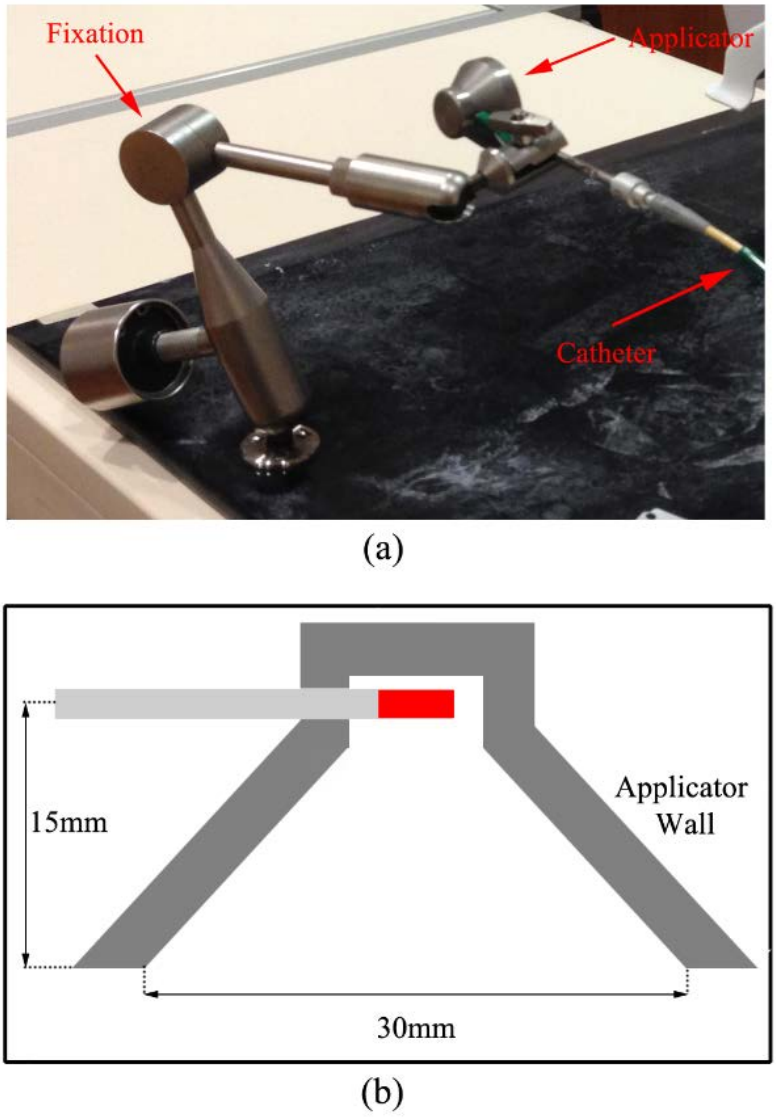

Figure 3.5 A horizontal Leipzig applicator. (a) A photo of the Leipzig applicator used as source holder is affixed on a multi-angle hydraulic clamp. The Leipzig applicator consists of a cone-shape tungsten/steel alloy. When in use, the source pellet will be located at the focal spot of the cone. It has an aperture diameter of 30 mm. (b) A schematic of the Leipzig applicator. The catheter transports the Ir-192 source (shown in red) into the applicator. The distance between the source and the surface of the applicator is 15 mm. The applicator works as an imaging source holder and collimator to confine and direct the irradiated area.

3.3.2 Breast Phantom

The center of the breast phantom (Model 073, CIRS Inc., Norfolk, VA) was located 310 mm from the surface of the applicator (Figure 3.6). The multi-modality breast phantom was designed for various aspects of breast imaging and image-guided interventional procedures. The phantom has a dimension of 12 cm × 10 cm × 9 cm with five cystic lesions embedded. It also includes a flexible Z-Skin™ membrane and special materials that simulates the human skin and breast tissue during scanning and biopsy. The "skin" and "tissue" material has remarkable self-healing properties. Instead of rotating the source and detector around the phantom like a conventional CBCT scanner, we rotated the phantom around the center of the rotary stage. The breast phantom was set on a board which was fixed to the rotary stage. The rotary stage was controlled by LabView software, which was installed on a laptop with Windows 8.1 OS. We built a GUI so as to control the rotary stage in a very flexible fashion (continuous mode, single step mode, absolute mode, relative mode, home mode etc.). The rotary stage communicated with the laptop through a serial/USB cable. In order to minimize the leakage of radiation, the cable went through the original conduit of the treatment room.

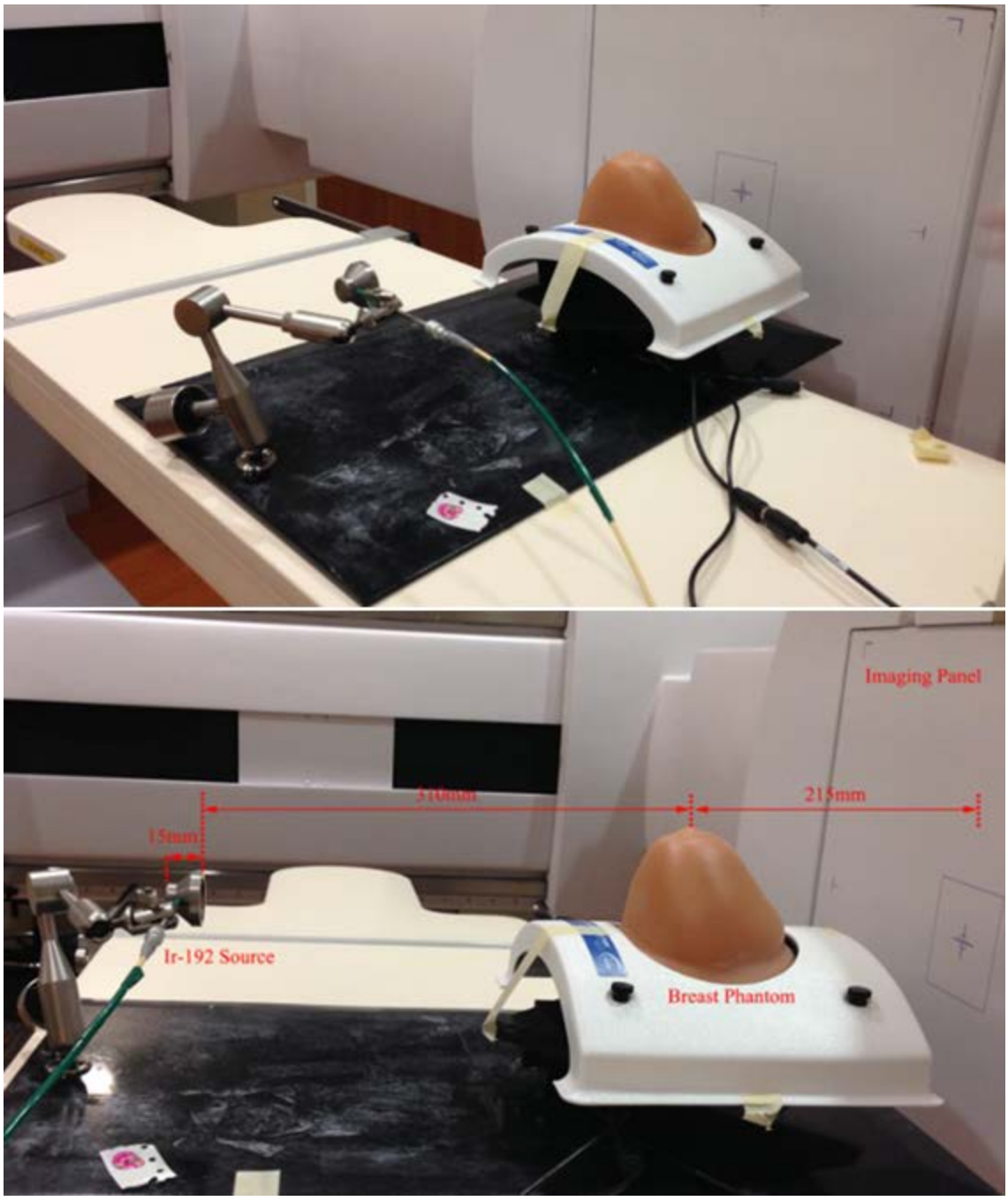

Figure 3.6 Imaging system geometry setup from different angle views. The breast phantom is placed on a rotary stage, which is in between the source and the imaging panel. Its rotating axis has a distance of 310 mm to the source holder, and 215 mm to the surface of the imaging panel. The panel has a resolution of 1024 × 1024 pixels on a 41 cm × 41 cm dimension (0.4 mm/pixel). The photodetector inside the panel has distance of 50 mm to the panel surface.

3.3.3 Imaging Panel

The radiotherapy simulator, Simulix Evolution™, can provide orthogonal radiographic images or CBCT images of brachytherapy patients for target localization in the treatment room immediately before the treatment starts (Reniers & Verhaegen, 2011). The system contains a 120 kV X-ray tube, an amorphous-silicon flat panel detector, and a treatment couch (Figure 3.7). The treatment couch was used in our experiment as a base to support the applicator and the breast phantom; it can move in 6 directions (vertical, lateral, and longitudinal). Since we used Ir-192 as an external imaging source, the X-ray tube was blocked by a stainless steel board to eliminate its influence. The imaging panel can function with two modes: fluoroscopy and digital radiography. It has a resolution of 1024 × 1024 pixels over a 41 cm × 41 cm dimension (0.4 mm/pixel). Over 1 million photodetectors are installed within the X-ray detector panel. Each detector has a sensitivity of 16-bit gray level (Sinha, Singh, Gurjar, & Bagdare, 2015). Therefore, depending on the intensity of photon energy received, each pixel can represent a maximum of 65,536 gray levels. We rotated the gantry 90 degrees to the horizontal position, so the surface of the detector was parallel to the surface of the collimator. The surface of the imaging panel was 215 mm from the center of the breast phantom (Figure 3.6).

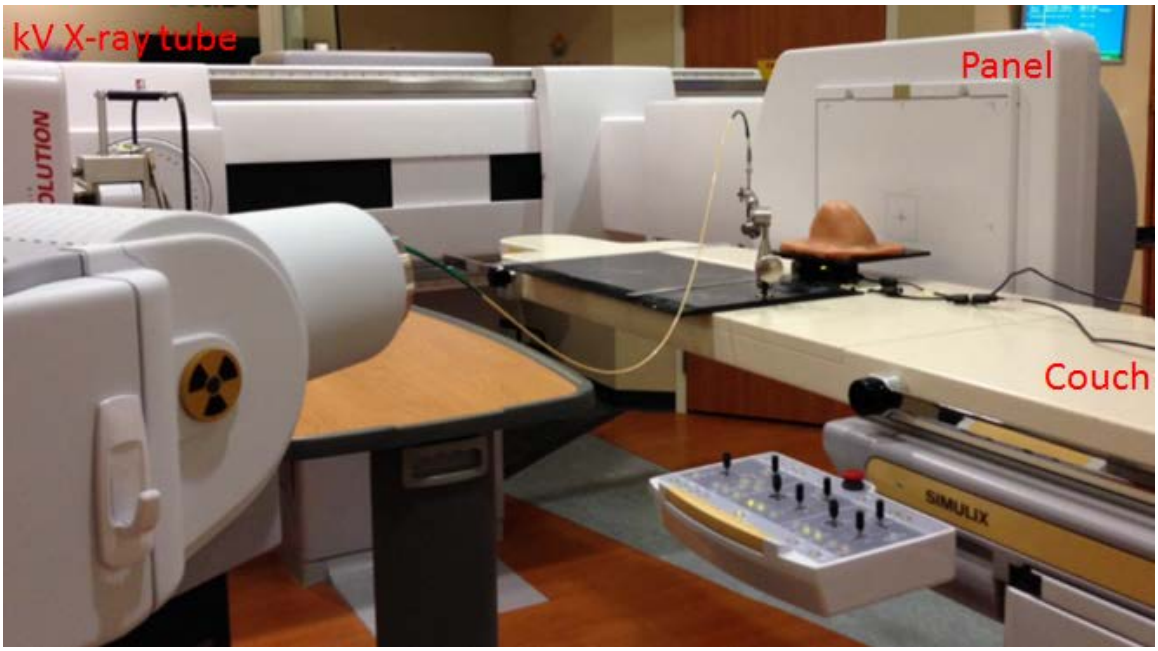

Figure 3.7 Simulix Evolution brachytherapy CT simulator. We rotated the gantry 90 degrees to the horizontal position in this figure, so the surface of the detector was parallel to the surface of the collimator.

3.3.4 Imaging Collection and Reconstruction

The co-alignment along the center of the imaging source holder, the rotating axis of the breast phantom and the center of the detector panel was carefully carried out prior to image acquisition. The console control room, where we performed data collection for the projections, was equipped with a radiation leakage detection device. Monitoring cameras in the treatment room were utilized to observe the source dwell position and the breast phantom rotation. The entire procedure is described as follows (Figure 3.8):

1. The Labview was used to control the rotary stage and set 0 degree as an initial position. We then rotated the breast phantom, which was fixed on the rotary stage, around its center clockwise by 360 degrees at 3-degree intervals.

2. The microSelectron® HDR after-loader was programmed to the maintenance mode. The Ir-192 can be pushed to the source holder at 132 cm, which was the end of the catheter as well as the focal center of the surface applicator. We then turned on the device. The Ir-192 source traveled to the dwell position and started irradiating.

3. Synchronized with the HDR source being pushed to position, the image was acquisition by the Simulix Evolution™ simulator in *digital radiography* mode, with exposure time set to 32 ms. In order to limit the effect of the kV X-ray tube, the tube was set to the lowest power outputs, which were 40 kV and 10 mAs. "PREP" button was pressed down at this moment to prepare for image acquisition. Projections were collected immediately when the source reached its dwell position by pressing down the "X-RAY" button without releasing "PREP" button. A total of 121 plane radiographic images were acquired, correlated to each of the 3-degree rotation intervals.

4. The HDR source was retracted from its dwell position back to the HDR afterloader after each image acquisition to avoid the detector panel's saturation.

5. All 121 images were read by the integrated Ocentra® (Nucletron BV, Veenendaal, The Netherlands) software at all rotation interval pauses. We exported these images from the system, and saved them as Digital Imaging and Communications in Medicine (DICOM) files for image analysis and reconstruction.

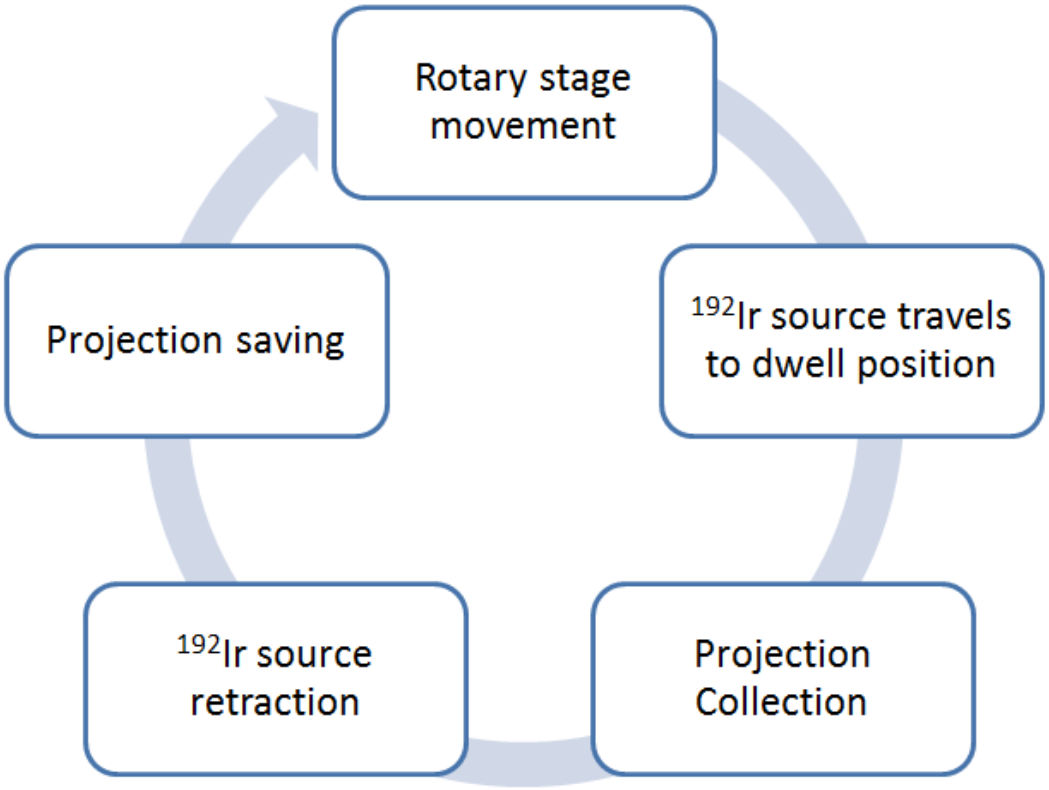

Figure 3.8 Radiographic image acquisition procedure flowchart. For one cycle of projection collection, after the rotary stage moved to a certain degree, the Ir-192 source was sent to the source holder. The image is subsequently captured and the Ir-192 source was immediately retracted afterward.

All projections were processed by the "minus logarithm" (Hsieh, 2003) to compensate for the intensity of the source, minimize the background noise, as well as invert the gray level of the projections. The processing is based on the equation below:

$$a = -\ln(\frac{I}{I_o}) \qquad (3.1)$$

where I is the intensity of an original projection, I_o is the intensity of a blank projection (Figure 3.9) without the breast phantom, and a is the resulting new projection after processing (Figure 3.10).

Figure 3.9 Blank projection used in this study. This image was taken without breast phantom on the rotary stage. It was used in "minus logarithm" to compensate for the intensity of the source, minimize the background noise, as well as invert the gray level of the images.

Due to the strong scatter effect caused by Compton scattering, the projections were very noisy. Again, we applied the pixel-wise low-pass filter (adaptive Wiener filter), which was based on statistics estimated from the local neighborhood of each pixel, for reducing the constant power additive noise. The filter's definition is based on the following equation (Lim, 1990):

$$b(n_1, n_2) = \mu + \frac{\sigma^2 - v^2}{\sigma^2}(a(n_1, n_2) - \mu) \qquad (3.2)$$

where $a(n_1, n_2)$ and $b(n_1, n_2)$ are input and output images within a neighborhood of 10 × 10 pixels, μ is the local mean, σ is the local variance and ν is the noise variance (Figure 3.10).

After both these pre-processed procedures, the images were ready for CBCT reconstruction, which were performed by FDK algorithm. Hann window filter (Equation 3.3) was used for FDK algorithm to reduce high frequency signals during the reconstruction (Lee et al., 2011).

$$W(\omega) = 0.5 + 0.5\cos(\omega) \qquad (3.3)$$

where ω is the spatial frequency of the image.

Figure 3.10 The results of a captured plane radiographic image. (a) Raw digital radiographic images exported from Simulix Evolution™ (Nucletron BV, Veenendaal, The Netherlands) console computer. (b) Result of (a) being processed through a "minus logarithm" to compensate for the intensity variation of radiation from the source, to minimize the background noise, and with the gray level inverted. (c) Result of (b) being filtered by a 2-D 10 × 10 Wiener low-pass filter to reduce the constant power additive noise.

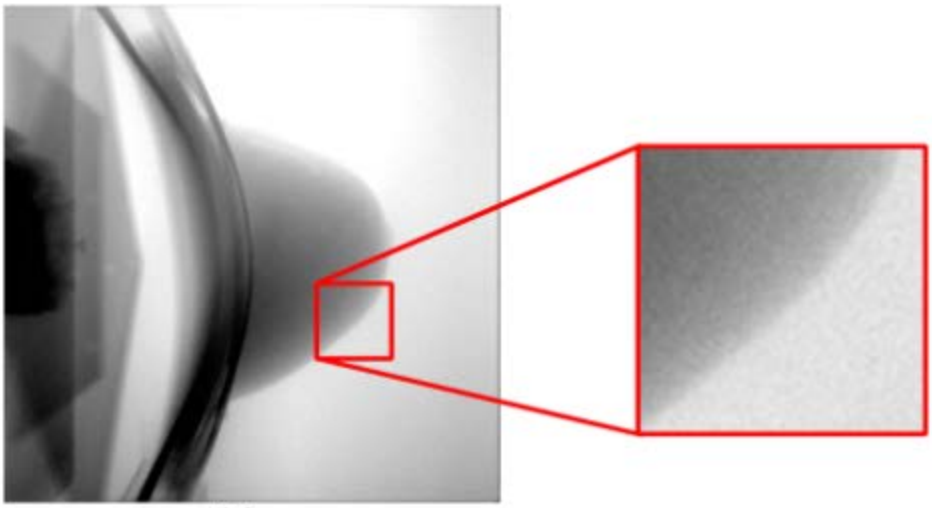

(a)

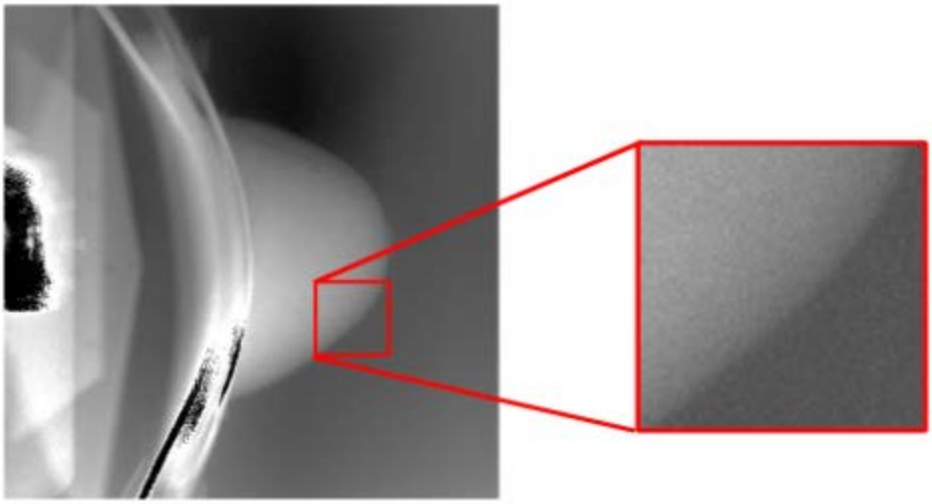

(b)

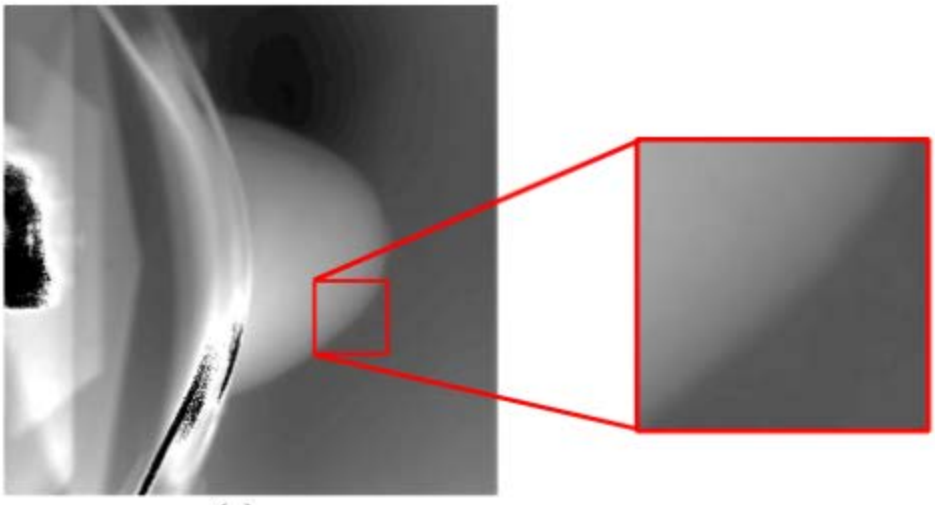

(c)

3.4 Results

From the 121 acquired plane images, we reconstructed a 3-D data set with a size of 549 × 549 × 549 pixels. The data set contains total of 549 coronal images, each image having a dimension of 549 × 549 pixels. Five cystic lesions appeared in 51 images. We also scanned the breast phantom using a conventional CT simulator (SOMATOM Definition AS, Siemens, Germany) as the "ground-truth" reference. The comparison between the reconstructed Ir-192 CBCT and the ground-truth CT are presented in two corresponding CT slices by Figure 3.11.

Figure 3.11a and 3.11c are coronal views of CT slices from the Siemens CT scanner where the cystic lesion is shown in the dark region. The reconstructed Ir-192 CBCT images (Figure 3.11b and 3.11d) corresponding to those two slices presented a very similar result. Compared with the conventional CT, images from the reconstructed Ir-192 CBCT enable us to differentiate the lesions with clarify from normal "breast tissue", as well as the "skin" areas. However, due to the strong scattering effect, CBCT-reconstructed images contained noise signals that induced blurring. The air gaps between the "skin" and "breast tissue" of the phantom is deformable, based on the orientation of the phantom, i.e., the shape of the gaps may vary due to gravity. Therefore, those gaps are not used for comparison between the conventional CT slices and the reconstructed CBCT slices.

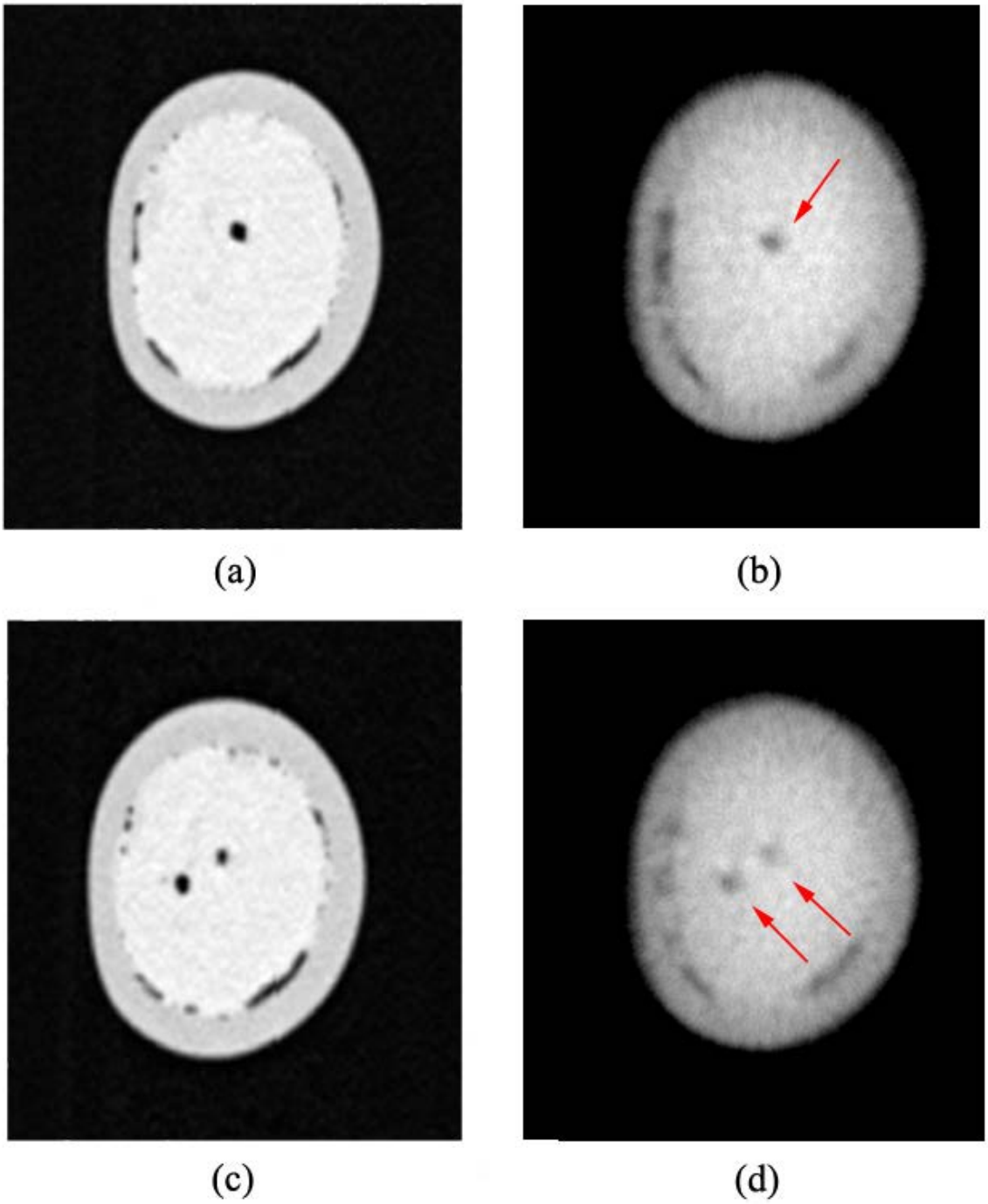

Figure 3.11 Comparison of breast phantom CT images from conventional CT scanner and from Ir-192 CBCT. All images are shown in coronal views. (a) and (c): The CT slices from Siemens CT scanner where the cystic lesions are shown in dark regions. (b) and (d): The corresponding reconstructed Ir-192 CBCT images to (a) and (c). The red arrows indicate the cystic lesions of breast phantom. Compared to the conventional CT, resulting images from the reconstructed Ir-192 CBCT provide sufficient clarity to differentiate the lesion areas, as well as the “skin” and “tissue” areas.

3.5 Discussion

Unlike regular X-ray CT, the quality and quantity of emitted photons are controlled by adjusting the voltage and current of the X-ray tube; the Ir-192 source is a natural radiation. Its activity affects the imaging quality. High activity source emits more photons in a fixed time frame than low activity source, which will produce a more noisy projection because of the increase of Compton scattering. Our source's activity was 7.6307 Ci on the day we collected the projections. An imaging panel with high energy tolerance and wide dynamic range is necessary for data collection, since Ir-192 source has an average energy level of 380 keV, which is much higher than 120 keV from the conventional CT X-ray tube.

Geometry and alignment correction are critical. In this study, we set up the whole system manually (Ir-192 source, rotary stage and detector), so human error is inevitable. We designed a simple alignment correction procedure. In brief, a radio-opaque marker was placed on the rotary stage and two projected images were taken at 0 and 180 degrees respectively (Figure 3.12). By comparing the centers of the marker in two projections, one can easily correct the residual miss-alignment. In Figure 3.12, the cyan lines are the edges of the nail. The red line is the rotation center of the breast phantom, which is the center of the two middle lines in each nail. The pink line marks the image center horizontally. The number of pixels between the red and pink lines is 16 pixels. Therefore, our rotation center was 16 pixels off the image center and we adjusted all projections by 16 pixels.

The geometry setting is crucial for CBCT reconstruction, such as source to object distance (SOD) and object to imager distance (OID). However, photodetectors are usually beneath the imaging panel and are invisible, which prevented us from measuring the true OID. Since we were able to measure the real length of the marker and calculate its projected

length in Figure 3.12, it was not difficult to determine the true OID through triangle proportionality theorem. In this study, for the Simulix Evolution^{TM}, the real photodetectors were 50 mm below the surface of the panel, resulting in the true OID of 265 mm. The metal base holder of the breast phantom generated significant scatter noise to the reconstructed images, especially to the posterior of the breast. Therefore, we displayed coronal views of the breast phantom.

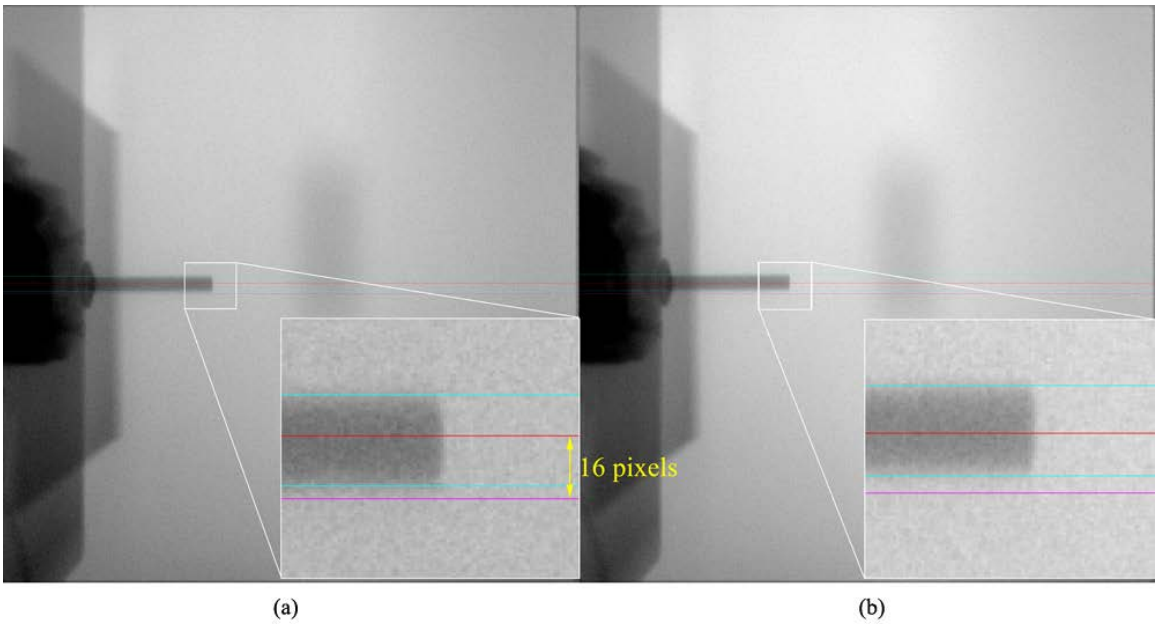

Figure 3.12 Two plane radiographic projections of a marker on the rotary stage for rotation center verification and correction. (a) Projection of rotary stage at 0 degree. (b) Projection of rotary stage at 180 degrees. The cyan lines are the edges of the marker. The red line is the rotation axis of the breast phantom, which is the center of the two middle lines in the marker's projections. The pink line is the image center. The number of pixels between the red and pink lines is 16 pixels.

An integrated image-guiding system will undoubtedly improve the accuracy of HDR brachytherapy delivery. The result of this study suggested that Ir-192 could

potentially be used as an external imaging source, thus making it possible to build a dual-function platform for image-guided target localization and brachytherapy using the same radionuclide source. Such approach could make the application of image-guidance in brachytherapy not only increasingly accessible but also cost-effective.

3.6 Conclusion

A CBCT with HDR radionuclides Ir-192 was successfully obtained in a laboratory setting. In the reconstructed CBCT images, the cystic lesions of breast phantom can be clearly distinguished. Radionuclides such as Ir-192 used in HDR brachytherapy can also be potentially used as external radiation sources for imaging, making a platform of dual-function radiation source for both image-guided localization and brachytherapy delivery feasible.

CHAPTER 4

PRELIMINARY TREATMENT PLANNING

4.1 Background of Treatment Planning System

The purpose of radiation therapy is to deliver adequate radiation dose to the tumor, and minimize the dose to the surrounding and intervening healthy tissues. However, it is difficult to control and tell the dose distribution, since the radiation must penetrate the healthy parts of the body to reach the tumor site. Therefore, a good dosage calculation tool is necessary for radiation treatment planning.

The development of computer hardware and variance reduction techniques for MC methods has significantly reduced the computation time, making MC feasible in clinical TPSs (Han, Mikell, Salehpour, & Mourtada, 2011). Currently, TPSs are the key part of radiation therapy systems. To start a new plan, image datasets from CT, MRI, or other imaging modalities are imported to the system. The tumor site is defined by oncologists, and after that the dosimetrists will use TPS to develop a suitable and complex plan for treatment, which will then be used for the therapy system to deliver radiation (Fornell, 2013). TPS uses radiation transport simulations and optimization to plan the geometric, radiological, and dosimetric aspects of the treatment. By choosing appropriate beam energy and arrangements for external beam radiation therapy, or appropriate catheter positions and source dwell times for brachytherapy, the TPS calculates the expected dose distribution in the patient's tissue. Dose-volume histogram (DVH) is used to evaluate the dose uniformity to the tumor, as well as to avoid the healthy tissues.

In the past two decades, various TPSs for commercial use have been continuously developed. Popularly used TPSs for external beam radiation therapy include, namingly Eclipse™ (Varian Medical Systems, Palo Alto, CA), Monaco® (Elekta, Stockholm, Sweden), Pinnacle® (Philips Medical Systems, Andover, MA.), etc. Other TPSs such as Oncentra Brachy® (Elekta, Stockholm, Sweden) and BrachyVision™ (Varian Medical Systems, Palo Alto, CA) are designed for brachytherapy treatment planning.

4.1.1 Oncentra Brachy®

Oncentra Brachy® comprehensive treatment planning software is a TPS from Elekta, which is designed specifically for brachytherapy planning. It offers a variety of useful tools, such as contouring and reconstruction. It uses Oncentra-ACE algorithm for dose distribution calculation, which is based on collapsed cone superposition (CCS) algorithm (Papagiannis, Pantelis, & Karaiskos, 2014). CCS features a multi-resolution Cartesian calculation grid. The origin is the source dwell position, and the highest resolution is 1 mm in a cube containing the origin. The resolution expands to 2 mm, 5 mm and 10 mm cubes from the origin until it reaches the geometry boundaries, which is defined from patient imaging (Tedgren & Ahnesjö, 2008).

Physicists who make the treatment plan need to choose accuracy levels for dose calculation from two options: standard and accuracy. This system runs relatively slow for dose calculations, especially during the process of dose optimization. Nevertheless, the advantage of the system is that it considers dose to medium in the heterogeneous geometry. Furthermore, it is compatible to all imaging modalities and is not sensitive to CT artifacts in terms of dose calculation (Papagiannis et al., 2014).

4.1.2 BrachyVision™

BrachyVision™ brachytherapy treatment planning system is an integral part of Eclipse™ TPS. The capabilities with Eclipse's contouring, registration, and plan evaluation tools make BrachyVision a powerful TPS. It supports all kinds of brachytherapy, such as HDR, LDR and PDR. The algorithm BrachyVision used is called Acuros™, released by Varian. Acuros is the first commercially available brachytherapy TPS based on grid-based Boltzmann solvers (GBBS) algorithms (Han et al., 2011). GBBS algorithms were introduced in the 1950s and used primarily in various neutral- and charged-particle shielding calculations. Acuros is an algorithm exclusively designed and optimized for brachytherapy from Attila GBBS, which is an alternative version of GBBS developed at Los Alamos National Laboratory (Los Alamos, NM).

Acuros features energy discretization technique for primary photons, and an efficiency gain for the scatter radiation calculation. Triangular-Chebyshev quadrature sets are used for angular discretization and the integration for the generation of the scattering source (Papagiannis et al., 2014). The process of calculation in Acuros is automatic, and the user is required to specify a dose output grid and its resolution. The setting of output grid influences the calculation time, but the resolution setting only affects accuracy.

The dosimetric accuracy and computation speed of Acuros algorithm has been verified by multiple groups, particularly in highly heterogeneous regions (Han et al., 2011; Papagiannis et al., 2014; Zourari et al., 2013; Fogliata et al., 2011; Bush, Gagne, Zavgorodni, Ansbacher, & Beckham, 2011). This algorithm currently is not only used in brachytherapy treatment planning, but also in external beam radiation therapy treatment planning.

4.2 Materials and Methods

Breast CT images were acquired from an 80 year old female with stage III breast cancer. The patient was on the simulator table with a breast board at prone position during the CT simulation. The thickness between each CT slices was 0.5 mm with a resolution of 512 × 512 pixels. The TPS used in this study is Varian Eclipse v13.6 with Acuros v1.6.1.35152. We wanted to create a preliminary four-field conformal plan from four directions.

4.2.1 Contouring

Gross tumor volume (GTV) was defined as gross tumor bed visible in all slices of CT images. The planning target volume (PTV) was based on an automatic 0.5 cm margin expansion to the GTV (Figure 4.1). The following organs at risk (OAR) were generated: left and right lung, normal breast tissue, heart, and skin. The skin is defined as 0.5 cm below the surface (shown in yellow in Figure 4.1).

Since the commercial brachytherapy TPS do not provide the option of a collimator, a virtual structure named "avoidance structure" was created (shown in white in Figure 4.1) on top of the skin with a thickness of 3 cm to serve as a collimator. We assigned a CT value of 3000 Hounsfield Unit (HU) to this structure, which is the maximum HU allowed in Acuros algorithm (Han et al., 2011). The maximum of 3000 HU equals to 3.0 g/cm^3 of mass density. This value is assumed to be the highest density of bone in the images. The assigned CT value overrode any CT values defined in the image in the region of the structure.

4.2.2 Source Locations

For this 3-D conformal plan, the Ir-192 source were planned to irradiate the tumor bed from four fields: superior, inferior, left and right. Unlike the external beam treatment by LINAC for prone position patients where radiation comes from the machine head rotating around the human body, the source in our plan will rotate around the breast during the treatment which is similar to our CBCT imaging model. One HDR applicator was placed at a distance of 5 cm away from the surface of the breast (Figure 4.2). The applicator was aligned horizontally with the center of the tumor bed (Figure 4.2 top left). The total length of the applicator used in this plan was 130 cm. The dwell position was set 1 cm apart. For the radiation from superior field, two dwell positions were set. For the rest of the three fields, three dwell positions each were used. The green dwell positions in Figure 4.2 (bottom left) shows where the Ir-192 source will pause and irradiate.

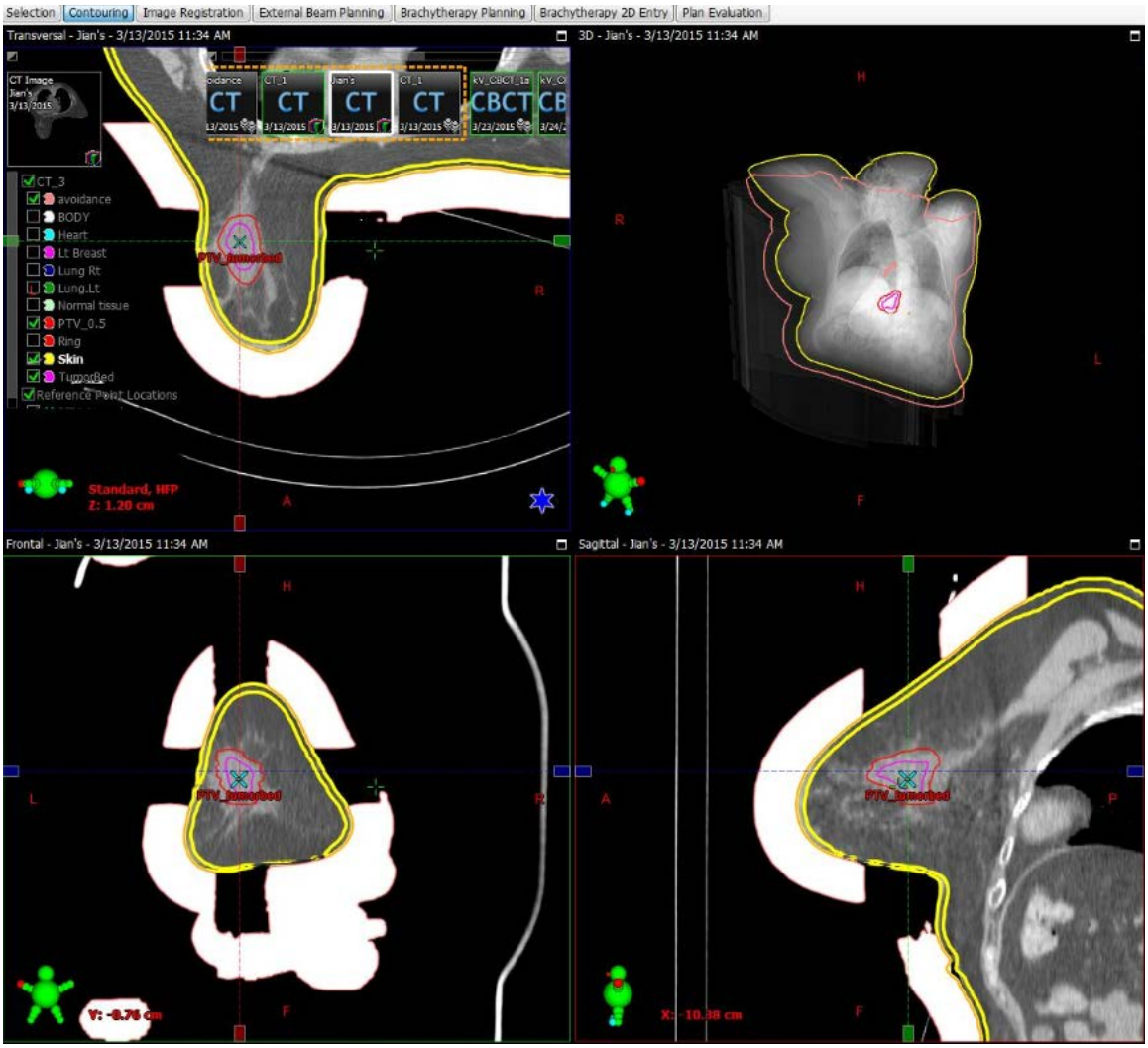

Figure 4.1 Contouring of the treatment plan. GTV was defined as gross tumor bed visible in all slices of CT images. The PTV was based on an automatic 0.5 cm margin around the GTV. A virtual structure named "avoidance structure" was created (shown in white) on top of the skin with a thickness of 3 cm to serve as a collimator. We assigned a CT value of 3000 HU to this structure, which is the maximum HU allowed in Acuros algorithm. Top left: transverse view. Top right: 3-D view. Bottom left: corona view. Bottom right: sagittal view.

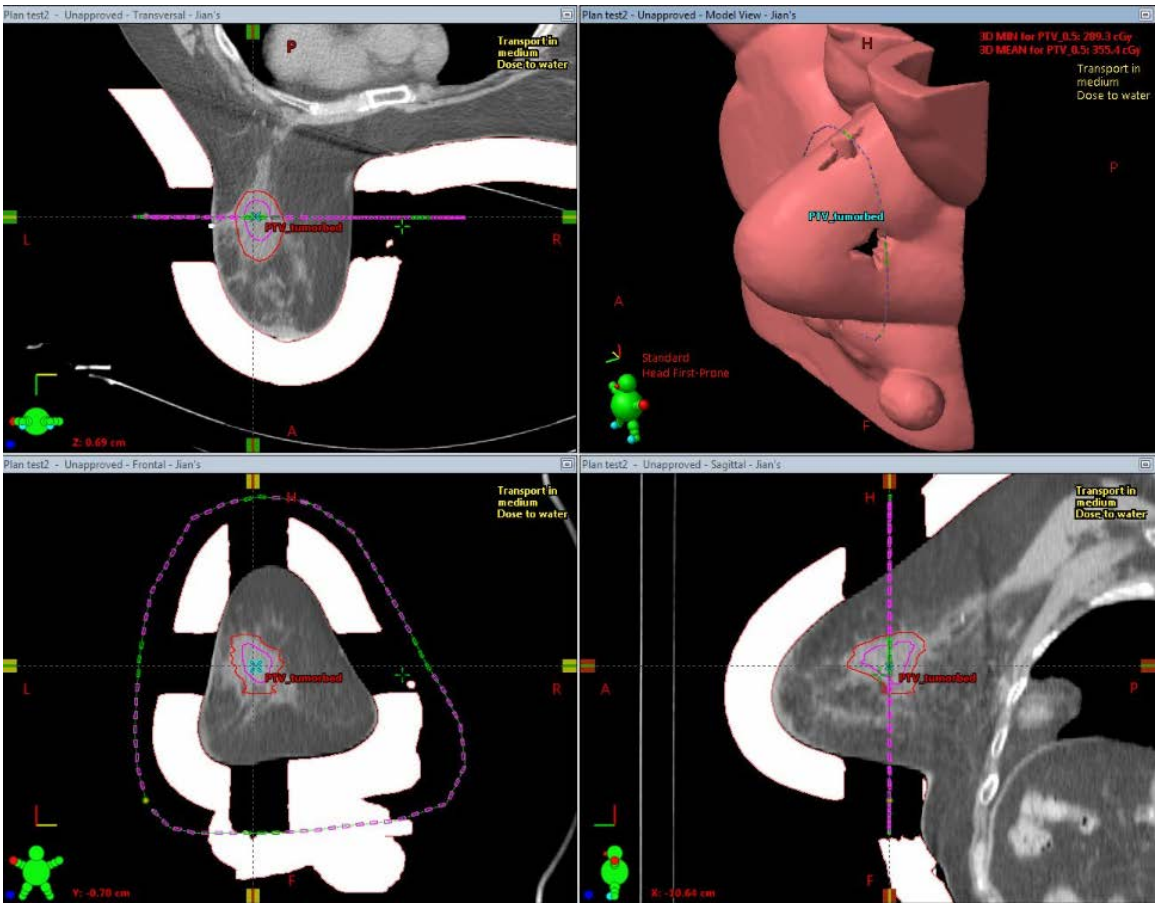

Figure 4.2 Ir-192 source and HDR applicator locations. The applicator was placed at a distance of 5 cm away from the surface of the breast. The applicator was aligned horizontally with the center of the tumor bed. The total length of the applicator used in this plan was 130 cm. The dwell position was set 1 cm apart. For the radiation from superior field, two dwell positions were set. For the rest of the three fields, three dwell positions each were used. The green dwell positions shows where the Ir-192 source will pause and irradiate. Top left: transverse view. Top right: model view. Bottom left: corona view. Bottom right: sagittal view.

We re-contoured the “avoidance structure”, since this structure was used as a collimator to match the shape of the PTV from the beam eye views in four fields. Theoretically, any parts of the patient’s body that is covered by this structure will be minimized from radiation.

4.3 Discussion

Breast cancer patients imaged and treated in prone position is a widely accepted treatment technique. Compared to the normal supine position technique, prone positioning has the major advantage of keeping a similar and reproducible position for CT scanning and treatment (Mahe, Classe, Dravet, Cussac, & Cuilliere, 2002). It can reduce the skin folds of the breast, axilla and neck regions. Furthermore, it significantly decreases dose to the ipsilateral and contralateral lung and improves dose homogeneity regardless of breast size (Griem et al., 2003), which reduces the acute toxicity and late toxicity. Prone position is a more comfortable and relaxing position for patients. In our study, prone position was easier to set up the Ir-192 source to irradiate the breast. Also, this method prevented extra radiation from depositing dose to OARs.

The maximum HU allowed in Eclipse Acuros algorithm is 3000 HU, which equals to 3.0 g/cm^3 of mass density. This is the highest density of bone in the images. We built an "avoidance structure" with assigned 3000 HU materials to serve as a collimator. However, the ideal collimator is made from high-Z materials, such as tungsten. It helps to shape the beam of radiation emerging from the source and can limit the maximum field size of a beam, as well as reduce the dose of OARs.

All modern TPSs are able to calculate the high-resolution dose distribution and DVH, but the conventional brachytherapy TPS has its limitations. The conventional brachytherapy TPS is suitable for cases where source shielding is negligible and high-Z shields or low materials densities are not present (Rivard, Melhus, Granero, Perez-Calatayud, & Ballester, 2009). Also, it assumes that the water is radiologically equivalent to tissue in a certain photon energy range. The conventional TPS fits well for calculation

of dose distributions in unbounded water media. However, in our study, the complex brachytherapy source with a potential high-Z collimator will detract from accurate calculations for clinical brachytherapy dose distributions. Future works include development of advanced brachytherapy dose calculation techniques based on collapsed cone or MC methods, and evaluation of plans with new treatment techniques.

4.4 Conclusion

This preliminary treatment plan provides the initial concept by using Ir-192 as an external source for breast cancer treatment. We propose a 3-D conformal treatment plan with four irradiation fields. The catheter locates outside the patient's breast so that the Ir-192 source can irradiate the tumor bed externally. Future radiation dose evaluation is required. By combining Ir-192's imaging ability which discussed in the previous two chapters, we conclude that it is possible to build an imaging-therapy integrated system by using Ir-192 for breast cancer.

CHAPTER 5

SUMMARY AND FUTURE WORK

Breast cancer is the second most common cancer diagnosed among women in the United States following skin cancer. Approximately one-third of women cancer patients have breast cancer. Following lung cancer, breast cancer is the second highest death rate compared to other types of cancer (DeSantis et al., 2014). Radiation therapy is a common way to treat breast cancer after surgery; it can significantly decrease the breast cancer recurrent rate. For early breast cancer treatment, BCS followed by radiation therapy is preferred over mastectomy (Hamid et al., 2012). Since most of the local recurrences occur near the tumor bed, additional boost radiation to the tumor bed would benefit all patients regardless of their age.

In this dissertation, we developed an imaging/therapy integrated system by using radionuclide Ir-192 for breast cancer. Three major studies have been completed. First of all, we verified the feasibility of using Ir-192 as an external source for breast imaging by MC simulation. Secondly, we built an imaging model in a physical laboratory setting to further prove the imaging ability of Ir-192 source. Thirdly, a preliminary 3-D conformal treatment plan was designed by using a commercial available TPS to evaluate the treatment ability of Ir-192 source.

5.1 Summary

External beam radiation therapy and brachytherapy are the two types of radiation therapy. Imaging is an indispensable part for both methods from simulation to patient positioning. CT and magnetic MRI are commonly used imaging modalities for simulation, and for patient positioning, in addition to US and Mammography as well. In order to increase the treatment accuracy and efficiency, external beam radiation therapy treatment machines usually have on-board imaging system. However, brachytherapy usually requires a separate and independent imaging system to confirm irradiation position for the current treatment procedure. The advantages of brachytherapy include focused and localized irradiation, as well as flexible irradiating capability, but the lack of a coherent imaging system limits its treatment power. High-energy level radionuclides, such as Ir-192, are widely used as brachytherapy treatment sources. Other low-energy level and short half-life radionuclides are usually used as internal emission-based imaging sources for diagnostic nuclear medicine images, such as PET and SPECT. However, Ir-192 has never been used as a transmission-based external imaging source. In this dissertation, we developed an imaging/therapy integrated system by using radionuclide Ir-192 for breast cancer.

In the first study, we used the MC method to simulate breast FBCT and CBCT by using Ir-192 as an external source. The whole breast phantom was built from a real patient's chest CT data. We designed an imaging model and embedded it into the EGSnrc simulation environment. CBCT and FBCT data were obtained through MC simulations. Different image processing techniques were applied to the data. A total of 47 images were reconstructed. Among these images, 16 images have high density areas (lesions). Comparing with the original CT slices, the lesion volume from both FBCT and CBCT data

sets can be identified. CBCT-reconstructed images contain more blurring and noise than FBCT images because of the scattering effects. The result of the MC simulation indicated that Ir-192 radionuclide can be used as a possible external radiation source for breast imaging.

In the second study, we used microSelectron Ir-192 source as the external source and the digital detector of Simulix Evolution simulator as the imaging panel. A breast phantom with cystic lesions was located on a rotary stage in between the source and panel. CBCT projections were obtained at every 3-degree intervals from 0 to 360. Different image processing techniques were applied to the data for CBCT reconstruction. A total of 549 Ir-192 CBCT images were reconstructed. By comparing them with the original CT slices of the breast phantom, the cystic lesions inside can be clearly distinguished. The photon radiation emitted from Ir-192 source has an average energy of 380 keV, higher than that of x-rays used in conventional CT and the more profound Compton scatter will compromise image quality. Furthermore, a mechanic CT simulation test phantom was designed and built from raw materials to mimic first generation CT geometry and data collection. Part of this platform was used in the Ir-192 CBCT real data acquisition. The result of this second study further verified the practicality of using Ir-192 as an external source for breast imaging.

In the third study, a preliminary 3-D conformal treatment plan was designed by using the commercially available TPS Eclipse to evaluate the treatment ability of Ir-192 as an external source. A 340 cGy to the PTV for one fraction was prescribed to a patient who had stage III breast cancer. Acuros algorithm was used for the calculation of dose distribution. The results revealed that 96.5% of tumor bed was covered by 100% of

prescription dose, and 84.6% of PTV was covered by 100% of prescription dose. The maximum dose to the tumor bed and PTV were 326 cGy and 421 cGy, respectively. Total treatment time was 3120 seconds and total air kerma strength was 337.08 Gy/cm^2. This treatment plan verified that Ir-192 as an external radiation source can provide enough dosage to the tumor bed of the breast. It is feasible to use Ir-192 as an external source for breast cancer treatment.

Based on our studies, a new treatment unit which combines imaging and treatment via a single radiation source (Ir-192) could potentially be implemented in the future for IGRT. In this context, an external imaging modality is not needed to guide the brachytherapy treatment, so the dual-function radiation source can simplify the procedure and increase the efficiency. Additionally, it will streamline the device and cut down the cost significantly by not using an additional imaging system.

5.2 Future Work

This dissertation verified the feasibility of a new treatment unit by using Ir-192 as an external source for imaging and treatment. The final goal of this study is to build this new unit and commercialize it. In order to reach this goal, more work need to be done in the future.

For the imaging portion, the patient's dose evaluation for CBCT is required. The dose administered to the patient by the diagnostic CT or LINAC on board kV CBCT is relatively small compared to that of the treatment. Research shows the diagnostic CT has an effective dose range from 10 mSv to 24 mSv (Lee, Haims, Monico, Brink, & Forman,

2004; Groves et al., 2004), and the LINAC on board kV CBCT delivers 1 cGy to 10 cGy to the patient for each scan (Islam et al., 2006; Wen et al., 2007). Ir-192 has an average energy of 380 keV, which is much higher than a regular CT X-ray tube. Therefore, the accumulated total-body dose delivered from this CBCT is considerable. Since extra radiation will increase the risk of secondary cancer occurring, the patient dose evaluation of Ir-192 CBCT is necessary in the future. This evaluation can be separated into two steps. The first step is using MC simulation to calculate the dose, and the second step involves measuring the dose in a real model.

For the treatment portion, a more advanced treatment technique, such as spiral tomotherapy, needs to be evaluated and applied, because the final goal of this study is to develop a treatment unit. Spiral tomotherapy is the delivery of IMRT using rotational delivery of a fan beam, and the couch and gantry are in continuous movement during the treatment (Mackie, 2006). In our designed unit, the Ir-192 source with MLC can move spirally around the patient's breast, instead of moving the couch and gantry in tomotherapy. Patient dose distribution and evaluation are important. Treatment plan that is based on this method has to be examined by using TPS or MC simulation. Furthermore, plan quality assurance (QA) also needs to be validated in the future.

Mechanic design of the system includes source and imaging panel holding, the rotation geometry etc., and integration of the hardware and software are both indispensable for the future development.

REFERENCES

Abo-Madyan, Y., Aziz, M. H., Aly, M. M., Schneider, F., Sperk, E., Clausen, S., ... & Glatting, G. (2014). Second cancer risk after 3D-CRT, IMRT and VMAT for breast cancer. *Radiotherapy and Oncology, 110*(3), 471-476.

AccuBoost. (2016). How does AccuBoost work?. *Advanced Radiation Therapy*. Retrieved from http://www.accuboost.com/how-does-accuboost-work/

Agostinelli, S., Allison, J., Amako, K. A., Apostolakis, J., Araujo, H., Arce, P., ... & Zschiesche, D. (2003). Geant4-a simulation toolkit. *Nuclear Instruments and Methods in Physics Research Section A: Accelerators, Spectrometers, Detectors and Associated Equipment, 506*(3), 250-303.

American Cancer Society. (2015). Breast cancer. *American Cancer Society*. Retrieved from http://www.cancer.org/acs/groups/cid/documents/webcontent/003090-pdf.pdf

Bavley, A. (2012, March 17). New medical device headed to KU could be 'revolutionary' tool for breast cancer. *The Kansas City Star*. Retrieved from http://www.kansascity.com/news/local/article301698/New-medical-device-headed-to-KU-could-be-%E2%80%98revolutionary%E2%80%99-tool-for-breast-cancer.html

Berger, M. J., & Hubbell, J. H. (1987). XCOM: Photon Cross Sections. *Technical Report NBSIR 87-3597*. Gaithersburg, MD: National Bureau of Standard.

Bielajew, A. F., Hirayama, H., Nelson, W. R., & Rogers, D. W. O. (1994) History, overview and recent improvements of EGS4. *Technical Report PIRS-0436*. Ottawa, Canada: National Research Council of Canada.

Bingham, S. A., Luben, R., Welch, A., Wareham, N., Khaw, K. T., & Day, N. (2003). Are imprecise methods obscuring a relation between fat and breast cancer?. *The Lancet, 362*(9379), 212-214.

Boone, J. M., Nelson, T. R., Lindfors, K. K., & Seibert, J. A. (2001). Dedicated breast CT: Radiation dose and image quality evaluation 1. *Radiology, 221*(3), 657-667.

Bush, K., Gagne, I. M., Zavgorodni, S., Ansbacher, W., & Beckham, W. (2011). Dosimetric validation of Acuros® XB with Monte Carlo methods for photon dose calculations. *Medical Physics, 38*(4), 2208-2221.

Chen, Y., Balla, A., Rayford II, C. E., Zhou, W., Fang, J., & Cong, L. (2010). Digital tomosynthesis parallel imaging computational analysis with Shift and Add and Back Projection reconstruction algorithms. *International Journal of Computational Biology and Drug Design, 3*(4), 287-296.

Chen, B., & Ning, R. (2002). Cone-beam volume CT breast imaging: feasibility study. *Medical Physics, 29*(5), 755-770.

Chibani, O., & Li, X. A. (2002). Monte Carlo dose calculations in homogeneous media and at interfaces: a comparison between GEPTS, EGSnrc, MCNP, and measurements. *Medical Physics, 29*(5), 835-847.

Cho, E., Chen, W. Y., Hunter, D. J., Stampfer, M. J., Colditz, G. A., Hankinson, S. E., & Willett, W. C. (2006). Red meat intake and risk of breast cancer among premenopausal women. *Archives of Internal Medicine, 166*(20), 2253-2259.

Cuttino, L. W., Todor, D., & Arthur, D. W. (2005). CT-guided multi-catheter insertion technique for partial breast brachytherapy: reliable target coverage and dose homogeneity. *Brachytherapy, 4*(1), 10-17.

Dahabreh, I. J., Wieland, L. S., Adam, G. P., Halladay, C., Lau, J., & Trikalinos, T. A. (2014). *Core needle and open surgical biopsy for diagnosis of breast lesions: an update to the 2009 report.* Rockville, MD: Agency for Healthcare Research and Quality.

Dahnert, W. (2011). *Radiology Review Manual* (7th ed.). Baltimore, MD: Lippincott Williams & Wilkins.

Daltrey, I. R., & Kissin, M. W. (2000). Randomized clinical trial of the effect of needle gauge and local anaesthetic on the pain of breast fine-needle aspiration cytology. *British Journal of Surgery, 87*(6), 777-779.

Darby, S. C., Ewertz, M., McGale, P., Bennet, A. M., Blom-Goldman, U., Brønnum, D., ... & Jensen, M. B. (2013). Risk of ischemic heart disease in women after radiotherapy for breast cancer. *New England Journal of Medicine, 368*(11), 987-998.

Davis, S. D., Parker, W., & Evans, M. D. (2013). Using mean dose rate to compare relative dosimetric efficiency with respect to source type and source change schedules for HDR brachytherapy†. *Journal of Applied Clinical Medical Physics, 14*(6). doi:10.1120/jacmp.v14i6.4239

Dawson, L. A., & Jaffray, D. A. (2007). Advances in image-guided radiation therapy. *Journal of Clinical Oncology, 25*(8), 938-946.

DeSantis, C., Ma, J., Bryan, L., & Jemal, A. (2014). Breast cancer statistics, 2013. *CA: A Cancer Journal for Clinicians, 64*(1), 52-62.

Ding, G. X., Munro, P., Pawlowski, J., Malcolm, A., & Coffey, C. W. (2010). Reducing radiation exposure to patients from kV-CBCT imaging. *Radiotherapy and Oncology, 97*(3), 585-592.

Faddegon, B. A., Kawrakow, I., Kubyshin, Y., Perl, J., Sempau, J., & Urban, L. (2009). The accuracy of EGSnrc, Geant4 and PENELOPE Monte Carlo systems for the simulation of electron scatter in external beam radiotherapy. *Physics in Medicine and Biology, 54*(20), 6151-6163.

Fang, J., Lupp, M., & Zhao, W. (2014, October). *Design and development of a Laser-CT: a medical imaging training system.* Poster presented at the annual meeting of the Biomedical Engineering Society, San Antonio, TX.

Fang, J., Wu, X., Yang, Y., & Zhao, W. (2015, October-November). *An external radionuclide (^{192}Ir) Monte Carlo CBCT simulation for breast imaging.* Poster presented at the medical imaging conference of the Institute of Electrical and Electronics Engineers, San Diego, CA.

Fang, J., Wu, X., Yang, Y., & Zhao, W. (2016). A new imaging/therapy platform by using external radionuclide (^{192}Ir), Part 1: Monte Carlo FBCT and CBCT simulation for breast imaging. *Journal of Radiation Oncology,* 1-7. doi: 10.1007/s13566-016-0252-9

Feldkamp, L. A., Davis, L. C., & Kress, J. W. (1984). Practical cone-beam algorithm. *Journal of the Optical Society of America A, 1*(6), 612-619.

Fogliata, A., Nicolini, G., Clivio, A., Vanetti, E., Mancosu, P., & Cozzi, L. (2011). Dosimetric validation of the Acuros XB Advanced Dose Calculation algorithm: fundamental characterization in water. *Physics in Medicine and Biology, 56*(6), 1879-1904.

Fornell, D. (2013, July 8). An introduction to current radiation therapy treatment planning systems. *Imaging Technology News*. Retrieved from http://www.itnonline.com/article/introduction-current-radiation-therapy-treatment-planning-systems

Goetsch, S. J., Attix, F. H., Pearson, D. W., & Thomadsen, B. R. (1991). Calibration of ^{192}Ir high-dose-rate afterloading systems. *Medical Physics, 18*(3), 462-467.

Griem, K. L., Fetherston, P., Kuznetsova, M., Foster, G. S., Shott, S., & Chu, J. (2003). Three-dimensional photon dosimetry: a comparison of treatment of the intact breast in the supine and prone position. *International Journal of Radiation Oncology • Biology • Physics, 57*(3), 891-899.

Groves, A. M., Owen, K. E., Courtney, H. M., Yates, S. J., Goldstone, K. E., Blake, G. M., & Dixon, A. K. (2004). 16-detector multislice CT: dosimetry estimation by TLD measurement compared with Monte Carlo simulation. *The British Journal of Radiology, 77*(920), 662-665.

Grupen, C., & Buvat, I. (Eds.). (2012). *Handbook of Particle Detection and Imaging*. Berlin, Germany: Springer.

Guinot, J. L., Baixauli-Perez, C., Soler, P., Tortajada, M. I., Moreno, A., Santos, M. A., ... & Arribas, L. (2015). High-dose-rate brachytherapy boost effect on local tumor control in young women with breast cancer. *International Journal of Radiation Oncology • Biology • Physics, 91*(1), 165-171.

Hall, E. J., & Wuu, C. S. (2003). Radiation-induced second cancers: the impact of 3D-CRT and IMRT. *International Journal of Radiation Oncology • Biology • Physics, 56*(1), 83-88.

Hamid, S., Rocchio, K., Arthur, D., Vera, R., Sha, S., Jolly, M., ... & Prestidge, B. (2012). A multi-institutional study of feasibility, implementation, and early clinical results with noninvasive breast brachytherapy for tumor bed boost. *International Journal of Radiation Oncology • Biology • Physics, 83*(5), 1374-1380.

Han, T., Mikell, J. K., Salehpour, M., & Mourtada, F. (2011). Dosimetric comparison of Acuros XB deterministic radiation transport method with Monte Carlo and model-based convolution methods in heterogeneous media. *Medical Physics, 38*(5), 2651-2664.

Hartmann, L. C., & Loprinzi, C. L. (Eds.). (2012). *The Mayo Clinic Breast Cancer Book*. Intercourse, PA: Good Books

Hepel, J. T., Leonard, K. L., Hiatt, J. R., DiPetrillo, T. A., & Wazer, D. E. (2014). Factors influencing eligibility for breast boost using noninvasive image-guided breast brachytherapy. *Brachytherapy, 13*(6), 579-583.

Ho, A. Y., Burri, R. J., Cesaretti, J. A., Stone, N. N., & Stock, R. G. (2009). Radiation dose predicts for biochemical control in intermediate-risk prostate cancer patients treated with low-dose-rate brachytherapy. *International Journal of Radiation Oncology • Biology • Physics*, 75(1), 16-22.

Hsieh, J. (2003). Computed Tomography: Principles, Design, Artifacts, and Recent Advances. Bellingham, WA: SPIE Press.

Hubbard, R. A., Kerlikowske, K., Flowers, C. I., Yankaskas, B. C., Zhu, W., & Miglioretti, D. L. (2011). Cumulative probability of false-positive recall or biopsy recommendation after 10 years of screening mammography: a cohort study. *Annals of Internal Medicine, 155*(8), 481-492.

Hubbell, J. H. (1999). Review of photon interaction cross section data in the medical and biological context. *Physics in Medicine and Biology, 44*(1), R1-R22.

Huda, W., & Slone, R. M. (2003). *Review of Radiologic Physics* (2nd ed.). Philadelphia, PA: Lippincott Williams & Wilkins.

Hulka, B. S., & Moorman, P. G. (2001). Breast cancer: hormones and other risk factors. *Maturitas, 38*(1), 103-113.

Huppert, N., Jozsef, G., DeWyngaert, K., & Formenti, S. C. (2011). The role of a prone setup in breast radiation therapy. *Frontiers in Oncology, 1*, 31.

Huq, M. S., Das, I. J., Steinberg, T., & Galvin, J. M. (2002). A dosimetric comparison of various multileaf collimators. *Physics in Medicine and Biology, 47*(12), N159-N170.

Iftimia, I., Talmadge, M., Ladd, R., & Halvorsen, P. (2015). Commissioning and quality assurance for the treatment delivery components of the AccuBoost system. *Journal of Applied Clinical Medical Physics, 16*(2), 129-143.

Islam, M. K., Purdie, T. G., Norrlinger, B. D., Alasti, H., Moseley, D. J., Sharpe, M. B., ... & Jaffray, D. A. (2006). Patient dose from kilovoltage cone beam computed tomography imaging in radiation therapy. *Medical Physics, 33*(6), 1573-1582.

Kawrakow, I. (2000). Accurate condensed history Monte Carlo simulation of electron transport. I. EGSnrc, the new EGS4 version. *Medical Physics, 27*(3), 485-498.

Kawrakow, I. (2002). On the de-noising of Monte Carlo calculated dose distributions. *Physics in Medicine and Biology, 47*(17), 3087-3103.

Kawrakow, I., Mainegra-Hing, E., Rogers, D. W. O., Tessier, F., & Walter, B. R. B. (2011). The EGSnrc code system. *NRC Report PIRS-701(6th printing)*. Ottawa, Canada: National Research Council of Canada.

Kawrakow, I., Mainegra-Hing, E., Tessier, F., & Walters, B. R. B. (2009). The EGSnrc C++ class library. *NRC Report PIRS-898 (rev A).* Ottawa, Canada: National Research Council of Canada.

Kelley, J. R., Cuttino, L. W., Vicini, F. A., & Arthur, D. W. (2007) Breast Brachytherapy. In P. M. Devlin (Ed.) *Brachytherapy: Applications and Techniques* (pp. 115-136). Philadelphia, PA: Lippincott Williams & Wilkins.

Kim, Y., & Trombetta, M. G. (2014). Dosimetric evaluation of multilumen intracavitary balloon applicator rotation in high-dose-rate brachytherapy for breast cancer. *Journal of Applied Clinical Medical Physics, 15*(1), 76-89.

Kolb, T. M., Lichy, J., & Newhouse, J. H. (2002). Comparison of the performance of screening mammography, physical examination, and breast us and evaluation of factors that influence them: An analysis of 27,825 patient evaluations 1. *Radiology, 225*(1), 165-175.

Kroese, D. P., Brereton, T., Taimre, T., & Botev, Z. I. (2014). Why the Monte Carlo method is so important today. *Wiley Interdisciplinary Reviews: Computational Statistics, 6*(6), 386-392.

Kuhl, C. K., Schrading, S., Leutner, C. C., Morakkabati-Spitz, N., Wardelmann, E., Fimmers, R., ... & Schild, H. H. (2005). Mammography, breast ultrasound, and magnetic resonance imaging for surveillance of women at high familial risk for breast cancer. *Journal of Clinical Oncology, 23*(33), 8469-8476.

Lawrence, T. S., Ten Haken, R. K., & Giaccia, A. (2008) Principles of radiation oncology. In V. T. DeVita Jr., T. S. Lawrence, & S. A. Rosenberg (Eds.) *Cancer: Principles and Practice of Oncology* (8th ed., pp. 307-336). Philadelphia, PA: Lippincott Williams & Wilkins.

Lee, C. H., Dershaw, D. D., Kopans, D., Evans, P., Monsees, B., Monticciolo, D., ... & Burhenne, L. W. (2010). Breast cancer screening with imaging: recommendations from the Society of Breast Imaging and the ACR on the use of mammography, breast MRI, breast ultrasound, and other technologies for the detection of clinically occult breast cancer. *Journal of the American College of Radiology, 7*(1), 18-27.

Lee, C. I., Haims, A. H., Monico, E. P., Brink, J. A., & Forman, H. P. (2004). Diagnostic CT scans: assessment of patient, physician, and radiologist awareness of radiation dose and possible risks. *Radiology, 231*(2), 393-398.

Lee, S. W., Lee, C. L., Cho, H. M., Park, H. S., Kim, D. H., Choi, Y. N., & Kim, H. J. (2011). Effects of reconstruction parameters on image noise and spatial resolution in cone-beam computed tomography. *Journal of the Korean Physical Society, 59*(4), 2825-2832.

Lee, C., & Lowe, G. (2011) Isotopes and delivery systems for brachytherapy. In P. J. Hoskin, & C. Coyle (Eds.) *Radiotherapy in Practice - Brachytherapy* (2nd ed., pp. 5-24). New York, NY: Oxford University Press.

Lim, J. S. (1990). *Two-dimensional Signal and Image Processing*. Englewood Cliffs, NJ: Prentice Hall.

Lim, Y. Y., & Maxwell, A. J. (2015). Digital breast tomosynthesis. In P. Hogg, J. Kelly, & C. Mercer (Eds.) *Digital Mammography: A Holistic Approach* (pp. 241-246). Switzerland: Springer International Publishing.

Lindfors, K. K., Boone, J. M., Nelson, T. R., Yang, K., Kwan, A. L., & Miller, D. F. (2008). Dedicated breast CT: Initial clinical experience 1. *Radiology, 246*(3), 725-733.

Lux, I., & Koblinger, L. (1991). *Monte Carlo Particle Transport Methods: Neutron and Photon Calculations*. Boca Raton, FL: CRC Press.

Mackie, T. R. (2006). History of tomotherapy. *Physics in Medicine and Biology, 51*(13), R427-R453.

Mahe, M. A., Classe, J. M., Dravet, F., Cussac, A., & Cuilliere, J. C. (2002). Preliminary results for prone-position breast irradiation. *International Journal of Radiation Oncology • Biology • Physics, 52*(1), 156-160.

Mainegra-Hing, E., & Kawrakow, I. (2008). Fast Monte Carlo calculation of scatter corrections for CBCT images. *Journal of Physics: Conference Series, 102*(1), 012017.

Mainegra-Hing, E., & Kawrakow, I. (2010). Variance reduction techniques for fast Monte Carlo CBCT scatter correction calculations. *Physics in Medicine and Biology, 55*(16), 4495-4507.

Marcu, L., Bezak, E., & Allen, B. (2012). *Biomedical Physics in Radiotherapy for Cancer*. Collingwood, Australia: CSIRO Publishing.

Mauri, D., Pavlidis, N., & Ioannidis, J. P. (2005). Neoadjuvant versus adjuvant systemic treatment in breast cancer: a meta-analysis. *Journal of the National Cancer Institute, 97*(3), 188-194.

McGuire, K. P., Santillan, A. A., Kaur, P., Meade, T., Parbhoo, J., Mathias, M., ... & Cox, C. E. (2009). Are mastectomies on the rise? A 13-year trend analysis of the selection of mastectomy versus breast conservation therapy in 5865 patients. *Annals of Surgical Oncology, 16*(10), 2682-2690.

McPherson, K., Steel, C. M., & Dixon, J. M. (2000). Breast cancer-epidemiology, risk factors, and genetics. *BMJ: British Medical Journal, 321*(7261), 624–628.

McRobbie, D. W., Moore, E. A., Graves, M. J., & Prince, M. R. (2007). *MRI from Picture to Proton* (2nd ed.). Cambridge, UK: Cambridge University Press.

Metcalfe, P., Kron, T., & Hoban, P. (2007). *The Physics of Radiotherapy X-rays and Electrons.* Madison, WI: Medical Physics Publishing.

Miki, Y., Swensen, J., Shattuck-Eidens, D., Futreal, P. A., Harshman, K., Tavtigian, S., … & Skolnick, M. H. (1994). A strong candidate for the breast and ovarian cancer susceptibility gene BRCA1. *Science, 266*(5182), 66-71.

Miller, R., & Thomadsen, B. (2009). *Brachytherapy physics: everything you need to know and controversial issues* [PowerPoint slides]. Retrieved from http://www.aapm.org/meetings/amos2/pdf/42-11873-3201-79.pdf

Mutaf, Y. D., Zhang, J., Yu, C. X., Yi, B. Y., Prado, K., D'Souza, W. D., ... & Feigenberg, S. J. (2013). Dosimetric and geometric evaluation of a novel stereotactic radiotherapy device for breast cancer: The GammaPod™. *Medical Physics, 40*(4), 041722.

Nag, S., Cano, E. R., Demanes, D. J., Puthawala, A. A., & Vikram, B. (2001). The American Brachytherapy Society recommendations for high-dose-rate brachytherapy for head-and-neck carcinoma. *International Journal of Radiation Oncology • Biology • Physics, 50*(5), 1190-1198.

Nag, S., Chao, C., Erickson, B., Fowler, J., Gupta, N., Martinez, A., & Thomadsen, B. (2002). The American Brachytherapy Society recommendations for low-dose-rate brachytherapy for carcinoma of the cervix. *International Journal of Radiation Oncology • Biology • Physics, 52*(1), 33-48.

Nag, S., Erickson, B., Parikh, S., Gupta, N., Varia, M., & Glasgow, G. (2000a). The American Brachytherapy Society recommendations for high-dose-rate brachytherapy for carcinoma of the endometrium. *International Journal of Radiation Oncology • Biology • Physics, 48*(3), 779-790.

Nag, S., Erickson, B., Thomadsen, B., Orton, C., Demanes, J. D., & Petereit, D. (2000b). The American Brachytherapy Society recommendations for high-dose-rate brachytherapy for carcinoma of the cervix. *International Journal of Radiation Oncology • Biology • Physics, 48*(1), 201-211.

Nag, S., Shasha, D., Janjan, N., Petersen, I., & Zaider, M. (2001). The American Brachytherapy Society recommendations for brachytherapy of soft tissue sarcomas. *International Journal of Radiation Oncology • Biology • Physics, 49*(4), 1033-1043.

Nath, M. E., Robinson, T. M., Tobon, H., Chough, D. M., & Sumkin, J. H. (1995). Automated large-core needle biopsy of surgically removed breast lesions: comparison of samples obtained with 14-, 16-, and 18-gauge needles. *Radiology, 197*(3), 739-742.

National Cancer Institute. (2014). A snapshot of breast cancer. *National Cancer Institute*. Retrieved from http://www.cancer.gov/research/progress/snapshots/breast

Ödén, J., Toma-Dasu, I., Cedric, X. Y., Feigenberg, S. J., Regine, W. F., & Mutaf, Y. D. (2013). Dosimetric comparison between intra-cavitary breast brachytherapy techniques for accelerated partial breast irradiation and a novel stereotactic radiotherapy device for breast cancer: GammaPod™. *Physics in Medicine and Biology*, 58(13), 4409-4421.

Oeffinger, K. C., Fontham, E. T., Etzioni, R., Herzig, A., Michaelson, J. S., Shih, Y. C. T., ... & Wender, R. (2015). Breast cancer screening for women at average risk: 2015 guideline update from the American Cancer Society. *The Journal of American Medical Association, 314*(15), 1599-1614.

Olivotto, I. A., Whelan, T. J., Parpia, S., Kim, D. H., Berrang, T., Truong, P. T., ... & Germain, I. (2013). Interim cosmetic and toxicity results from RAPID: a randomized trial of accelerated partial breast irradiation using three-dimensional conformal external beam radiation therapy. *Journal of Clinical Oncology, 31*(32), 4038-4045.

Otto, K. (2008). Volumetric modulated arc therapy: IMRT in a single gantry arc. *Medical Physics, 35*(1), 310-317.

Pagni, P., Spunticchia, F., Barberi, S., Caprio, G., & Paglicci, C. (2014). Use of core needle biopsy rather than fine-needle aspiration cytology in the diagnostic approach of breast cancer. *Case Reports in Oncology, 7*(2), 452–458.

Papagiannis, P., Pantelis, E., & Karaiskos, P. (2014). Current state of the art brachytherapy treatment planning dosimetry algorithms. *The British Journal of Radiology, 87*(1041), 20140163.

Pasler, M., Georg, D., Bartelt, S., & Lutterbach, J. (2013). Node-positive left-sided breast cancer: does VMAT improve treatment plan quality with respect to IMRT?. *Strahlentherapie und Onkologie, 189*(5), 380-386.

Pegram, M. D., Pietras, R., Bajamonde, A., Klein, P., & Fyfe, G. (2005). Targeted therapy: wave of the future. *Journal of Clinical Oncology, 23*(8), 1776-1781.

Pérez-Calatayud, J., Ballester, F., Das, R. K., DeWerd, L. A., Ibbott, G. S., Meigooni, A. S., ... & Williamson, J. F. (2012). Dose calculation for photon-emitting brachytherapy sources with average energy higher than 50 keV: Report of the AAPM and ESTRO. *Medical Physics, 39*(5), 2904-2929.

Pérez-Calatayud, J., Granero, D., Ballester, F., Puchades, V., Casal, E., Soriano, A., & Crispín, V. (2005). A dosimetric study of Leipzig applicators. *International Journal of Radiation Oncology • Biology • Physics, 62*(2), 579-584.

Pierce, J. P., Natarajan, L., Caan, B. J., Parker, B. A., Greenberg, E. R., Flatt, S. W., ... & Stefanick, M. L. (2007). Influence of a diet very high in vegetables, fruit, and fiber and low in fat on prognosis following treatment for breast cancer: the Women's Healthy Eating and Living (WHEL) randomized trial. *The Journal of American Medical Association, 298*(3), 289-298.

Popescu, C. C., Olivotto, I. A., Beckham, W. A., Ansbacher, W., Zavgorodni, S., Shaffer, R., ... & Otto, K. (2010). Volumetric modulated arc therapy improves dosimetry and reduces treatment time compared to conventional intensity-modulated radiotherapy for locoregional radiotherapy of left-sided breast cancer and internal mammary nodes. *International Journal of Radiation Oncology • Biology • Physics, 76*(1), 287-295.

Pouliot, J., Bani-Hashemi, A., Chen, J., Svatos, M., Ghelmansarai, F., Mitschke, M., ... & Roach, M. (2005). Low-dose megavoltage cone-beam CT for radiation therapy. *International Journal of Radiation Oncology • Biology • Physics, 61*(2), 552-560.

Preibsch, H., Baur, A., Wietek, B. M., Krämer, B., Staebler, A., Claussen, C. D., & Siegmann-Luz, K. C. (2015). Vacuum-assisted breast biopsy with 7-gauge, 8-gauge, 9-gauge, 10-gauge, and 11-gauge needles: how many specimens are necessary?. *Acta Radiologica, 56*(9), 1078-1084.

Prionas, N. D., Lindfors, K. K., Ray, S., Huang, S. Y., Beckett, L. A., Monsky, W. L., & Boone, J. M. (2010). Contrast-enhanced dedicated breast CT: initial clinical experience 1. *Radiology, 256*(3), 714-723.

Rao, M., Yang, W., Chen, F., Sheng, K., Ye, J., Mehta, V., ... & Cao, D. (2010). Comparison of Elekta VMAT with helical tomotherapy and fixed field IMRT: plan quality, delivery efficiency and accuracy. *Medical Physics, 37*(3), 1350-1359.

Rasmussen, B. E., Davis, S. D., Schmidt, C. R., Micka, J. A., & DeWerd, L. A. (2011). Comparison of air-kerma strength determinations for HDR ^{192}Ir sources. *Medical Physics, 38*(12), 6721-6729.

Reitsamer, R., Sedlmayer, F., Kopp, M., Kametriser, G., Menzel, C., Glueck, S., ... & Peintinger, F. (2008). Concepts and techniques of intraoperative radiotherapy (IORT) for breast cancer. *Breast Cancer, 15*(1), 40-46.

Reniers, B., & Verhaegen, F. (2011). Technical Note: Cone beam CT imaging for 3-D image guided brachytherapy for gynecological HDR brachytherapy. *Medical Physics, 38*(5), 2762-2767.

Richards, G. M., Berson, A. M., Rescigno, J., Sanghavi, S., Siegel, B., Axelrod, D., ... & Mills, C. (2004). Acute toxicity of high-dose-rate intracavitary brachytherapy with the MammoSite applicator in patients with early-stage breast cancer. *Annals of Surgical Oncology, 11*(8), 739-746.

Richardson, J. T. (2010). *Early breast cancer: the role of radiation therapy* [PowerPoint slides]. Retrieved from http://www.slideshare.net/MercyHealthSystem/breast-cancer-webinar

Rivard, M. J., Melhus, C. S., Granero, D., Perez-Calatayud, J., & Ballester, F. (2009). An approach to using conventional brachytherapy software for clinical treatment planning of complex, Monte Carlo-based brachytherapy dose distributions. *Medical Physics, 36*(6), 1968-1975.

Rivard, M. J., Melhus, C. S., Wazer, D. E., & Bricault Jr, R. J. (2009). Dosimetric characterization of round HDR I192r AccuBoost applicators for breast brachytherapy. *Medical Physics, 36*(11), 5027-5032.

Rogers, D. W. O. (2006). Fifty years of Monte Carlo simulations for medical physics. *Physics in Medicine and Biology, 51*(13), R287-R301.

Salvat, F., Fernández-Varea, J. M., & Sempau, J. (2008). PENELOPE-2008: A code system for Monte Carlo simulation of electron and photon transport. *NEA Workshop Proceedings No.6416*. Barcelona, Spain: Nuclear Energy Agency, Organisation for Economic Co-Operation and Development.

Saw, C. B., Loper, A., Komanduri, K., Combine, T., Huq, S., & Scicutella, C. (2005). Determination of CT-to-density conversion relationship for image-based treatment planning systems. *Medical Dosimetry, 30*(3), 145-148.

Scanderbeg, D. J., Yashar, C., White, G., Rice, R., & Pawlicki, T. (2010). Evaluation of three APBI techniques under NSABP B-39 guidelines. *Journal of Applied Clinical Medical Physics, 11*(1), 274-280.

Shin, M. H., Holmes, M. D., Hankinson, S. E., Wu, K., Colditz, G. A., & Willett, W. C. (2002). Intake of dairy products, calcium, and vitamin D and risk of breast cancer. *Journal of the National Cancer Institute, 94*(17), 1301-1310.

Singletary, K. W., & Gapstur, S. M. (2001). Alcohol and breast cancer: review of epidemiologic and experimental evidence and potential mechanisms. *The Journal of American Medical Association, 286*(17), 2143-2151.

Sinha, A., Singh, N., Gurjar, O. P., & Bagdare, P. (2015). Acceptance testing and quality assurance of Simulix Evolution radiotherapy simulator. *Radiation Protection and Environment, 38*(3), 102-108.

Sioshansi, S., Hiatt, J. R., Rivard, M. J., Hepel, J. T., Cardarelli, G. A., O'Leary, S., & Wazer, D. E. (2008). Three-dimensional dose modeling of the AccuBoost mammography-based image guided non-invasive breast brachytherapy system for partial breast irradiation. *International Journal of Radiation Oncology • Biology • Physics, 72*(1), S516-S517.

Skowronek, J., Wawrzyniak-Hojczyk, M., & Ambrochowicz, K. (2012). Brachytherapy in accelerated partial breast irradiation (APBI)-review of treatment methods. *Journal of Contemporary Brachytherapy, 4*(3), 152-164.

Sledge, G. W. (2005). What is targeted therapy?. *Journal of Clinical Oncology, 23*(8), 1614-1615.

Tedgren, Å. C., & Ahnesjö, A. (2008). Optimization of the computational efficiency of a 3-D, collapsed cone dose calculation algorithm for brachytherapy. *Medical Physics, 35*(4), 1611-1618.

Tello, V. M. (2015). *Medical linear accelerators and how they work* [PowerPoint slides]. Retrieved from http://hpschapters.org/florida/13PPT.pdf

Thing, R. S., & Mainegra-Hing, E. (2014). Optimizing cone beam CT scatter estimation in egs_cbct for a clinical and virtual chest phantom. *Medical Physics, 41*(7), 071902.

Tornai, M. P., Bowsher, J. E., Jaszczak, R. J., Pieper, B. C., Greer, K. L., Hardenbergh, P. H., & Coleman, R. E. (2003). Mammotomography with pinhole incomplete circular orbit SPECT. *Journal of Nuclear Medicine, 44*(4), 583-593.

Vicini, F. A., & Arthur, D. W. (2005). Breast brachytherapy: North American experience. *Seminars in Radiation Oncology, 15*(2), 108-115.

Wang, R., & Li, X. A. (2001). Monte Carlo dose calculations of beta-emitting sources for intravascular brachytherapy: A comparison between EGS4, EGSnrc, and MCNP. *Medical Physics, 28*(2), 134-141.

Wen, N., Guan, H., Hammoud, R., Pradhan, D., Nurushev, T., Li, S., & Movsas, B. (2007). Dose delivered from Varian's CBCT to patients receiving IMRT for prostate cancer. *Physics in Medicine and Biology, 52*(8), 2267-2276.

Willems, S. M., Van Deurzen, C. H. M., & Van Diest, P. J. (2012). Diagnosis of breast lesions: fine-needle aspiration cytology or core needle biopsy? A review. *Journal of Clinical Pathology, 65*(4), 287-292.

Woody, N. M., & Videtic, G. M. M. (2014). Tools for simulation and treatment. In G. M. M. Videtic, N. M. Woody, & A. D. Vassil (Eds.) *Handbook of Treatment Planning in Radiation Oncology* (2nd ed., 17-26). New York, NY: Demos Medical Publishing.

Wooster, R., Neuhausen, S. L., Mangion, J., Quirk, Y., Ford, D., Collins, N., ... & Stratton, M. R. (1994). Localization of a breast cancer susceptibility gene, BRCA2, to chromosome 13q12-13. *Science, 265*(5181), 2088-2090.

X-5 Monte Carlo Team. (2008). MCNP - A General Monte Carlo N-Particle Transport Code, Version 5. Volume I: Overview and Theory. *Los Alamos National Laboratory*. Retrieved from https://laws.lanl.gov/vhosts/mcnp.lanl.gov/pdf_files/la-ur-03-1987.pdf

Xing, L., Thorndyke, B., Schreibmann, E., Yang, Y., Li, T. F., Kim, G. Y., ... & Koong, A. (2006). Overview of image-guided radiation therapy. *Medical Dosimetry, 31*(2), 91-112.

Yamada, Y., Rogers, L., Demanes, D. J., Morton, G., Prestidge, B. R., Pouliot, J., ... & Hsu, I. C. (2012). American Brachytherapy Society consensus guidelines for high-dose-rate prostate brachytherapy. *Brachytherapy, 11*(1), 20-32.

Yashar, C. M., Blair, S., Wallace, A., & Scanderbeg, D. (2009). Initial clinical experience with the Strut-Adjusted Volume Implant brachytherapy applicator for accelerated partial breast irradiation. *Brachytherapy, 8*(4), 367-372.

Yoshimura, R. I., Shibuya, H., Miura, M., Watanabe, H., Ayukawa, F., Hayashi, K., & Toda, K. (2009). Quality of life of oral cancer patients after low-dose-rate interstitial brachytherapy. *International Journal of Radiation Oncology • Biology • Physics, 73*(3), 772-778.

Yu, C. X. (1995). Intensity-modulated arc therapy with dynamic multileaf collimation: an alternative to tomotherapy. *Physics in Medicine and Biology, 40*(9), 1435-1449.

Yu, C. X., Shao, X., Zhang, J., Regine, W., Zheng, M., Ying, S. Y., ... & Duan, Z. (2013). GammaPod—A new device dedicated for stereotactic radiotherapy of breast cancer. *Medical Physics, 40*(5), 051703.

Yu, Y. H., Wei, W., & Liu, J. L. (2012). Diagnostic value of fine-needle aspiration biopsy for breast mass: a systematic review and meta-analysis. *BMC cancer, 12*(1), 41.

Yue, N. J., Chen, T., & Zou, W. (2014). Radiation oncology and medical devices (Part 2). *China Medical Devices, 29*(2), 1-10.

Zannis, V. J., Walker, L. C., Barclay-White, B., & Quiet, C. A. (2003). Postoperative ultrasound-guided percutaneous placement of a new breast brachytherapy balloon catheter. *The American Journal of Surgery, 186*(4), 383-385.

Zourari, K., Pantelis, E., Moutsatsos, A., Sakelliou, L., Georgiou, E., Karaiskos, P., & Papagiannis, P. (2013). Dosimetric accuracy of a deterministic radiation transport based 192Ir brachytherapy treatment planning system. Part III. Comparison to Monte Carlo simulation in voxelized anatomical computational models. *Medical Physics, 40*(1), 011712.